1-1-2008

Design of a prototype bioresorbable tibial implant in a sheep model

Adrian Dudi Janura
Ryerson University

DESIGN OF A PROTOTYPE BIORESORBABLE TIBIAL IMPLANT IN A SHEEP MODEL

By

Ardian Dudi Janura
B.Eng. (Aerospace Engineering),
Ryerson University (Toronto, Canada), 2005

A Thesis
Presented to Ryerson University
in partial fulfillment of the
requirements for the degree of
Master of Applied Science
in the Program of
Mechanical Engineering

Toronto, Ontario, Canada, 2008

Author's Declaration

I hereby declare that I am the sole author of this thesis. I authorize Ryerson University to lend this thesis to other institutions or individuals for the purpose of scholarly research.

I further authorize Ryerson University to reproduce this thesis by photocopying or by other means, in total or in part, at the request of other institutions or individuals for the purpose of scholarly research.

Abstract

By

Ardian Dudi Janura

DESIGN OF A PROTOTYPE BIORESORBABLE
TIBIAL IMPLANT IN A SHEEP MODEL

MASc, Mechanical Engineering
Ryerson University, Toronto, Canada, 2008

The purpose of this study was the design of a prototype calcium polyphosphate tibial implant for implantation into a sheep. In the design, several design parameters were considered: CPP implant structural strength, the maximum allowed micromotion of the structure at the interface with bone and the possibility of the surgeon implementing the necessary geometric changes on the bone elements during implant surgical insertion.

A finite element analysis facilitated the design and allowed for the effects of the various geometric parameters investigated. This analysis was based on a real solid model of the sheep tibial bone based on the CT scans of a five year old sheep, and several were the geometric parameters investigated.

The approach of the finite element analysis was very conservative, in the meaning that the load applied was purposely increased in order to account for any possibly unknown factors that may exist and not implemented in the analysis.

Acknowledgments

Thank you to my supervisor, Dr. Marcello Papini. His availability throughout my project was second to none and there always was great encouragement when problems seemed insurmountable. I would also like to thank Dr. Donatus Oguamanam, the co-supervisor for his great support during the project.

I would also like to thank Dr. Paul Zalzal and Dr. Bob Pilliar for the important and constructive advice that they gave me freely many times throughout my studies. I wish to acknowledge the data provided by Dr. Rita Kandel, Dr. Mark Huring, which was available whenever it was needed. Thank you to Dr J. Wang, of the University of Dentistry at University of Toronto, without whose the help the mechanical testing would never have taken place.

I am indebted to both the Canadian Institute of Health Research (CIHR) and Canadian Arthritis Network (CAN) for financing the project.

I would also like to thank my Mom for her consistent support and encouragement. Finally, for her ceaseless help and support during my studies and for her incredible patience I would like to say ..... Thank You Albana

TABLE OF CONTENTS

LIST OF TABLES

CHAPTER 2

CHAPTER 3

CHAPTER 4

CHAPTER 5

CHAPTER 6

LIST OF FIGURES

CHAPTER 1

CHAPTER 2

CHAPTER 3

CHAPTER 4

CHAPTER 5

CHAPTER 6

LIST OF APPENDIXES

NOMENCLATURE

CPP	Abbreviation of Calcium Polyphosphate ceramics
a_{ij}	Coefficients of matrix deformation of generalized Hook's law
A_{ij}	Elastic coefficients of equivalent Hook's law
$\bar{V}$	Strain energy of deformation per unit volume
$\sigma_x\ \sigma_y\ \sigma_z$	Normal stresses in x, y, and z directions
$\tau_{xy}, \tau_{yz}, \tau_{xz}$	Shear stresses in xy, yz, and xz planes respectively
$E_{xx}E_{yy},E_{zz}$	Yong's modulus in x, y, and z directions
$G_{xy}\ ,G_{yz}\ ,G_{xz}$	Shear modulus in xy, yz, and xz planes
$\eta_{yz,x}\ \eta_{xz,x.,..}\ \eta_{xy,z}$	Coefficients of mutual influence of the first kind
$\eta_{y,xz}\ \eta_{y,yz...}\ \eta_{yz,x}$	Coefficients of mutual influence of the second kind
$\mu_{xy,zx}, \mu_{xz,zy},..., \mu_{yz,xy}$	Coefficients characterizing the shear in one plane induced by shear acting on one of its orthogonal planes
$\nu_{xy}, \nu_{yz},... \nu_{xz}$	Poison's ratios
$\varepsilon_x, \varepsilon_y, \varepsilon_z$	Normal Strain in x, y, and z directions
$\gamma_{xy}, \gamma_{yz}, \gamma_{xz}$	Shear strain in xy, yz, and xz planes
f^B	Externally applied load
f^{s_f}	Surface traction
R_C^i	Concentrated loads
$\bar{U}$	Virtual displacement
$\bar{\varepsilon}$	Virtual strain
$W^\gamma(C)$	Strain energy function of body B^γ in contact
Π^γ	total potential energy of interacting bodies
$b.(y)$	Standard boundary conditions
$g.(y)$	Unilateral contact constraints
g_N	Non-penetration condition gap function

g_T	Relative tangential contact displacement
$\dot{g}_T$	Relative tangential velocity of the contact pair
Π_c^{LM}	Total potential energy expressed by Lagrange multipliers
Π_C^P	Total potential energy expressed by penalty terms
Π_N^{AM}	Total potential energy expressed by augmented Lagrange Terms.
p_N	Normal component of contact pressure
$\bar{t}_T^{\beta}$	Tangential component of contact stress
μ	Friction coefficient of two contact bodies

CHAPTER 1

Introduction and Background

1.1 Introduction

Hyaline cartilage is the load bearing medium located at the end of the long bones of synovial joints such as knee, hip, fingers etc. Due to the very limited ability to repair itself, damage of the Hyaline cartilage (also known as articular cartilage) either by trauma or disease can permanently affect the functionality of the joint. Damage of the articular cartilage can lead to instability, and deformities that, depending on the location of the joint, can greatly affect even the simplest tasks of the everyday life. The most common symptoms of damaged articular cartilage (arthritis) include pain, inflammation of surrounding structures, stiffening and swelling of the joint.

The three most common forms of arthritis are: Osteoarthritis (OA), Rheumatoid arthritis (RA), and Post traumatic arthritis (PTA). Osteoarthritis is the most common form of knee arthritis and is mostly found in the elderly of age above 60. OA is a slow progressive degenerative disease in which the articular cartilage gradually wears away due to the physical stress. RA is an inflammatory type of arthritis that can destroy the joint cartilage and can be found at any age. The third type, PTA, is similar to OA and may develop years after a fracture, ligament injury, or meniscus tear.

Nowadays, several techniques are available to restore or repair damaged articular cartilage [1, 2]. Most of the techniques available are focused in using autologus chondrocyte implantations. The cartilage for this procedure is harvested from a non-weightbearing area of the knee, and the number of chondrocytes is expanded in a culture medium and then re- implanted into the defective periosteal flap [3-5]. The success rate for this type of procedure is estimated to be 50-80% [6, 7, 8, and 9]. A number of complications may be experienced by the patients, mainly: incomplete restoration of the hyaline articular cartilage, ack of long- term stability of the repaired tissue [7, 8, and 10], and graft detachment.

Another widely advocated technique is the osteochondral transplantation (mosaicplasty) [11, 12, 13, 14, and 15]. In this procedure, osteochondral plugs are taken from the peripheries of both femoral condyles at the level of the patellofemoral joint and inserted as a mosaic to fill the defect. There are several advantages associated with this procedure such as the fact that the defect can be filled immediately with mature, hyaline

articular cartilage, and that there is the same treatment for both chondral and osteochondral defects. There are two main concerns associated with this procedure. Morbidity is a concern, limiting the area of the articular cartilage to be repaired by this method to 4 cm^2 [15] and secondly the possibility of lateral integration, a rare occurrence [16], can result in cyst formation as result of penetration of synovial fluid into the subchondral layer. The success rates for this procedure are reported to be 92% and 87% for femoral condyle and tibia plateau mosaicplasty [15].

Allogeneic osteochondral grafts are another technique in which the damaged cartilage is replaced by healthy articular cartilage usually extracted from cadavers. Success rates for this procedure range between 65 %and 85% for a follow up period of more than 10 years [17-19]. However, there are several drawbacks related to this method, such as the scarcity of the donor material, problems related to the storage and handling of the frozen tissue, as well as the risk of disease transmission. Despite the risks and the problems, this technique has been shown to be very successful; many patients with large osteochondral defects have greatly benefited from this type of treatment.

Applied mainly to young athletes, microfracture is another technique which is used to induce cartilage growth by stimulating a spontaneous repair reaction. For this technique, it is recommended that very small holes, 0.5-1 mm diameter, and at a depth of 2-2.5 mm, be generated throughout the articular cartilage lesions. A decline in the success of this technique is observed for five years after its application for articular cartilage repair [20].

In severe cases, where the articular cartilage defects are large, the knee is resurfaced with metal and plastic implants. They are designed to maintain the functionality of the joint only in forward and backward direction. Both femoral and tibia components are produced from titanium or cobalt-chromium alloys and the sliding between them is achieved by the presence of high-molecular-weight polyethylene. Total joint implants have been used for a period of 20 years with satisfactory success rates. These success rates are reduced to 20% for a follow-up period of 10 years raising questions with the viability of the method [21, 22].

Recent efforts have been focused in developing new treatment based on the bioengineering of articular cartilage which would have the potential to address all the

problems and complications associated with the methods mentioned above. The basic concept is the *in vitro* generation of an osteochondral type plug of cartilaginous tissue on top of porous ceramic substrate. In the work of Dr. Kandel [11,23], a sheep model has been used, and cartilaginous tissue is derived from sheep (6-9 month old) by sequential enzymatic digestion, and placed on top of a calcium polyphosphate (CPP) material [11, 23]. The use of ceramic porous materials such as CPP is desirable due to the osteogenity and biocompatibility that these materials exhibit. Osteogenity is dependent on the porosity of the ceramics, and encourages bone ingrowth into pores, finally enabling a secure fixation of the implant into the bone as well as a secure anchoring of the in-vitro formed cartilaginous tissue. The ultimate aim is the total replacement of the CPP scaffold by the ingrown bone tissue, in theory achievable if the scaffold satisfies two requirements: firstly, bone ingrowth is possible for pore openings varying from 100-300μm to enable a normal bone remodeling process [24], and secondly bone ingrowth is compromised for micromotion between implant and bone interfaces greater that 50μm.

The major concern related to the use of ceramics in general as bone substitute materials is their low tensile strength. Initial studies suggest that the initial tensile strength of the ceramic implant must be higher than tensile strength of the cancellous bone, i.e., in the range of 3-20MPa [25]. A CPP material satisfying this requirement has developed, as shown by the work of Pilliar's group [26, 27].

Stability of the implant and subsequently the success of this method are also determined by the geometrical structure of the implant and the anchorage method. These factors can be determined with the help of finite element (FE) analysis which is a computerized numerical technique that is used to obtain approximated solutions of a set of partial differential equations that predict the response of physical system subject to external loads. This forms the basis for the present thesis.

1.2 Anatomy of the Human Knee

The Knee is the largest joint in the human body and its constituents are the femur, tibia, patella, ligaments, and cartilage. The purpose of the knee is the transformation of the biological loads between the femur, tibia, fibula, and patella. This load transfer is controlled by the large ligaments which provide not only the connection between the bony structures of the knee (Femur, Tibia, and Fibula) but also the bracing of the joint against any abnormal type of motion. There are four major ligaments present in human knee: the anterior cruciate ligament (ACL), the medial collateral ligament (MCL), the posterior cruciate ligament (PCL), and the lateral collateral ligament (LCL). A schematic diagram of the human knee is shown in Fig. 1.1.

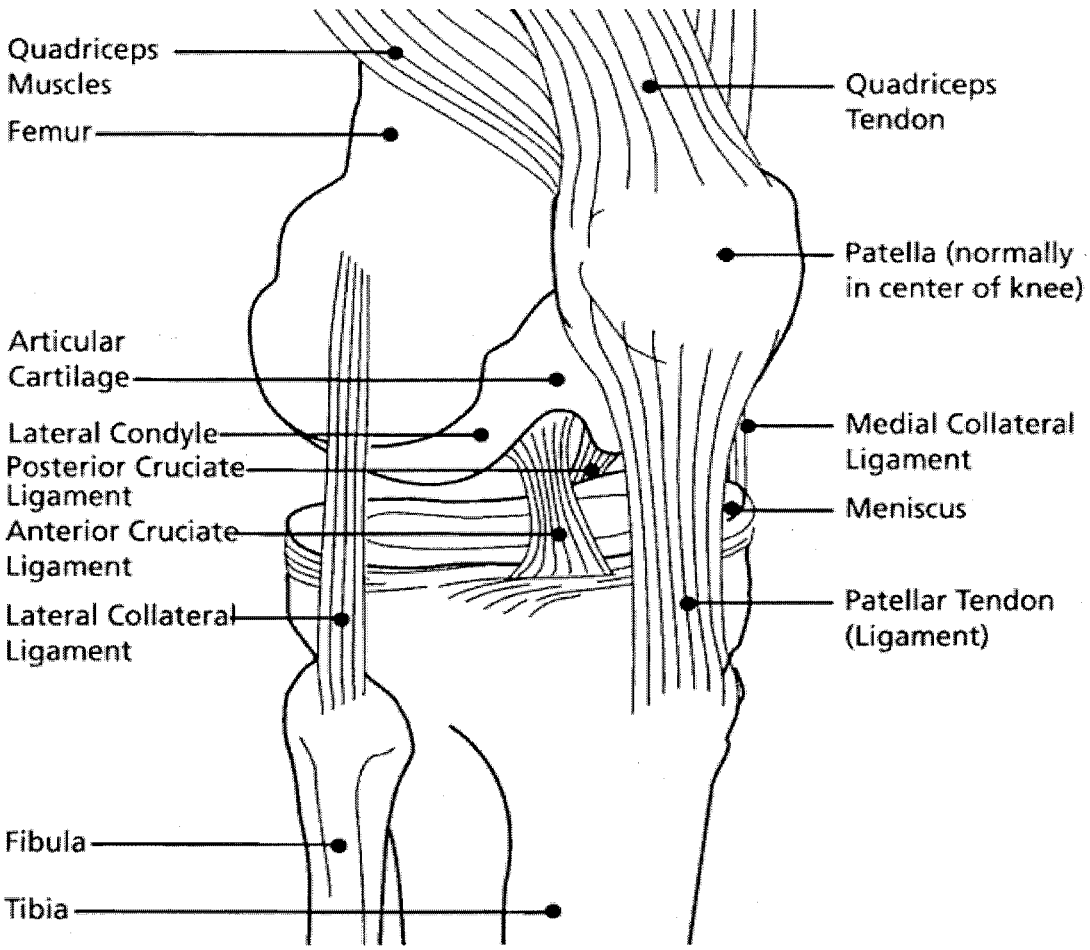

Figure 1.1 Anatomy of the human knee. Distal femur, proximal tibia, proximal fibula. (Picture reproduced from [28])

Other parts of the knee are the cartilage layers covering the ends of the distal end of the femur and proximal end of the tibia, and menisci. The cartilage serves as a shock absorption medium during movements, while the meniscus is a tough rubber like cartilage that is attached to the knee's ligaments and has two main functions: protection of the end bones (femur and tibia) from rubbing against each other and it also serves as a shock absorber.

1.2.1 Bone structure and functions

Bone is highly vascular and mineralized connective tissue which is characterized by its growing mechanism, hardness and its capability to remodel itself. Some of the key functions performed by the bone are: to provide structural support and protection for organs, to maintain the mineral homeostasis, and it is the primary site for the synthesis of blood cells.

Bone is a dense multi-phase composite, which is made-up of cells embedded in an organized matrix which contains both organic and inorganic elements, and water. The structure and the proportions of its components are dependent on the species, age, site and history, resulting in many different classifications of bone possessing various mechanical properties. It has the capability to continuously remodel, throughout the organism lifetime, in response to the changing mechanical conditions, always maintaining an optimal balance between geometrical form and function. Bones are classified into two different tissue types: cortical and cancellous bone. Both of these types of bone have the same composition, which can be split into three components: water, organic and mineral where the percentage of each constituent is dependent on the species. For human cancellous bone, the ratio between the water, organic and mineral constituent is 20%, 30%, and 50% respectively [2]. The ratio between the organic and inorganic constituents for humans is 33% and 67% respectively.

The organic portion of the bone contains 10% noncollagenous proteins where its presence is not directly related to the mechanical properties but to its maintenance. The main constituents of this portion are proteoglycans and osteocalcin proteins which are linked with the remodeling process of the bone [2-5], phospholipids and osteopontin

proteins, which are linked to the degree and control of mineralization, and lastly the morphogenetic protein, which is linked to the osteoinductive properties of the bone itself [3-5]. The remaining 90% of the organic material contains predominantly Type I collagen in combination with small quantities of Type III, IV, and V.

The mineral matrix is a mixture of calcium phosphate (Ca_3 $(PO_4)_2$), calcium hydroxide (Ca $(OH)_2$) and phosphate ions in crystallized form of hydroxyapatite ($Ca_{10}(PO_4)_6(OH)_2$). The hydroxyapatite is found not in the pure form but incorporated with other compounds and ions such as citrate, carbonate, Na, Mg, and HPO_4 [4, 5, and 29].

Cortical bone, also known as compact bone, contributes roughly 80% of the total body weight. It has 70% solid volume fraction and is extremely hard, formed with stacked layers. It can be considered a composite material with a density varying between 1.7 – 2.3 g/cm^3 and with a porosity varying from 5 – 30% [2, 3]. Cortical bone is a very compact medium where the porosity is due to the central canals of the Haversian system allowing passages for blood vessel, cancliculi the interconnecting pathways between lacunae, and resorption cavities cause by the remodeling process occurring in any bone [30]. A schematic diagram of the microstructure of the cortical bone is shown in Fig. 1.2A.

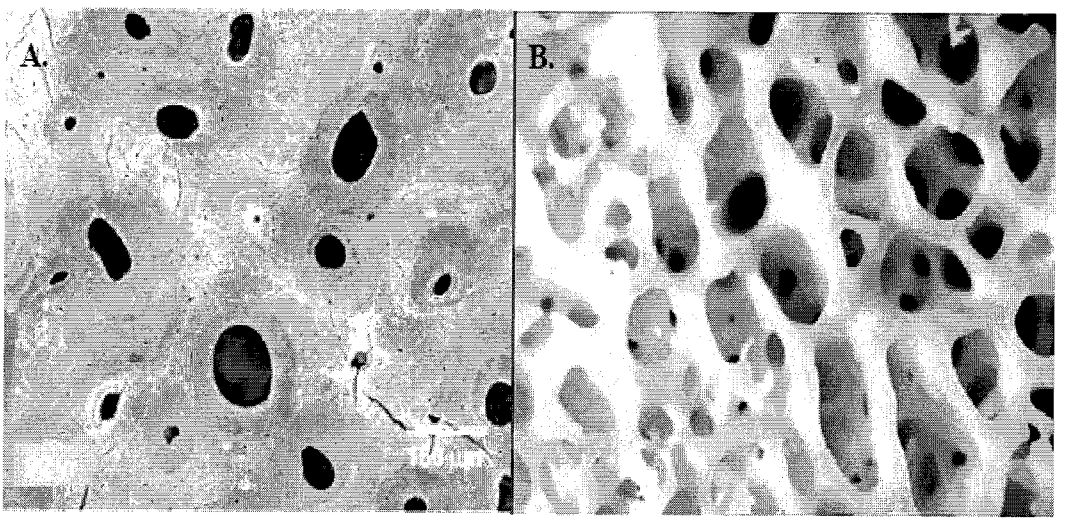

Figure 1.2 Image of microstructure of: A) Cortical bone from the femur of a 92 year old male. B) Cancellous bone of a 69 year old osteoarthritic male. (Picture reproduced from [11])

Cancellous bone, also known as trabecular or spongy bone has the same cellular composition as the cortical bone with a difference only on the material density which varies from 1.6-1.9 g/cm^3. The porosity of the structure varies from 30 % to a maximum value of 90% [2]. The microstructure of the cancellous bone is shown in the Fig. 1.2B.

1.2.2 Cartilage

There are three type of cartilage present in human body: 1) hyaline cartilage, 2) fibrocartilage and 3) elastic cartilage. Hyaline cartilage, also known as articular cartilage, is found at diarthroidal joints covering the extremities of the long bones. Articular cartilage is a load bearing hydrated connective tissue with the primary composition of proteoglycans and type II collage. It is a nonhomogenous medium where the thickness, density, and alignment of collagen fibrils vary with depth from the cartilage surface, enforcing depth dependent properties.

Depending on the collagen content and fibril orientation, the cartilage layer, as shown in Fig. 1.3, is divided in four zones. At the zone near the surface, the superficial zone, the collagen content is at 85% by dry weight and the fibril are oriented tangent to the surface indicating the shear bearing purpose of this zone. The collagen content drops to 68% at middle zone, approaching the value at the tide mark [31, 32].

The mechanical behavior of the cartilage layer is determined by the interaction of the two phases present: the fluid and matrix phases. The fluid phase contains water and electrolytes, where the water content for the articular cartilage rages from 68-85%. The solid phase contains type II collagen, proteoglycans, glycoprotein and chondrycyte; the last of which is responsible for construction of the cartilage matrix. Collagen content ranges from 10-20% while proteoglycans content varies from 5-10% [31, 32].

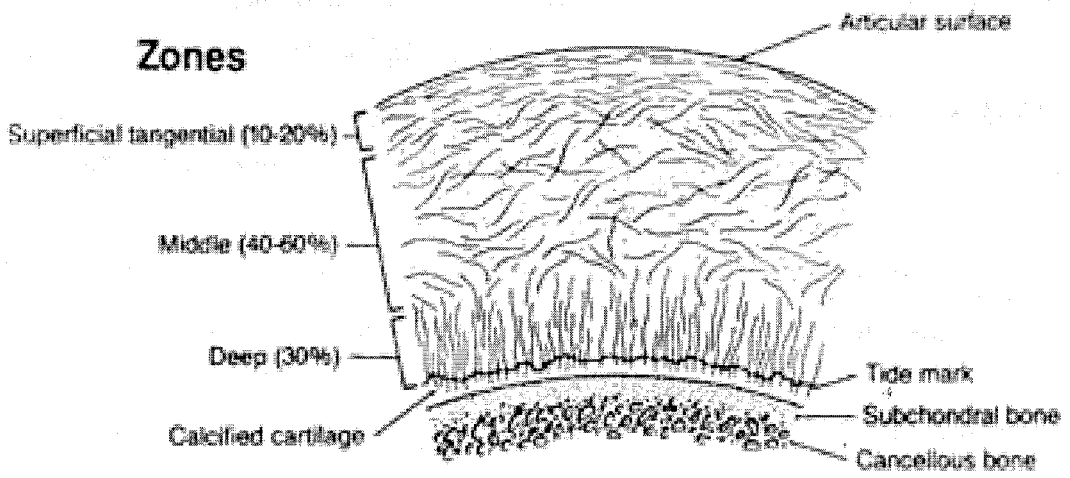

Figure 1.3 Schematic representation of cartilage layer. (Picture reproduction from [31])

1.3 Calcium Polyphosphate scaffolds as bone substitute material

1.3.1 Fabrication of CPP implants

Calcium polyphosphate for use in bone scaffold applications is produced by the process of thermal decomposition (calcination) of the calcium phosphate monobasic mondydrate (Ca $(H_2PO_4)_2(H_2O)$) at a temperature 500^0C for a period of 10 hours [33, 34]. The resulting powder from this process is heated at 1100^0C, until the melting point is reached, and then held for one hour at this temperature, in order to induce chain lengthening. The resulting frit, after quenching, is milled and scanned in order to achieve a particle with a size ranging between 75-106 μm. This raw material has been used in previous studies to manufacture, using gravity sintering, simple cylindrical shaped plug implants. [6, 27, 33]. In the present work, a much more complicated implant will be designed and tested, and the CPP implant was produced by the Solid freeform fabrication (SFF) process, and more specifically with Stereolithography (SLA) [33].

1.3.2 Calcium polyphosphate mechanical characteristics.

The use of ceramics as a bone substitute material has been the subject of many recent studies, because of their desirable characteristics such as osteogenity and biocompatibility. In particular, calcium polyphosphate (CPP) has been extensively studied and shown to be extremely biocompatible, having calcium orthophosphate, a naturally metabolizable substance, as its product of degradation within the human body [27]. Other important features such as the initial mechanical strength, and the rate of degradation of the CPP material have been investigated in [26, 27, 33], where the studies were accomplished both under *in vivo* and *in vitro* conditions. Grynpas et al. [27] showed that there is a dependency of the above characteristics on the particle sizes used in the CPP implant under *in vitro* conditions. The parameters analyzed, as a function of particle size, during the life span of the CPP implants were CPP degradation rate, bone ingrowth degree, and variation of the mechanical strength of the implant.

According to [27], the degradation rate was found to be inversely proportional to the particle size used in the CPP implant. It was found that for the implant with the finer size (45-105μm) degradation was estimated for a 6 week and 1 year period to be 47 and 57%, respectively. For an implant with medium sized particles (106-150μm), degradation was estimated to be 29 and 33% respectively, while for the largest sized particles (150-250μm) degradation was 9.5 and 14% respectively. The principal reason for the particle size dependency on the rates of degradation is related to the fact that for small particle size the zones of bonding of CPP particles are of greater atomic disorder making them susceptible to degradation.

Another reason affecting not only the rate of degradation but the bone ingrowth process as well is the type of bone that the CPP material is contact with. Being more vascular than the cortical bone, at contact areas between cancellous bone and CPP material both processes occur at a faster rate.

In vitro studies of the CPP material showed that the mechanical strength is heavily dependent on the powder particle size [33]. Tensile strength testing was performed on two particle sizes: the fine power with particle size ranging between 106-150μm and the coarse with particle size of 150-250 μm. The initial tensile strengths for

fine and coarse powder CPP material were measured to be 24 and 5.9 MPa, respectively. The effect of aging under *in vitro* conditions was measured for a period of 30 days, with the resulting tensile strength for the specimens for fine power reduced to 8.0 MPa and for coarse powder reduced to 1.9 MPa. In this study, it was discovered that in both cases, fine and coarse power, the strength is reduced very rapidly in the initial stage of the aging process, followed by a more gradual decrease over time.

1.4 Thesis Objectives

The research was conducted as part of the Canadian Institutes of Health Research (CIHR) Bioengineering of Skeletal Tissues Team, a Canada wide team of researchers, of which the author's supervisor is a member, working toward developing bioengineered tissue replacements for arthoplasty. The author was the only member of the team working on the design of the implant.

The purpose of this study was thus to design a prototype calcium polyphosphate (CPP) tibial plaeau implant for implantation into a sheep model. In the design, a number of important factors had to be considered. Firstly, the strength and stability of the implant had to be such that it would not fail under a worst case simulated *in vivo* loading. Secondly, the maximum allowed micromotion of the implant at its interface with bone was limited to ensure bone ingrowth could occur. Finally, the ease of implantation had to be considered, so that the implant could be easily inserted by the surgeon using readily available surgical tools. The study will establish a methodology for the design and analysis of bone scaffold based arthoplasty joints in an animal model, and it represents the first step towards the implementation of the technology in articular cartilage repair of a full joint in humans.

CHAPTER 2

Material Models and Contact Boundary Problem

In this chapter, the theoretical background needed to understand various aspects of the implant design will be presented. First, the material model used in the design of the implant will be briefly presented. This will be followed by a brief introduction to the Finite Element Method, and a discussion of the contact boundary approaches used in the finite element analysis.

2.1 Material Models

This section presents the constitutive equations of the various materials considered in this thesis. A detailed description can be found at the book by Lekhntskii [34]. During the comparative stage of the design, isotropic type material properties were assumed for the cortical bone, cancellous bone, Calcium Polyphosphate implant, and titanium screw. Anisotropic material properties were used at a later stage, applied only in the final design, with the purpose of quantifying the effect the isotropic assumption against the real anisotropic properties of the bone elements. At this stage, the cortical bone was considered to be transversely anisotropic, while the cancellous bone was homogenous and anisotropic. Calcium Polyphosphate (CPP) implant and titanium screw were assumed to exhibit isotropic properties in all cases.

2.1.1 Generalized Hooke's Law for Anisotropic Materials

To obtain the relationship between the components of stress and strain in an elastic body, it is assumed that the components of strain are linear functions of components of stress. In the general case of a homogenous anisotropic body, the generalized Hook's Law in Cartesian coordinates has the form:

$$\begin{bmatrix} \varepsilon_x \\ \varepsilon_y \\ \varepsilon_z \\ \gamma_{yz} \\ \gamma_{xz} \\ \gamma_{xy} \end{bmatrix} = \begin{bmatrix} a_{11} & a_{12} & a_{13} & a_{14} & a_{15} & a_{16} \\ a_{21} & a_{22} & a_{23} & a_{24} & a_{25} & a_{26} \\ a_{31} & a_{32} & a_{33} & a_{34} & a_{35} & a_{36} \\ a_{41} & a_{42} & a_{43} & a_{44} & a_{45} & a_{46} \\ a_{51} & a_{52} & a_{53} & a_{54} & a_{55} & a_{56} \\ a_{61} & a_{62} & a_{63} & a_{64} & a_{65} & a_{66} \end{bmatrix} \begin{bmatrix} \sigma_x \\ \sigma_y \\ \sigma_z \\ \tau_{yz} \\ \tau_{xz} \\ \tau_{xy} \end{bmatrix} \tag{2.1}$$

Solving the above system of equations for stress components σ_x, σ_y, σ_z, τ_{yz}, τ_{xz}, τ_{xy}, the equivalent form of generalized Hooke's law is obtained:

$$\begin{bmatrix} \sigma_x \\ \sigma_y \\ \sigma_z \\ \tau_{yz} \\ \tau_{xz} \\ \tau_{xy} \end{bmatrix} = \begin{bmatrix} A_{11} & A_{12} & A_{13} & A_{14} & A_{15} & A_{16} \\ A_{21} & A_{22} & A_{23} & A_{24} & A_{25} & A_{26} \\ A_{31} & A_{32} & A_{33} & A_{34} & A_{35} & A_{36} \\ A_{41} & A_{42} & A_{43} & A_{44} & A_{45} & A_{46} \\ A_{51} & A_{52} & A_{53} & A_{54} & A_{55} & A_{56} \\ A_{61} & A_{62} & A_{63} & A_{64} & A_{65} & A_{66} \end{bmatrix} \begin{bmatrix} \varepsilon_x \\ \varepsilon_y \\ \varepsilon_z \\ \gamma_{yz} \\ \gamma_{xz} \\ \gamma_{xy} \end{bmatrix} \tag{2.2}$$

The systems of equations (2.1) and (2.2) contain 36 coefficients, the coefficients of deformation a_{ij}, and A_{ij}, the elastic coefficients (moduli of elasticity). Materials that exhibit such stress-strain relations involving a number of independent elastic coefficients are said to be anisotropic. For a given temperature, time and location in the body, the coefficients a_{ij} and A_{ij} are constants that are characteristics of a given material.

Assuming that the body undergoes deformation under load isothermally, and denoting the elastic potential by $\bar{V}$ (representing the strain energy of deformation per unit volume), the following relations result:

$$\sigma_x = \frac{\partial \bar{V}}{\partial \varepsilon_x} \quad , \quad \sigma_y = \frac{\partial \bar{V}}{\partial \varepsilon_y} \quad , \ldots, \quad \tau_{xy} = \frac{\partial \bar{V}}{\partial \gamma_{xy}} \tag{2.3}$$

Differentiating expressions in (2.3) with respect to $\varepsilon_x, \varepsilon_y, \ldots, \gamma_{xy}$ gives:

$$\left.\begin{aligned} \frac{\partial \sigma_x}{\partial \varepsilon_y} &= \frac{\partial \sigma_y}{\partial \varepsilon_x} \\ \frac{\partial \sigma_x}{\partial \varepsilon_z} &= \frac{\partial \sigma_y}{\partial \varepsilon_x} \\ &\cdots \\ \frac{\partial \tau_{xy}}{\partial \gamma_{yx}} &= \frac{\partial \tau_{yx}}{\gamma_{xy}} \end{aligned}\right\} \tag{2.4}$$

Hence, it follows that the matrices of the elastic coefficients in eqs. (2.1) and (2.2) are symmetric.

$$\begin{cases} a_{12.} = a_{21}; \quad a_{23} = a_{32}; \quad a_{13.} = a_{31}; \quad \ldots; \quad a_{65} = a_{56}; \\ A_{12} = A_{21}; \quad A_{23} = A_{32}; \quad A_{13} = A_{31}; \quad \ldots; \quad A_{65} = A_{56} \end{cases} \tag{2.5}$$

Therefore, the number of the coefficients in expressions (2.1) and (2.2) for the generalized anisotropic material is reduced from 36 to 21 independent coefficients.

In the generalized case, the expression of the elastic potential per unit volume has the form:

$$\begin{aligned} \bar{V} &= \frac{1}{2} a_{11}\sigma_x^2 + a_{12}\sigma_x\sigma_y + a_{13}\sigma_x\sigma_z + a_{14}\sigma_x\tau_{yz} + a_{15}\sigma_x\tau_{xz} + a_{16}\sigma_x\tau_{xy} \\ &+ \frac{1}{2} a_{22}\sigma_y^2 + a_{23}\sigma_y\sigma_z + a_{24}\sigma_y\tau_{yz} + a_{25}\sigma_y\tau_{xz} + a_{26}\sigma_y\tau_{xy} + \frac{1}{2} a_{33}\sigma_z^2 \\ &+ a_{34}\sigma_z\tau_{yz} + a_{35}\sigma_z\tau_{xz} + a_{36}\sigma_y\tau_{xy} + \frac{1}{2} a_{44}\tau_{yz}^2 + a_{45}\tau_{yz}\tau_{xz} + a_{46}\tau_{yz}\tau_{xy} \\ &+ \frac{1}{2} a_{55}\tau_{xz}^2 + a_{56}\tau_{xz}\tau_{xy} + \frac{1}{2} a_{66}\tau_{xy}^2 \end{aligned} \tag{2.5}$$

The above expression, using the symmetry of the elastic coefficients, can be written in a more simplified form as:

$$\bar{V} = \frac{1}{2}\left(\sigma_x \varepsilon_x + \sigma_y \varepsilon_y + \sigma_z \varepsilon_z + \tau_{yz}\gamma_{yz} + \tau_{xz}\gamma_{xz} + \tau_{xy}\gamma_{xy}\right) \tag{2.6}$$

Similar to expression (2.5), the elastic potential per unit volume can be written as a function of deformation components as follows:

$$\bar{V} = \frac{1}{2} A_{11}\varepsilon_x^2 + A_{12}\varepsilon_x\varepsilon_y + \ldots + \frac{1}{2} A_{22}\varepsilon_y^2 + \ldots A_{26}\varepsilon_Y\gamma_{xy} + \ldots \frac{1}{2} A_{66}\gamma_{xy}^2 \tag{2.7}$$

The potential energy of the deformation for the whole body is then found by means of integration over its volume W:

$$V = \iiint_W \bar{V}\, dw \tag{2.8}$$

In the case of general anisotropy, the elastic coefficients in eq. (2.1) are assembled into six groups corresponding to similarities in characteristics within each group:

I. $$a_{11} = \frac{1}{E_{xx}}, \qquad a_{22} = \frac{1}{E_{yy}}, \qquad a_{33} = \frac{1}{E_{zz}}; \tag{2.9}$$

II. $$a_{12} = -\frac{\nu_{yx}}{E_{xx}} = -\frac{\nu_{xy}}{E_{yy}}, \qquad a_{23} = -\frac{\nu_{zy}}{E_{yy}} = -\frac{\nu_{yz}}{E_{zz}},$$

$$a_{13} = -\frac{\nu_{xz}}{E_{zz}} = -\frac{\nu_{zx}}{E_{xx}}; \tag{2.10}$$

III. $$a_{44}=\frac{1}{G_{yz}},\qquad a_{55}=\frac{1}{G_{xz}},\qquad a_{66}=\frac{1}{G_{xy}};\tag{2.11}$$

IV. $$a_{56}=\frac{\mu_{xy,zx}}{G_{xz}}=\frac{\mu_{zx,xy}}{G_{xy}},\qquad a_{46}=\frac{\mu_{xy,yz}}{G_{yz}}=\frac{\mu_{yz,xy}}{G_{xy}},$$

$$a_{45}=\frac{\mu_{zx,xy}}{G_{yz}}=\frac{\mu_{yz,zx}}{G_{xz}};\tag{2.12}$$

V. $$a_{14}=\frac{\eta_{yz,x}}{E_{xx}}=\frac{\eta_{x,yz}}{G_{yz}},\qquad a_{25}=\frac{\eta_{zx,y}}{E_{yy}}=\frac{\eta_{y,zx}}{G_{xz}},$$

$$a_{36}=\frac{\eta_{xy,z}}{E_{zz}}=\frac{\eta_{z,xy}}{G_{xy}};\tag{2.13}$$

VI. $$a_{24}=\frac{\eta_{yz,y}}{E_{yy}}=\frac{\eta_{y,yz}}{G_{yz}},\qquad a_{35}=\frac{\eta_{zx,z}}{E_{zz}}=\frac{\eta_{z,zx}}{G_{xz}},$$

$$a_{16}=\frac{\eta_{xy,x}}{E_{xx}}=\frac{\eta_{x,xy}}{G_{xy}},\qquad a_{34}=\frac{\eta_{yz,z}}{E_{zz}}=\frac{\eta_{z,yz}}{G_{yz}},$$

$$a_{15}=\frac{\eta_{zx,x}}{E_{xx}}=\frac{\eta_{x,zx}}{G_{xz}},\qquad a_{26}=\frac{\eta_{xy,y}}{E_{yy}}=\frac{\eta_{y,xy}}{G_{xy}};\tag{2.14}$$

In expressions (2.9) through (2.14) E_{xx}, E_{yy}, E_{zz} are the Young's moduli in three orthogonal directions, the x, y, and z directions; G_{yz}, G_{xz}, G_{xy} denote the shear moduli for shear deformation in the y-z , x-z, and x-y planes , respectively; Coefficients $\mu_{zx,yz}$, $\mu_{xy,yz},\ldots,$ $\mu_{yz,xy}$, characterize the shear stresses in planes that are parallel to one of the coordinate system's planes which induce tangential stresses parallel to the other coordinate system's plane. For example, $\mu_{yz,xy}$ characterizes the shear in the plane parallel

to the xy plane which induces the stress τ_{yz}. Coefficients $\eta_{yz,x}$, $\eta_{zx,x}$, …, $\eta_{xy,z}$ are called the coefficients of the mutual influence of the first kind. They characterize the stretching, for example, in the z-direction which is induced by the tangential stresses on plane xy. Lastly, coefficients $\eta_{x,yz}$, $\eta_{y,yz}$…, $\eta_{z,xy}$ are called the coefficients of mutual influence of the second kind, and characterize the shears in the planes parallel to the coordinate system's planes (e.g., yz-plane), under the influence of the of normal stresses (e.g., y-direction).

Poisson's ratios are denoted by ν_{yx}, ν_{zy}, ν_{xz}, ν_{xy}, ν_{yz}, ν_{zx}. They characterize the transverse tension (compression) for compression (tension) in a direction of the axis of the coordinate (e.g. ν_{yx} characterizes the decrease in x-direction as the result of tension in the y-direction).

With the introduction of the coefficients given by expressions (2.9) through (2.14) using the symmetry of the elastic coefficient's matrix at (2.1), the generalized Hooke's law can be written in the following way:

$$\varepsilon_x = \frac{1}{E_{xx}}\left[\sigma_x - \nu_{yx}\sigma_y - \nu_{zx}\sigma_z + \eta_{yz,x}\tau_{yz} + \eta_{zx,x}\tau_{zx} + \eta_{xy,x}\tau_{xy}\right] \tag{2.15}$$

$$\varepsilon_y = \frac{1}{E_{yy}}\left[-\nu_{xy}\sigma_x + \sigma_y - \nu_{zy}\sigma_z + \eta_{yz,y}\tau_{yz} + \eta_{zx,y}\tau_{zx} + \eta_{xy,y}\tau_{xy}\right] \tag{2.16}$$

$$\varepsilon_z = \frac{1}{E_{zz}}\left[-\nu_{xz}\sigma_x - \nu_{yz}\sigma_y + \sigma_z + \eta_{yz,z}\tau_{yz} + \eta_{zx,z}\tau_{zx} + \eta_{xy,z}\tau_{xy}\right] \tag{2.17}$$

$$\gamma_{yz} = \frac{1}{G_{yz}}\left[\eta_{x,yz}\sigma_x + \eta_{y,yz}\sigma_y + \eta_{z,yz}\sigma_z + \tau_{yz} + \mu_{zx,yz}\tau_{xz} + \mu_{xy,yz}\tau_{xy}\right] \tag{2.18}$$

$$\gamma_{xz} = \frac{1}{G_{xz}}\left[\eta_{x,zx}\sigma_x + \eta_{y,zx}\sigma_y + \eta_{z,zx}\sigma_z + \mu_{yz,zx}\tau_{yz} + \tau_{xz} + \mu_{xy,zx}\tau_{xy}\right] \tag{2.19}$$

$$\gamma_{xy} = \frac{1}{G_{xy}}\left[\eta_{x,xy}\sigma_x + \eta_{y,xy}\sigma_y + \eta_{z,xy}\sigma_z + \mu_{yz,xy}\tau_{yz} + \mu_{zx,xy}\tau_{xz} + \tau_{xy}\right] \tag{2.20}$$

Expressions (2.14) - (2.20) describe the generalized case of anisotropy where the material displays different material properties in all directions, thus the material does not exhibit any kind of symmetry. The number of independent elastic constant, as mentioned

above, is 21. Strain-stress relations are described by expressions (2.1) and (2.2) through elastic constants a_{ij} and A_{ij} which can be evaluated through technical coefficients by means of expressions (2.9) through (2.14).

If the material possesses symmetry of any kind, then it is reflected in its elastic properties, causing a reduction in the number of independent elastic coefficients. The degree of this reduction depends on the depth of the symmetry of the material. A brief description of some types of symmetry is given in the following section.

2.1.2 Elastic symmetry

If an anisotropic body possesses an elastic symmetry, then the equations of the generalized Hooke's law are simplified. The degree in which these equations are simplified depends on the degree of the symmetry resulting in the number of independent elastic constants to be reduced to 13, 9, or to a minimum of two (E, ν) which corresponds to the case of isotropic material or total symmetry.

The simplified form of the generalized Hooke's law, due to the symmetry of the material properties, is derived by the introduction of a second x', y', z' coordinate system, which is symmetric to the reference body coordinate system x, y, z, in accordance with the form of its elastic symmetry. Therefore, in the generalized Hooke's law, the expression for both coordinate systems will have identical elastic coefficients (coefficients a_{ij} at 2.1). Thus the elastic potential per unit volume for both coordinate systems will have the form:

For the reference system x, y, z:

$$\bar{V} = \frac{1}{2}a_{11}\sigma_x^2 + a_{12}\sigma_x\sigma_y + a_{13}\sigma_x\sigma_z + \ldots + \frac{1}{2}a_{66}\tau_{xy}^2 \qquad (2.21)$$

For the second system x', y', z':

$$\bar{V} = \frac{1}{2}a_{11}\sigma_x^{'2} + a_{12}\sigma_x^{'}\sigma_y^{'} + a_{13}\sigma_x^{'}\sigma_z^{'} + \ldots + \frac{1}{2}a_{66}\tau_{xy}^{'2} \tag{2.22}$$

Because the same quantity is evaluated by the above expressions, the following results:

$$\frac{1}{2}a_{11}\sigma_x^2 + a_{12}\sigma_x\sigma_y + \ldots + \frac{1}{2}a_{66}\tau_{xy}^2 = \frac{1}{2}a_{11}\sigma_x^{'2} + a_{12}\sigma_x^{'}\sigma_y^{'} + \ldots + \frac{1}{2}a_{66}\tau_{xy}^{'2} \tag{2.23}$$

The position of the second coordinate system (x', y', z') with respect to the reference system (x, y, z) is determined by direction cosines given in the following table:

Table 2.1 Direction Cosines

	x	y	z
x'	α_1	β_1	γ_1
y'	α_2	β_2	γ_2
z'	α_3	β_3	γ_3

where $\alpha_1 = cos\ (x, x')$, $\beta_3 = cos\ (y, z')$ and so forth. By projecting the stress components of the reference coordinate system into the new system, the components of stresses in the new system are obtained (in the areas normal to the new system axis) as:

$$\sigma_x^{'} = \sigma_x\alpha_1^2 + \sigma_y\beta_1^2 + \sigma_z\gamma_1^2 + 2\tau_{yz}\beta_1\gamma_1 + 2\tau_{xz}\alpha_1\gamma_1 + 2\tau_{xy}\alpha_1\beta_1 \tag{2.24}$$

$$\tau_{yz}^{'} = \sigma_x\alpha_2\alpha_3 + \alpha_y\beta_2\beta_3 + \sigma_z\gamma_2\gamma_3 + \tau_{yz}(\beta_2\gamma_3 + \beta_3\gamma_2) + \tau_{xz}(\alpha_2\gamma_3 + \alpha_3\gamma_2) + \tau_{xy}(\alpha_2\beta_3 + \alpha_3\beta_2) \tag{2.25}$$

The expressions for $\sigma_y^{'}$ and $\sigma_z^{'}$ are obtained by using expression (2.24) by substituting in the right hand side of this expression the proper coefficients of the indices α, β, and γ into (2.24), while the expressions for $\tau_{xy}^{'}$ and $\tau_{xz}^{'}$ are obtained by proper permutation of the same indices using the expression (2.22).

Substituting the expressions for $\sigma_x^{'},\sigma_y^{'},\sigma_z^{'}$, $\tau_{yz}^{'},\tau_{xz}^{'},\tau_{xy}^{'}$ into the right hand side of eq. (2.21) and equating the coefficients for similar terms, gives the result that, depending on the depth of the symmetry, many of the elastic coefficients become zero and others are related by defined variations. Therefore, bodies that exhibit symmetries will have a smaller number of independent elastic constants. The relationship between the moduli A_{ij} can also be obtained if elastic potential is expressed in terms of strain instead of stress.

2.1.3 One Plane of symmetry

In this type of symmetry, the elastic properties of the material are the same in two symmetric directions with respect to one plane. By directing the z-axis normal to the plane of elastic symmetry, the system of equations (3.1) takes the form:

$$\begin{bmatrix} \varepsilon_x \\ \varepsilon_y \\ \varepsilon_z \\ \gamma_{yz} \\ \gamma_{xz} \\ \gamma_{xy} \end{bmatrix} = \begin{bmatrix} a_{11} & a_{12} & a_{13} & 0 & 0 & a_{16} \\ & a_{22} & a_{23} & 0 & 0 & a_{26} \\ & & a_{33} & 0 & 0 & a_{36} \\ & & & a_{44} & a_{45} & 0 \\ S & Y & M & & a_{55} & 0 \\ & & & & & a_{66} \end{bmatrix} \begin{bmatrix} \sigma_x \\ \sigma_y \\ \sigma_z \\ \tau_{yz} \\ \tau_{xz} \\ \tau_{xy} \end{bmatrix} \tag{2.26}$$

In this type of symmetry, the number of independent material constants reduces to 13, as the coefficients a_{14}, a_{24}, a_{46}, a_{15}, a_{25}, a_{35}, a_{56} and the corresponding moduli coefficients A_{ij} at (2.2) become zero. The direction normal to the plane of symmetry is called the principal direction because during tension-compression applied in this direction, the segments normal to the plane of symmetry remain normal during deformation. Application of a stress in z-direction would lead to:

$$\begin{cases} \varepsilon_x = a_{13}\sigma_z \\ \varepsilon_y = a_{23}\sigma_z \\ \varepsilon_z = a_{33}\sigma_z \\ \gamma_{yz} = 0 \\ \gamma_{xz} = 0 \\ \gamma_{xy} = a_{36}\sigma_z \end{cases} \tag{2.27}$$

Hence in this type of symmetry, the body possesses only one principal direction.

2.1.4 Three planes of symmetry

In this type of symmetry, elastic planes passing in every point of the material are orthogonal with each other. By selecting a coordinate system with an axis perpendicular to the elastic planes, the generalized Hooke's law given by the system of equations in (2.1) becomes:

$$\begin{bmatrix} \varepsilon_x \\ \varepsilon_y \\ \varepsilon_z \\ \gamma_{yz} \\ \gamma_{xz} \\ \gamma_{xy} \end{bmatrix} = \begin{bmatrix} a_{11} & a_{12} & a_{13} & 0 & 0 & 0 \\ & a_{22} & a_{23} & 0 & 0 & 0 \\ & & a_{33} & 0 & 0 & 0 \\ & & & a_{44} & 0 & 0 \\ S & Y & M & & a_{55} & 0 \\ & & & & & a_{66} \end{bmatrix} \begin{bmatrix} \sigma_x \\ \sigma_y \\ \sigma_z \\ \tau_{yz} \\ \tau_{xz} \\ \tau_{xy} \end{bmatrix} \tag{2.28}$$

In addition to the elastic coefficients of the case of one plane of symmetry, constants a_{16}, a_{26}, a_{36}, and a_{45} become equal to zero. Therefore, the number of independent coefficients reduces to nine. The remaining elastic constants are called the principal constants: E_1, E_2, E_3 (Young's moduli), v_{12}, v_{21}, v_{23}, v_{32}, v_{13}, v_{31} (Poisson's ratio coefficients), and G_{12}, G_{13}, G_{23} (shear moduli). The system of eq. (3.23) can be written as a function of these coefficients as follows:

$$\begin{bmatrix} \varepsilon_x \\ \varepsilon_y \\ \varepsilon_z \\ \gamma_{yz} \\ \gamma_{xz} \\ \gamma_{xy} \end{bmatrix} = \begin{bmatrix} \frac{1}{E_1} & -\frac{\nu_{12}}{E_2} & -\frac{\nu_{13}}{E_3} & 0 & 0 & 0 \\ & \frac{1}{E_2} & -\frac{\nu_{23}}{E_3} & 0 & 0 & 0 \\ & & \frac{1}{E_3} & 0 & 0 & 0 \\ & & & \frac{1}{G_{23}} & 0 & 0 \\ & & & & \frac{1}{G_{13}} & 0 \\ S & Y & M & & & \frac{1}{G_{12}} \end{bmatrix} \begin{bmatrix} \sigma_x \\ \sigma_y \\ \sigma_z \\ \tau_{yz} \\ \tau_{xz} \\ \tau_{xy} \end{bmatrix} \tag{2.29}$$

where $E_1\nu_{21} = E_2\nu_{12}$, $E_2\nu_{32} = E_3\nu_{23}$, $E_3\nu_{13} = E_1\nu_{31}$.

Three principal directions are mutually orthogonal with each other, and a material exhibiting this type of symmetry is called orthogonally-anisotropic or simply orthotropic.

2.1.5 One plane of isotropy

If a body possesses an axis of symmetry of rotation, then all directions in the planes normal to this axis are equivalent with respect to the elastic properties and the body is isotropic in these planes. Generalized Hooke's law for materials exhibiting this type of symmetry, in the Cartesian coordinate system with the z-axis perpendicular to the plane of isotropy xy has the form:

$$
\begin{aligned}
\varepsilon_x &= \frac{1}{E}\left(\sigma_x - \nu\sigma_y\right) - \frac{\nu'}{E'}\sigma_z, \\
\varepsilon_y &= \frac{1}{E}\left(\sigma_y - \nu\sigma_x\right) - \frac{\nu'}{E'}\sigma_z, \\
\varepsilon_z &= \frac{\nu'}{E'}\left(\sigma_x - \sigma_y\right) + \frac{1}{E'}\sigma_z, \\
\gamma_{yz} &= \frac{1}{G'}\tau_{yz}, \\
\gamma_{xz} &= \frac{1}{G'}\tau_{xz}, \\
\gamma_{xy} &= \frac{1}{G}\tau_{xy} = \frac{2(1+\nu)}{E}\tau_{xy}.
\end{aligned}
\tag{2.30}
$$

where E and v are the Young's modulus and Poisson's coefficient, respectively, on the plane of isotropy, and E' and v' are the Young's modulus and Poisson's coefficient in the direction perpendicular to the plane of isotropy. Lastly, G and G' are the shear moduli for the planes perpendicular and parallel, respectively, to the plane of isotropy. A material exhibiting this type of elastic behavior is called transversely isotropic. The number of independent elastic coefficients in this type of symmetry is six.

2.1.6 Isotropic Materials

If a material exhibits identical properties in all directions so that any plane represents a plane of elastic symmetry, then the material is called isotropic. The number of independent elastic coefficient reduces to two: E and v (Young's modulus and Poisson's coefficient). In addition to the previously considered case of three-plane symmetry, the following relationships also hold:

$$
a_{33} = a_{11} \quad , \qquad a_{13} = a_{12} \quad , \qquad a_{44} = 2(a_{11} - a_{12}) \tag{2.31}
$$

The Hooke's law, after introducing the above simplification will take the following form:

$$\begin{bmatrix} \varepsilon_x \\ \varepsilon_y \\ \varepsilon_z \\ \gamma_{yz} \\ \gamma_{xz} \\ \gamma_{xy} \end{bmatrix} = \begin{bmatrix} \frac{1}{E} & -\frac{\nu}{E} & -\frac{\nu}{E} & 0 & 0 & 0 \\ & \frac{1}{E} & -\frac{\nu}{E} & 0 & 0 & 0 \\ & & \frac{1}{E} & 0 & 0 & 0 \\ & & & \frac{1}{G} & 0 & 0 \\ & & & & \frac{1}{G} & 0 \\ S & Y & M & & & \frac{1}{G} \end{bmatrix} \begin{bmatrix} \sigma_x \\ \sigma_y \\ \sigma_z \\ \tau_{yz} \\ \tau_{xz} \\ \tau_{xy} \end{bmatrix} \qquad (2.32)$$

where $G = \dfrac{E}{2(1+\nu)}$ is the shear modulus, and SYM indicates that the matrix is symmetric.

2.1.7 Cylindrical anisotropy

. Then an infinitesimally small element is bounded by three pairs of surfaces which are identical to the corresponding coordinate system surface, and the material is referred to as a curvilinear anisotropic material. In the case of a Cartesian coordinate system, the infinitesimally small material is bounded by a three pair of surfaces which coincide with the planes of the coordinate system.

Two forms of curvilinear anisotropy considered by St. Venant are: cylindrical and spherical anisotropy. The cylindrical anisotropy is defined as follows: All directions normal to a certain axis, the axis of anisotropy, have equivalent material properties. The infinitesimally small elements are bounded by two planes orthogonal to the axis of the anisotropy, by two planes passing through this axis and by two surfaces of coaxial

cylinders. A graphic representation of a cylindrical element in two-dimensions is given in Figure 2.1:

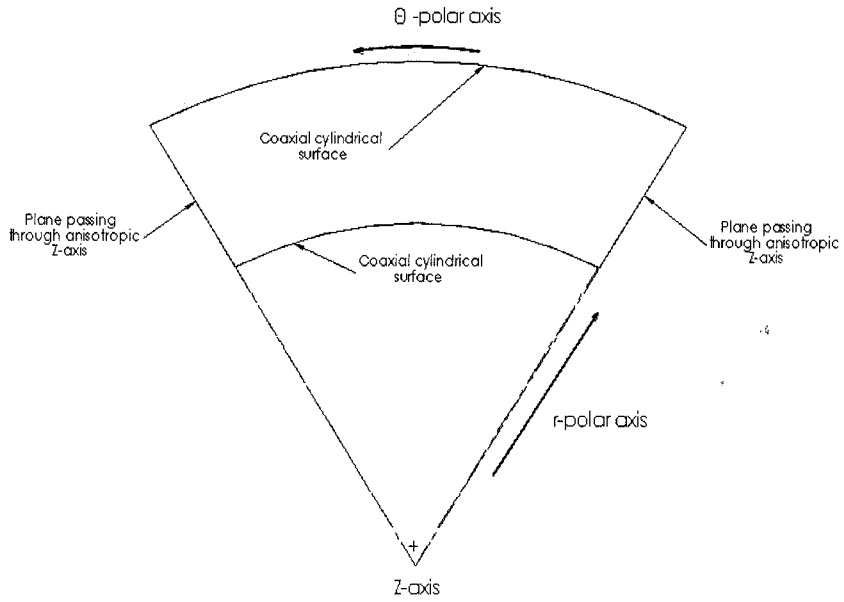

Figure 2.1 Infinitesimally small cylindrical anisotropic element. Anisotropic z-axis is normal to the page, and the two parallel planes orthogonal to the anisotropic axis defining the volumetric cylindrical anisotropic element are parallel to the page [1].

Considering the z-axis as the axis of anisotropy, and r and θ the arbitrary polar axis from which the angle θ is measured, the equations for the generalized Hooke's law given by (2.1) will take the following form in cylindrical coordinates,:

$$\begin{bmatrix} \varepsilon_r \\ \varepsilon_\theta \\ \varepsilon_z \\ \gamma_{\theta z} \\ \gamma_{rz} \\ \gamma_{r\theta} \end{bmatrix} = \begin{bmatrix} a_{11} & a_{12} & a_{13} & a_{14} & a_{15} & a_{16} \\ & a_{22} & a_{23} & a_{24} & a_{25} & a_{26} \\ & & a_{33} & a_{34} & a_{35} & a_{36} \\ & & & a_{44} & a_{45} & a_{46} \\ S & Y & M & & a_{55} & a_{56} \\ & & & & & a_{66} \end{bmatrix} \begin{bmatrix} \sigma_r \\ \sigma_\theta \\ \sigma_z \\ \tau_{\theta z} \\ \tau_{rz} \\ \tau_{r\theta} \end{bmatrix} \tag{2.33}$$

In the case of plane of symmetry normal to the z-axis, the coefficients a_{14}, a_{24}, a_{34}, a_{15}, a_{25}, a_{35}, a_{56}, and a_{46} become zero as in Section 2.2.1. In the case of three planes of symmetry, as discussed in Section 2.2.2, in addition to the above coefficients, a_{16}, a_{26}, a_{36}, and a_{45} also become zero. Thus the Hooke's law for this case will have the form:

$$\begin{bmatrix} \varepsilon_r \\ \varepsilon_\theta \\ \varepsilon_z \\ \gamma_{\theta z} \\ \gamma_{rz} \\ \gamma_{r\theta} \end{bmatrix} = \begin{bmatrix} \frac{1}{E_r} & -\frac{\nu_{\theta r}}{E_\theta} & -\frac{\nu_{rz}}{E_z} & 0 & 0 & 0 \\ & \frac{1}{E_\theta} & -\frac{\nu_{rz}}{E_z} & 0 & 0 & 0 \\ & & \frac{1}{E_z} & 0 & 0 & 0 \\ & & & \frac{1}{G_{\theta z}} & 0 & 0 \\ & & & & \frac{1}{G_{rz}} & 0 \\ S & Y & M & & & \frac{1}{G_{r\theta}} \end{bmatrix} \begin{bmatrix} \sigma_r \\ \sigma_\theta \\ \sigma_z \\ \tau_{\theta z} \\ \tau_{rz} \\ \tau_{r\theta} \end{bmatrix} \qquad (2.34)$$

In eq. (3.27) E_r, E_θ, E_z are the Young's moduli in the radial, tangential and axial directions ; $\nu_{r\theta}$ is the Poisson's coefficient that characterizes the compression in the tangential (θ) direction for tension applied in the radial (r) direction, etc. ; Shear moduli $G_{\theta z}$, G_{rz}, $G_{r\theta}$ characterize the shear moduli surfaces θ - z, r -z, and lastly at θ - z. A special case of three planes of symmetry is when the material exhibits isotropy in a plane normal to an axis (z-axis), as in the case of the transversely isotropic materials mentioned in Section 2.2.3.

2.2 Finite element equilibrium equations

The following brief summary of the basic concepts of the finite element method is based on the book by Bathe [35]. The displacement- based finite element formulation is based on the principle of virtual displacement. This principle states that in the equilibrium state, for small virtual displacements imposed on the body, the total internal virtual work is equal to total external virtual work, as described by the following expression:

$$\int_V \bar{\varepsilon}^T \varepsilon^T \ \tau dV = \int_V \bar{U}^T \ f^B dV + \int_{S_f} \bar{U}^{S_f T} f^{S_f} dS + \sum_i \bar{U}^{iT} R_C^i \tag{2.35}$$

where $\bar{U}$ and $\bar{\varepsilon}$ are the virtual displacements and the corresponding virtual strains (where T denotes the transpose), respectively. The right hand side of eq. (2.35) represents the virtual work done by the externally applied load f^B (per unit volume, where B denotes the body forces), surface traction f^{S_f} over a small area (S_f is the surface subject to the surface traction f), and concentrated loads R_C^i where the superscript i denotes the point of load application. These three loads are expressed in components corresponding to the Cartesian coordinate system as follows:

$$f^B = \begin{bmatrix} f_X^B \\ f_Y^B \\ f_Z^B \end{bmatrix}; \qquad f^{S_f} = \begin{bmatrix} f_X^{S_f} \\ f_Y^{S_f} \\ f_Z^{S_f} \end{bmatrix}; \qquad R_C^i = \begin{bmatrix} R_{CX}^i \\ R_{CY}^i \\ R_{CZ}^i \end{bmatrix} \tag{2.36}$$

Virtual displacements are independent from the actual displacements that a body undergoes due to the applied load, and are not real displacements. Stresses τ are assumed as known quantities and are unique stresses that balance the applied loads. Virtual strains ε^* are calculated by the differentiations :

$$\varepsilon_{xx} = \frac{\partial U}{\partial X}; \qquad \varepsilon_{yy} = \frac{\partial U}{\partial Y}; \qquad \varepsilon_{zz} = \frac{\partial U}{\partial Z} \tag{2.37}$$

$$\gamma_{XY} = \frac{\partial U}{\partial Y} + \frac{\partial V}{\partial X}; \qquad \gamma_{YZ} = \frac{\partial V}{\partial Z} + \frac{\partial W}{\partial Y}; \qquad \gamma_{ZX} = \frac{\partial W}{\partial X} + \frac{\partial U}{\partial Z} \tag{2.38}$$

The virtual displacement field is continuous over the volume, with values from zero at the surfaces where boundary conditions of displacement are imposed. When the principle of virtual displacements is satisfied, all three fundamental requirements of mechanics are fulfilled: Equilibrium, Compatibility (continuous displacement field satisfying the boundary conditions), and the stress-strain law holds because stresses $\boldsymbol{\tau}$ are calculated based on constitutive relationships from strains $\boldsymbol{\varepsilon}$.

Bodies are approximated in Finite Element Analysis as an assemblage of discrete finite elements connected with each other at nodal points. The displacements are assumed to be a function of the nodal displacement, and are measured in a local coordinate system x, y, and z chosen conveniently within each discrete element. Therefore, for a specific m^{th} discrete element, the displacement $u^{(m)}$ is given by:

$$u^{(m)}(x,y,z) = H^{(m)}(x,y,z)\hat{U} \tag{2.39}$$

where $\boldsymbol{H^{(m)}}$ is the displacement interpolation matrix, and $\hat{U}$ is the vector of the three global displacement components U_i, V_i, and W_i for all nodal points, including those at supports. Using eq. (3.32), the element strains can be expressed as:

$$\varepsilon^{(m)}(x,y,z) = B^{(m)}(x,y,z)\hat{U} \tag{2.40}$$

where $\boldsymbol{B^{(m)}}$ is the strain-displacement matrix. The use of eqs. (2.32) and (2.33) together with the principle of virtual displacement will process all element matrices of an assemblage of elements, into governing structure matrices. This process is referred to as the direct stiffness method. The relation between the element stress and strain is given by:

$$\tau^{(m)} = C^{(m)}\varepsilon^{(m)} + \tau^{I(m)} \tag{2.41}$$

where $\boldsymbol{C^{(m)}}$ is the elasticity matrix of element m and $\boldsymbol{\tau^{I(m)}}$ are the given initial element stresses. The governing law for the material specified in $\boldsymbol{C^{(m)}}$ for individual elements can be isotropic or anisotropic (as described in section 2.1) and can vary from element to element. By using eq. (2.32), the equilibrium equation corresponding to the nodal point displacements can be given as a sum of integrations over volume and areas as follows:

$$\sum_m \int_{V^{(m)}} \bar{\varepsilon}^{(m)T} \tau^{(m)} dV^{(m)} = \sum_m \int_{V^{(m)}} \bar{u}^{(m)T} f^{B(m)} dV^{(m)} + \sum_m \int_{s_1^m \ldots, s_q^m} \bar{u}^{(m)T} f^{S(m)} dS^{(m)} + \sum \bar{u}^{iT} R_C^i \tag{2.42}$$

where m=1, 2…,k (k = number of elements), and $S_1^{(m)}.....S_q^{(m)}$ denotes the element surface part of the body surface S. Applying the principle of virtual displacements on expressions (2.39) and (2.40) and substituting into (2.42) gives:

$$\bar{\hat{U}}\left[\sum_m \int_{V^m} B^{(m)T} C^{(m)} B^{(m)} dV^{(m)}\right]\hat{U} = \bar{\hat{U}}^T \left[\begin{array}{l} \left\{\sum_m \int_{V^{(m)}} H^{(m)T} f^{B(m)} dV^{(m)}\right\} + \left\{\sum_m \int_{S_1^m \ldots, S_q^m} H^{S(m)T} f^{S(m)} dS^{(m)}\right\} - \\ -\left\{\sum_m \int_{V^{(m)}} B^{(m)T} \tau^{I(m)} dV^{(m)}\right\} + R_c \end{array}\right] \tag{2.43}$$

where the surface displacement interpolation matrices $H^{S(m)}$ are obtained from the displacement interpolation matrices $\boldsymbol{H^{(m)}}$ by substituting the appropriate surface element, and the concentrated load vector is applied to the nodes of the element assemblage.

The principle of virtual displacement is applied $\boldsymbol{n}$ times using expression (2.43) to obtain the equations for the $\boldsymbol{n}$ unknown nodal point displacements resulting in

$$KU = R \tag{2.44}$$

where : $R=R_B+R_S-R_I+R_C$

and denoting the unknown nodal point displacement $U \equiv \hat{U}$, the resulting stiffness matrix **K** of the element assemblage is,

$$K = \sum_m \int_{V^{(m)}} B^{(m)T} C^{(m)} B^{(m)} dV^{(m)} = \sum_m K^{(m)} \tag{2.45}$$

The effect of element body forces is

$$R_B = \sum_m \int_{V^{(m)}} H^{(m)T} f^{B(m)} dV^{(m)} = \sum_m R_B^{(m)} \tag{2.46}$$

and the effect of element surface forces is

$$R_S = \sum_m \int_{S_1^{(m)} \ldots S_q^{(m)}} H^{S^{(m)T}} f^{S(m)} dS^{(m)} = \sum_m R_S^{(m)} \tag{2.47}$$

while the effect of element initial stresses is,

$$R_I = \sum_m \int_{V^{(m)}} B^{(m)T} \tau^{I(m)} dV^{(m)} = \sum_m R_I^{(m)} \tag{2.48}$$

and R_c are the nodal concentrated loads.

Expression (2.44) represents the static equilibrium of the element assemblage. The applied force may vary in time, in which case the displacement also varies in time and the expression (2.44) becomes the expression of equilibrium for every specific point in time. The summation of the element volume and surface integrals evaluated from expressions (2.45) through (2.48) represent the direct addition of the element stiffness matrices $K^{(m)}$, the body force vectors $R_B^{(m)}$, and R_s and R_I similarly. This process of assemblage is called the direct stiffness method.

In the above evaluations, inertial forces are negligible because the loads are assumed to be applied slowly. If these loads are applied rapidly, then the inertial loads need to be calculated resulting in evaluation of mass and damping matrix for the body, the resulting equilibrium equations are of the form:

$$M\ddot{U}+C\dot{U}+KU=R \tag{2.49}$$

Therefore, for the dynamic case, where the inertial forces need to be evaluated, the matrices K, M, and C and the load vector R must be calculated. Then, the system will be solved for the unknown responses $U,\dot{U},\ddot{U}$ subject to possible initial stresses and displacements.

2.3 Contact Boundary Problem

Boundary value problems involving contact are of great importance in all fields of engineering. Most of the problems involving contact between bodies can be treated by the assumption of small strains; however, due to the nature of the contact problem, all applications are nonlinear. These nonlinearities are as a consequence of the geometric and material discontinuity at the interface instead of the usual continuity property holding in solid mechanics, and involve variational inequalities and constrained minimizations. Contact problems can be combined either with large elastic or inelastic deformations, and can include time-dependent responses. Hence, today's modern contact formulations in computational mechanics have to account for all these effects and involve the use of special algorithms to obtain the solutions.

In the following sections, the contact boundary problem that is briefly introduced can be found described in detail in the book by Wriggers [36].

2.3.1 Contact Problem Definition

In continuum mechanics, contact problems can be included in the general category of constrained minimization problems. If two bodies are in contact at time t, with contact surface Γ_c, then the principle of virtual work can be written as:

$$\Pi^{\gamma} = \int_{B^{\gamma}} W^{\gamma}(C)dV - \int_{B^{\gamma}} \bar{f}^{\gamma} \cdot \varphi^{\gamma} dV - \int_{\Gamma_{\sigma}^{\gamma}} \bar{t}^{\gamma} \cdot \varphi^{\gamma} dA \qquad (2.50)$$

Equation (2.50) represents the total potential energy of the system of interacting bodies, where the contributions of the contact forces are included in the last term of the right-hand side. These contributions are represented by the general term t^{γ} which denotes the surface traction applied on the boundary of B^{γ}. The contributions of body forces $\bar{f}^{\gamma}$ acting on the body B^{γ} are included in the second integral, and $W^{\gamma}(C)$ describes the strain energy function of the body B^{γ}.

Figure 2.2 schematically illustrates the case of deformable-to-rigid contact in two dimensions, where contact areas between the bodies are denoted by Γ_c, the outward normal vector to the surface is denoted by n, the gap between contacting surfaces is denoted by g, and the contact pressure is denoted by p_N.

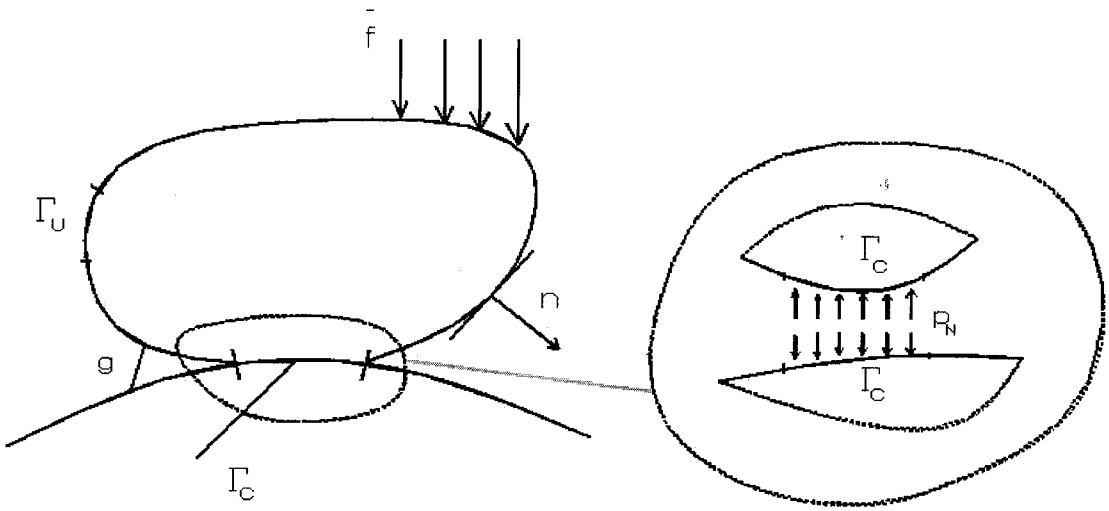

Figure 2.2 Contact of two elastic bodies

The constrained minimization contact problem has the form:

$$\left.\begin{aligned} \Pi(y) &\rightarrow \min \\ b(y) &= 0 \\ g(y) &\leq 0 \end{aligned}\right\} \qquad (2.51)$$

where **y** indicates the unknowns, and the functional **Π(y)** describes the elastic potential, the constraint set **b(y) =0** denotes standard boundary conditions and the set $g(y) \leq 0$ collects the unilateral contact constraints. The constraint $g(y) \leq 0$ can result in a set of simple geometrical non-penetration conditions, or can be associated with a contact constitutive law that defines surface distance with respect to the contact pressure. For the formulation given by equation (2.50), a solution y^* must be found which fulfils all the constraint set equations.

2.3.2 Contact Kinematics

Consider two bodies β^1 and β^2, approaching each other during a finite deformation process and coming into contact on areas Γ_c as shown in figure (2.3).

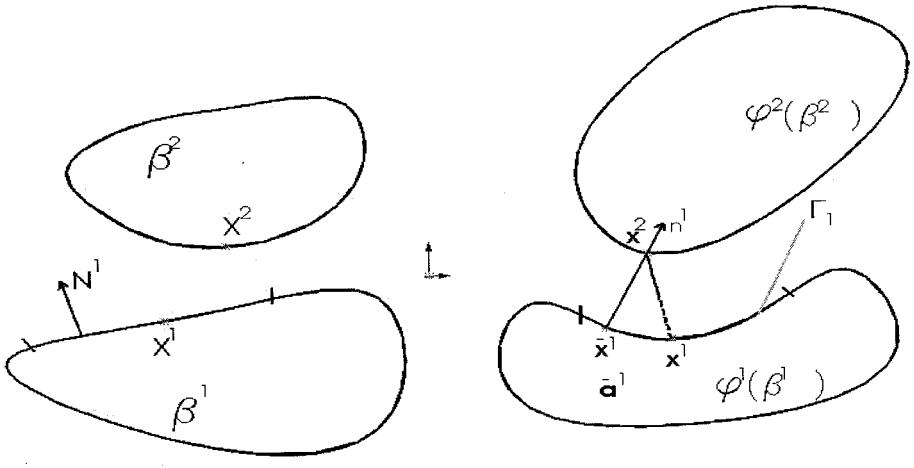

Figure 2.3 Minimum distance determination, for deformed configuration of bodies B^α [37]

Two points X^1 and X^2 in the initial configuration can occupy the same position in the current configuration $\varphi(X^2)=\varphi(X^1)$ within the deformation process. The non-penetration condition is given by :

$$\left(x^2 - x^1\right)\cdot n^1 = 0 \tag{2.52}$$

where x^α denotes the coordinates of the current configuration $\varphi(\beta^\alpha)$ of body β^α : $x^\alpha=X^\alpha+u^\alpha$ where X^α is related to the initial configuration of body β^α and u^α is the displacement field. Every point x^2 on Γ^2 can be related to a point $\bar{x}^1 = x^1\left(\bar{\xi}\right)$ on Γ^1 via the minimum distance problem

$$\hat{d}^1\left(\xi^1,\xi^2\right)=\left\|x^2 - x^1\right\| = \min_{x^1\subseteq\Gamma^1}\left\|x^2 - x^1(\xi)\right\| \tag{2.53}$$

The distance, in eq. (2.53) can be used to define the gap or penetration between the two bodies. $\xi=(\xi^1,\xi^2)$ denotes the parameterization of the boundary Γ^1 via convective coordinates. The outward unit normal vector can be calculated by:

$$\bar{n}^1 = \frac{\left(\bar{a}_1^1 \times \bar{a}_2^1\right)}{\left\|\bar{a}_1^1 \times \bar{a}_2^1\right\|} \tag{2.54}$$

where $\bar{a}_\alpha^1$ is the tangent vector at master point $\hat{x}^1(\xi^1,\xi^2)$. Here the quantities with an over bar represent their evaluation at the minimal distance point(ξ^1,ξ^2). Thus the above expression can be written in the following form:

$$\bar{n}^1 = \frac{x^2 - \hat{x}^1\left(\xi^1,\xi^2\right)}{\left\|x^2 - \hat{x}^1\left(\xi^1,\xi^2\right)\right\|} \tag{2.55}$$

Generally, this definition can be used in relation with the penalty method (see section 2.3), and it has the problem that $\bar{n}^1$ is not defined for $\left\|x^2 - \hat{x}^1(\xi^1,\xi^2)\right\|$=0. Once the point $\bar{x}^1$ is known, either the inequality constraint of the non-penetration condition can be defined as in:

$$g_N = \left(x^2 - \bar{x}^1\right)\cdot \bar{n}^1 \geq 0 \tag{2.56}$$

or the penetrations function as in:

$$\bar{g}_N = \begin{cases} \left(x^2 - \bar{x}^1\right)\cdot \bar{n}^1 \ldots if \ldots \left(x^2 - \bar{x}^1\right)\cdot \bar{n}^1 < 0 \\ 0 \ldots\ldots\ldots\ldots\ldots\ldots otherwise \end{cases} \tag{2.57}$$

The later defines the magnitude of penetration of one body into the other and has to be used in conjunction with the penalty method. In the case of geometrically linear kinematics, the inequality constraint can be written as:

$$\left(u^2 - \bar{u}^1\right) \cdot \bar{n}^1 + g_X \geq 0 \tag{2.58}$$

Where u^α are the displacement of bodies β^α, and the $g_X = \left(X^2 - \bar{X}^1\right) \cdot \bar{n}^1$ represent the initial gap between the bodies. Thus the penetration function, in view of the penalty formulation, is given by the following:

$$\bar{u}_N = \begin{cases} \left(u^2 - \bar{u}^1\right) \cdot \bar{n}^1 + g_X \ldots if \ldots \left(x^2 - \bar{x}^1\right) \cdot \bar{n}^1 + g_X < 0 \\ 0 \ldots\ldots\ldots\ldots\ldots\ldots otherwise \end{cases} \tag{2.59}$$

Functions $\bar{g}_N$ and $\bar{u}_N$, in eqs. (2.57) and (2.59), indicate the penetration of one body into the other. In the case of contact between a rigid surface and a deformable body, and this will also hold, with the conditions that $\bar{u}^1 \equiv 0$, and $\bar{n}^1$ is normal to the surface of the rigid body.

2.3.3 Tangential Contact

There are two distinguishing cases in the tangential direction. The first is the case of a stick state where a point in contact is not allowed to move in the tangential direction. The second case is sliding, where a point in contact is allowed to move in tangential direction.

For the stick state case, the computed values of the convective coordinates $\left(\xi^1, \xi^2\right)$ do not change during the motion, and hence $\dot{\bar{\xi}}^\alpha = 0$. Thus, the stick condition can be formulated as follows:

$$g_T = g_{T\alpha}\,\bar{a}^{\alpha} = 0 \qquad \text{where} \qquad g_{T\alpha} = \left(x^2 - \bar{x}^1\right)\cdot \bar{a}^1_\alpha \tag{2.60}$$

In the above expression, g_T represent the relative displacements in the tangential direction, which for sticking must be zero. Thus, using the fact that the normal gap g_N is equal to zero, and that $g_T = 0$, a more simplified form results:

$$x^2 - \bar{x}^1 = 0 \tag{2.61}$$

In the case of sliding, the tangential slip between bodies is related to the change of point x^2 relative to the projection $\bar{x}^1$, which means that the solution point $\bar{\xi} = \left(\bar{\xi}^1, \bar{\xi}^2\right)$ obtained through eq. (2.53) will move on the master surface (named as contactor surface). During calculations, the path during this movement can be arbitrary and cannot be assumed a priori. The relative tangential velocity along this path is given by:

$$\dot{g}_T = \dot{\bar{\xi}}^{\alpha}\,\bar{a}_{\alpha} \tag{2.62}$$

Tangential stresses can be calculated from constitutive functions where tangential slip $\dot{g}_T$ enters as a local kinematical function. In the above expression, $\dot{\bar{\xi}}^{\alpha}$ represents the relative velocity in convective parameterized coordinates.

2.3.4 Constraint Formulation

The classical way to formulate a contact constraint is based in the idea of treating normal contact as a geometrical constraint. The mathematical condition for non-penetration is stated by the expression $g_N \geq 0$, which excludes penetration as a possible situation into the solution. Contact takes place when $g_N = 0$, and the associated normal component p_N^1 must not be zero and,

$$t^1 = \sigma^1 \bar{n}^1 = p_N^1 \bar{n}^1 + t_T^{1\beta} \bar{a}_\beta^1 \tag{2.63}$$

Stress action on both contact surfaces obeys the principle of action-reaction, thus the stress component action on one surface is equal and in opposite direction to the corresponding stress component action on the other contact surface. For the frictionless case, the tangential stress component $\bar{t}_T^{1\beta}$ becomes zero.

For contact between the surfaces, a combination of functions $g_N = 0$ and $p_N < 0$ hold, and when a gap is present between the surfaces, then the function combination $g_N > 0$ and $p_N = 0$ hold. Summarizing will lead to the statement known as the Kuhn-Tucker-Karush condition for frictionless contact as:

$$g_N \geq 0, \qquad p_N \leq 0, \quad \text{and} \quad g_N p_N = 0 \tag{2.64}$$

At the contact interface, as mentioned previously, the response in the tangential direction can be divided into two different actions. The first corresponds to the stick case where the tangential velocity is zero:

$$\dot{g}_T = 0 \quad \Leftrightarrow \quad g_T = 0 \tag{2.65}$$

Associated with the above constraint is a Lagrange multiplier λ_T which denotes the reaction due to the constraint.

The second situation occurs when the tangential forces overcome a certain limit, and sliding between the contacting surfaces occurs. By assuming that Coulomb's friction law holds on the contact surface with μ friction coefficient, the tangential traction component can be evaluated by:

$$t_T = -\mu \, | \, p_N \, | \, \frac{\dot{g}_T}{\left\| \dot{g}_T \right\|} \qquad \text{if} \qquad \left\| t_T \right\| > \mu |p_N| \tag{2.66}$$

Introducing a non-dimensional variable η given by:

$$\eta = \frac{t_T}{\mu p_N} \tag{2.67}$$

then Coulomb's law of friction states the following:

$$\left.\begin{array}{lll} & |\eta| \le 1 & \\ |\eta| < 1 & implies & \dot{g}_T = 0 \\ |\eta| = 1 & implies & sign\left(\dot{g}_T\right) = sign(\eta) \end{array}\right\} \tag{2.68}$$

Fig. 2.4 illustrates the normal and tangential interface conditions.

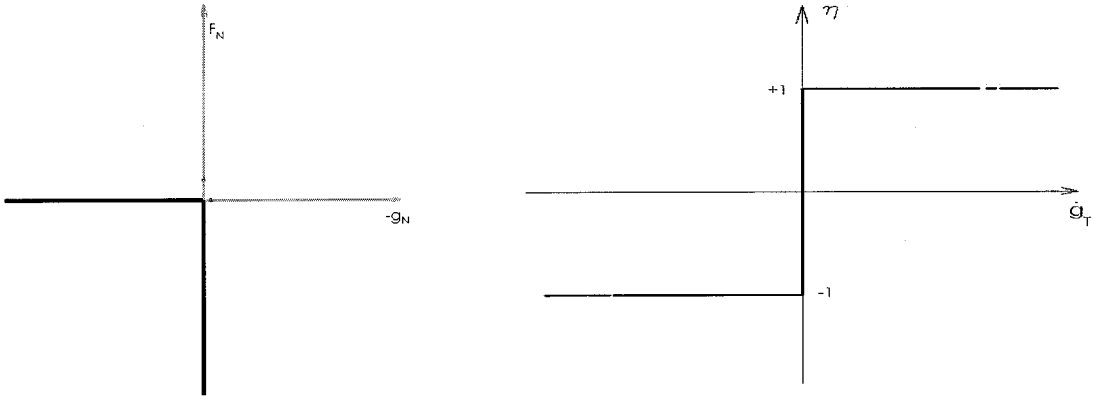

Figure 2.4 Interface conditions in contact analysis. (Left) normal conditions. (Right) tangential conditions

Subsequently, the solution of the contact problem shown in Fig. 2.4 entails the solution of the virtual work (weak form) eq. (2.50) subject to conditions given by eqs. (2.64) and (2.68). In the preceding equations, the static (or pseudo-static) contact conditions are considered. In the dynamic case, the distributed body forces include the inertial force effects and the kinematics interface conditions must be satisfied at all times requiring displacement, velocity and acceleration compatibility between contacting bodies.

2.3.5 Treatment of Contact Constraints and Contact Algorithms

Most standard finite element codes that handle contact problems use either the penalty or the Lagrange multiplier method. For a simplified contact representation, the contact interface can be considered as known. Thus, the variational inequality that the solution of the contact problem has to fulfill is written as:

$$\sum_{\gamma=1}^{2}\left\{\int_{B^\gamma}\tau^\gamma\cdot\nabla\eta^\gamma dV-\int_{B^\gamma}\bar{f}^\gamma\cdot\eta^\gamma dV-\int_{\Gamma_\sigma^\gamma}\bar{t}^\gamma\cdot\eta^\gamma dA\right\}+C_c=0 \tag{2.69}$$

where C_c are contact contributions associated with the active contact set, η^γ are virtual displacements which are zero at the boundary Γ_φ^γ , $\bar{f}^\gamma$, as mentioned before, denotes the body forces, and t^γ denotes the surface on the boundary Γ^γ.

The above equation (2.69) is obtained by the minimization of the total potential energy for the system comprising two bodies in contact:

$$\sum_{\gamma=1}^{2}\left\{\int_{B^\gamma}W^\gamma(C)dV-\int_{B^\gamma}\bar{f}^\gamma\cdot\phi^\gamma dV-\int_{\Gamma_\sigma^\gamma}\bar{t}^\gamma\cdot\phi^\gamma dA\right\}+\Pi_c\Rightarrow MIN \tag{2.70}$$

where W^γ is the strain energy related to body B^γ, and φ^γ denotes the deformation of bodies. The term Π_c includes the contribution of contact constraints in the potential energy expression.

Several different variants for the formulation of Π_c and C_c are available. Such algorithms are: Lagrange multiplier method, the penalty method, the method of direct elimination of the geometrical contact constraints, the NITSCHE method , the perturbed Lagrange, the Augmented Lagrangian, and the barrier method, etc.

In finite element codes, contact algorithms can be divided into two main groups. The first group, called the global algorithms, includes the contact search and the solution of the variational inequalities algorithm types. The second group, called local algorithms,

includes contact detection, and algorithms dealing with the update of constitutive equations and stresses.

In the following subsections the three most common algorithms will be briefly described: the Lagrange multiplier, the Penalty, and the Augmented Lagrangian method. These three algorithms are briefly treated in the contest of contact constraints treatment and lastly in global solution algorithms.

2.3.6 LAGRANGE Multiplier Method

In the potential energy expression, eq. (2.50), the contact contribution according to the Lagrange multiplier method takes the following form:

$$\Pi_c^{LM} = \int_{\Gamma_C} (\lambda_N g_N + \lambda_T g_T) dA \tag{2.71}$$

Therefore, this technique is based on the addition of the multipliers λ_N and λ_T, where g_N and g_T are the normal and tangential gap functions. Variation of Π_c^{LM} leads to the constraint formulation:

$$C_C^{LM} = \int_{\Gamma_C} (\lambda_N \delta g_N + \lambda_T \delta g_T) dA + \int (\delta\lambda_N g_N + \delta\lambda_T g_T) dA \tag{2.72}$$

In the above formula, the first integral represents the virtual work of the Lagrange multipliers along the variation of the gap functions in the normal and tangential directions, while the second integral describes the enforcement of the constraints. The Lagrange multiplier λ_N can be identified as a constant pressure p_N. δg_N and δg_T are the variations of the normal and tangential gap respectively. Lastly, terms $\lambda_T \delta g_T$ and $\delta\lambda_T g_T$ represent the tangential stick. In the case of the stick condition, the relative tangential slip g_T is zero, for which the term λ_T is treated as a reaction. In the case of sliding, a tangential stress vector $\mathbf{t}_T$ is determined from the constitutive law from frictional slip

where instead of writing $\lambda_T \delta g_T$, one would use $t_T \delta g_T$. Therefore the following expression is true:

$$C_C^{slip} = \int_{\Gamma_C} (\lambda_N \delta g_N + t_T \delta g_T) dA + \int_{\Gamma_C} \delta\lambda_N g_N dA \tag{2.73}$$

Implementation of the Lagrange multiplier method as global solution algorithm occurs as follows. Using matrix notation, the total potential energy equation can be written:

$$\Pi^{LM}(u,\lambda) = \Pi(u) + \Lambda^T G^C(u) \tag{2.74}$$

Subject to the constraint *Kuhn-Tucker-Karash* condition formulated as:

$$G^C(u) \geq 0 \qquad \Lambda(u) \leq 0 \qquad G^C(u)\Lambda = 0 \tag{2.75}$$

variation of expression 2.72 yields:

$$\partial\Pi^{LM} = \partial\Pi + \partial\Lambda^T G^C(u) + \partial u^T C^C(u)^T \Lambda = 0 \tag{2.76}$$

From the expression above, the nonlinear equation system for arbitrary variation takes the form:

$$\begin{aligned} G(u) + \; C^c(u)^T \Lambda &= 0 \\ G^c(u) &= 0 \end{aligned} \tag{2.77}$$

For arbitrary du and $\delta\Lambda$, after the linearization of the above system of equations, the following results:

$$\begin{bmatrix} K_T\left(\bar{u}\right) + K_T^c\left(\bar{u},\bar{\Lambda}\right) & C^c\left(\bar{u}\right)^T \\ C^c\left(\bar{u}\right) & 0 \end{bmatrix} \begin{Bmatrix} \Delta u \\ \Delta\Lambda \end{Bmatrix} = -\begin{Bmatrix} G\left(\bar{u}\right) + C^c\left(\bar{u}\right)^T \bar{\Lambda} \\ G^{cL}\left(\bar{u}\right) \end{Bmatrix} \tag{2.78}$$

Thus the Lagrange multiplier method fulfills the contact constraints exactly by introducing additional variables which here are denoted by Λ.

2.3.7 Penalty method

In this formulation, a penalty term due to the constraint conditions (2.59) is added to the Πas in the following expression:

$$\Pi_C^P = \frac{1}{2}\int_{\Gamma_C}\left(\varepsilon_N\left(\bar{g}_N\right)^2 + \varepsilon_T g_T \cdot g_T\right)dA...\varepsilon_N,\varepsilon_T > 0 \tag{2.79}$$

where ε_N and ε_T represent the penalty parameters. Variation of the above expression yields:

$$C_C^P = \int_{\Gamma_C}\left(\varepsilon_N \bar{g}_N \delta \bar{g}_N z + \varepsilon_T g_T \delta g_T\right)dA...\varepsilon_N,\varepsilon_T > 0 \tag{2.80}$$

From the above expression, when $\varepsilon_N \to \infty$ and $\varepsilon_T \to \infty$, the Lagrange multiplier method is obtained. However, large values of these parameters would lead to an ill-conditioned numerical problem.

For the case of slip conditions, where one of the frictional laws has to be applied , in the case of the Coulomb's friction law:

$$C_C^{slip} = \int_{\Gamma_C}\left(\varepsilon_N \bar{g}_N \delta \bar{g}_N + t_T \delta g_T\right)dA....\varepsilon_N,\varepsilon_T > 0 \tag{2.81}$$

In the case where only stick occurs in the contact interface, then there is no need to distinguish between normal and tangential directions. In such a case, an equal number is

selected for penalty parameters for all direction: $\varepsilon=\varepsilon_N=\varepsilon_T$ and using the constraint given by , the penalty term yields the expression for the contact contribution as:

$$C_C^{stick} = \int_{\Gamma_C} \varepsilon \left(x^2 - \bar{x}^{-1} \right) \left(\eta^2 - \bar{\eta}^{-1} \right) dA \tag{2.82}$$

Because a high value of penalty parameter leads to an ill-conditioned problem, the choice of this parameter is restricted for a given problem.

Implementation of the Penalty method as a global solution algorithm is accomplished in the following manner. Using matrix notation, the total potential energy expression can be written:

$$\Pi^P(u) = \Pi(u) + \frac{\varepsilon}{2} G^c(u)^T G^c(u) \rightarrow MIN \tag{2.83}$$

whose variation yields:

$$\partial \Pi^P = \delta \Pi + \varepsilon \partial u^T C^c(u)^T G^c(u) = 0 \tag{2.84}$$

Where the nonlinear equation system, unlike the Lagrange multiplier method, has the form:

$$G(u) + \varepsilon \cdot C^c(u)^T G^c(u) = 0 \tag{2.85}$$

And as in the Lagrange multiplier method, linearization is required for equation[] at the known displacement state, which results in:

$$\left[K_T\left(\bar{u}\right) + \varepsilon \left(K_T^{cP}\left(\bar{u}\right) + C^c\left(\bar{u}\right)^T C^c\left(\bar{u}\right) \right) \right] \Delta u = -\left[G\left(\bar{u}\right) + C^c\left(\bar{u}\right)^T G^c\left(\bar{u}\right) \right] \tag{2.86}$$

2.3.8 Augmented Lagrangian

Another method to regularize the non-differentiable normal contact and friction terms is provided by augmented Lagrange formulation. For normal contact the augmented Lagrange functional is given by:

$$\Pi_N^{AM} = \begin{cases} \int_{\Gamma_C} \left(\lambda_N g_N + \frac{\varepsilon_N}{2} g_N^2 \right) d\Gamma \ldots\ldots\ldots\ldots for \ldots\ldots\ldots \hat{\lambda}_N \leq 0, \\ \int_{\Gamma_C} -\frac{1}{2\varepsilon_N} |\lambda_N|^2 d\Gamma \ldots\ldots\ldots\ldots for \ldots\ldots\ldots \hat{\lambda}_N > 0, \end{cases} \tag{2.87}$$

where $\hat{\lambda}_N = \lambda_N + \varepsilon_N g_N$. This functional holds not only for a closed gap which is expressed by the condition $\hat{\lambda}_N \leq 0$, but also for an open gap condition expressed by $\hat{\lambda}_N > 0$. Variation of the above expression yields:

$$C_N^{AM} = \begin{cases} \int_{\Gamma_C} \left(\hat{\lambda}_N \delta g_N + \delta\lambda_N g_N \right) d\Gamma \ldots. for \ldots. \hat{\lambda}_N \leq 0, \\ \int_{\Gamma_C} -\frac{1}{\varepsilon_N} \lambda_N \delta\lambda_N d\Gamma \ldots. for \ldots. \hat{\lambda}_N > 0, \end{cases} \tag{2.88}$$

Introducing the increment of relative tangential movement as by $\overset{v}{g}_T = \overset{-\alpha}{\xi} a_\alpha^1 dt$ and the augmented Lagrange multiplier $\hat{\lambda}_T = \lambda_T + \varepsilon_T \overset{v}{g}_T$, the functional given by eq. (2.87) can be written in the following form:

$$\Pi_T^{AM} = \begin{cases} \int_{\Gamma_C} \left(\lambda_T \overset{\vee}{g}_T + \frac{\varepsilon_T}{2} \overset{\vee}{g}_T \overset{\vee}{g}_T \right) d\Gamma \ldots . for \ldots . \left\| \hat{\lambda}_T \right\| \le \mu \hat{p}_N , \\ \int_{\Gamma_C} -\frac{1}{2\varepsilon_T} \left[\left\| \lambda_T \right\|^2 - 2\mu \hat{p}_N \left\| \hat{\lambda}_T \right\| + \left(\mu \hat{p}_N \right)^2 \right] d\Gamma \ldots for \ldots . \left\| \hat{\lambda}_T \right\| > \mu \hat{p}_N , \end{cases} \tag{2.89}$$

where μ is the friction coefficient and $\hat{p}_N$ is the augmented normal contact pressure. For the case where there is no contact between the bodies($\hat{\lambda}_N$ >0) the functional takes the form:

$$\Pi_T^{AM} = \int_{\Gamma_C} -\frac{1}{2\varepsilon_T} \left\| \lambda_T \right\|^2 d\Gamma \qquad \forall \hat{\lambda}_T \tag{2.90}$$

The major problem associated with numerical treatment of the penalty method and the contact interface laws is the ill-conditioning which arises where the large values of the penalty parameters ε_N and ε_T are selected, or the stiffness due to constitutive interface laws are combined with the stiffness of the bodies within the finite element formulation. A method to avoid the ill-conditioning associated with penalty method is the augmented Lagrange technique which functions as a two loop algorithm known as the Uszawa algorithm. The multiplier $\hat{\lambda}_N$ is kept constant during iteration of the inner loop, then within the outer loop this multiplier is updated to a new value. For the frictionless contact case, the contact contribution in the weak form can be expressed in the following form:

$$C_N^{UZ} = \int_{\Gamma_C} \left(\bar{\lambda}_N + \varepsilon_N g_N \right) \delta g_N d\Gamma \tag{2.91}$$

Since $\bar{\lambda}_N$ is unknown, an update procedure for the multiplier is constructed within the iteration loop of the form:

$$\bar{\lambda}_{Nnew} = \bar{\lambda}_{Nold} + \varepsilon_N g_{Nnew} \tag{2.92}$$

As mentioned in the case of the treatment of contact constraints, the Augmented Lagrangian method is based in the combination of penalty and Lagrange multiplier method when used as global solution algorithm. A matrix formulation for frictionless contact is given with the following expression:

$$\Pi^{AM}(u)=\Pi(u)+\Lambda^T G^c(u)+\frac{\varepsilon_N}{2}G^c(u)^T G^c(u)-\frac{1}{2\varepsilon_N}\lambda^T\lambda \tag{2.93}$$

In the above expression, Λ includes all contribution of the contact nodes fulfilling the condition $\lambda_{sm+1}=\lambda_{sm}+\varepsilon_N g_{Ns}$, while λ includes the nodes with $\lambda_{sm+1}>0$ ensuring the differentiability of the function. Variation of the above equation with respect to displacement and Lagrange multipliers yields the nonlinear system of equations:

$$\begin{aligned} G(u)+\quad \Lambda^T C^c(u)+\quad \varepsilon_N C^c(u)^T G^c(u) &= 0 \\ G^c(u) &= 0 \\ -\frac{1}{\varepsilon_N}\lambda &= 0 \end{aligned} \tag{2.94}$$

Solving the above nonlinear system of equations by Newton's method would result in equation system at state (u_m, λ_m):

$$\begin{bmatrix} \hat{K}_T+\varepsilon_N C^{cT}C^c & C^{cT} & 0 \\ 0 & 0 & 0 \\ 0 & 0 & -\frac{1}{\varepsilon_N}I \end{bmatrix}_m \begin{Bmatrix} \Delta u \\ \Delta\Lambda \\ \Delta\lambda \end{Bmatrix}_{m+1} = -\begin{Bmatrix} \hat{G} \\ G^c \\ -\frac{1}{\varepsilon_N}\lambda \end{Bmatrix}_m \tag{2.95}$$

Augmented Lagrange techniques are used with Uszawa algorithms, which increases the total number of iterations through the addition of an inner loop for the contact and an outer loop for the update of the Lagrange parameters. For the frictionless contact formulation, a matrix representation of the Uszawa algorithm starts from Lagrange functional with $\bar{\Lambda}$ constant Lagrange multiplier:

$$\Pi^{UA}(u) = \Pi(u) + \bar{\Lambda}^T G^c(u) + \frac{\varepsilon_N}{2} G^c(u)^T G^c(u) \tag{2.96}$$

The variation with respect to displacement is given by the following expression:

$$G^{UA}\left(u, \bar{\Lambda}\right) = G(u) + \bar{\Lambda}^T C^c(u) + \varepsilon_N C^c(u) G^c(u) = 0 \tag{2.97}$$

which is solved using Newton's method, and after linearization, the system of equations at state $\left(u_i, \bar{\Lambda}\right)$ yields:

$$\left[\hat{K}_T\left(u_i, \bar{\Lambda}\right) + \varepsilon_N \left[C^c(u_i)\right]^T C^c(u_i)\right] \Delta u_{i+1} = -\hat{G}^{UA}\left(u_i, \bar{\Lambda}\right) \tag{2.98}$$

CHAPTER 3

CAD MODELING

In this chapter, the CAD modeling of the bone, which includes both the sheep cortical and cancellous portions, the fixation screw, the Calcium Polyphosphate (CPP) implant, and the cartilage layers, will be presented. The transformation of the bone from computed tomography (CT) scans to computer aided design (CAD) surfaces modeling with MIMICS (Materialise HQ, Leuven, Belgium) will be described in Section 3.1. The modeling of the implant, screw and assembly of the components with SolidWorks (SolidWorks Corporation, Concord, MA, USA) will be described in Section 3.2 and the final smoothing of the model with Rhinoceros 3.0 (Mc Neel North America, Seattle WA, USA) is described in Section 3.3. The chapter will briefly describe the issues encountered during the modeling with each of the software packages and the methods used to address these problems.

3.1 CAD modeling of the Bone.

It was ultimately desired to construct a 3D model of the tibial plateau of a sheep, so that a CPP implant which would replace the medial side of the plateau could be designed and constructed. Modeling with **Materialise's Interactive Medical Image Control System (MIMICS)**, represented the initial step in the construction of the bone CAD model. Computed tomography (CT) scanning is a process in which the relative density of scanned tissue is determined by the use of X-rays. Depending on the type of medium at a specific location of the bone, the resulting image at the CT scan for that location may appear white or black. If the medium is dense (such as cortical bone) the outgoing beam intensity is weaker resulting in a bright area. If the medium is less dense, the loss of beam energy is smaller, and thus the outgoing beam is stronger, resulting in a darker area at the corresponding location in the CT scan. The end result of this process is a stack of two-dimensional images of the tissue, representing its cross-section at various locations along its length. The information provided by the stack of two-dimensional CT scans can then be used to reconstruct the three-dimensional shape of bone.

A CT scan of a three year old sheep tibia was obtained as contiguous images such that the voxel size was 128 μm with a slice distance of 175 μm, providing a total model height of 38.15 mm. In the present sheep tibia case, it was necessary to convert the CT scan slices into 3D surface representations of both the cancellous and cortical portions of the bone, since they have different material properties. This was done using the following general steps:

1) Segmentation of cross - sectional slices along the length of the bone (proximal to distal portion of the tibia)
2) Re-slicing along medial/lateral plane, and segmentation of re-sliced CT scans
3) Polyline creation and surface construct from polylines
4) Export of the constructed surfaces in IGS (initial graphics exchange specification) format

3.1.1 Segmentation of cross sectional slices along the length of the bone

The first step in acquisition of the three-dimensional model of the cortical part of the bone was the creation of the mask, a collection of pixels on which all editing and calculations are performed. The mask was created by the process of 'segmentation' in which a desired group of pixels of i^{th} intensity falling within a set of lower and higher threshold values is assigned to the mask. For the cortical bone, the lower and upper pixel intensity values were determined to be 1340 and 2590 respectively. With this action, the highlighted region of interest (cortical part of tibia), was established simultaneously for all slices. Based upon the information in 136 slices, the three-dimensional model of the lower portion of the tibia was constructed. The overall height if this portion was 23.8 mm. Due to MIMICS software characteristics, where it is not possible to calculate polylines on the axial view with multiple peaks, re-slicing of the initial CT scans was necessary. The difference between the initial setup and re-sliced setup is given in Table

3.1. Three sectional views in the initial and re-sliced model were used, where the views are determined as perpendicular to the planes created by the actual directions of tibia.

Table 3.1 Views in lower portion and re-sliced models in MIMICS

	Directional Views in MIMICS		
	Axial	Coronal	Sagital
Lower Portion of Tibia	*Plane created by directions Medial-Lateral and Ventral-Dorsal*	*Plane Created by directions Axial and Medial-Lateral*	*Plane created by directions Axial and Ventral-Dorsal*
Re-sliced	*Plane created by directions Axial and Ventral-Dorsal*	*Plane Created by directions Medial-Lateral and Ventral-Dorsal*	*Plane created by directions Axial and Medial-Lateral*

Figures 3.1-3.3 show the Axial, Coronal, and Sagittal view for the initial model where only the active mask is displayed and the rest of the bone is displayed as black.

Figure 3.1 Mimics axial view of a typical slice after threshold process applied

Figure 3.2 Mimics coronal view of a typical slice after threshold process applied

Figure 3.3 Mimics sagittal view of a typical slice after threshold process applied

Manual erasing of some portions of the individual slices was required to obtain the cortical bone alone, because some of the images did not threshold properly. Erasing of the undesired pixels was performed separately on individual slices. Thus, after the erasing process, the masks were constructed on the slices corresponding to the lower portion of the tibia shown as in Figures 3.4 -Figure 3.6.

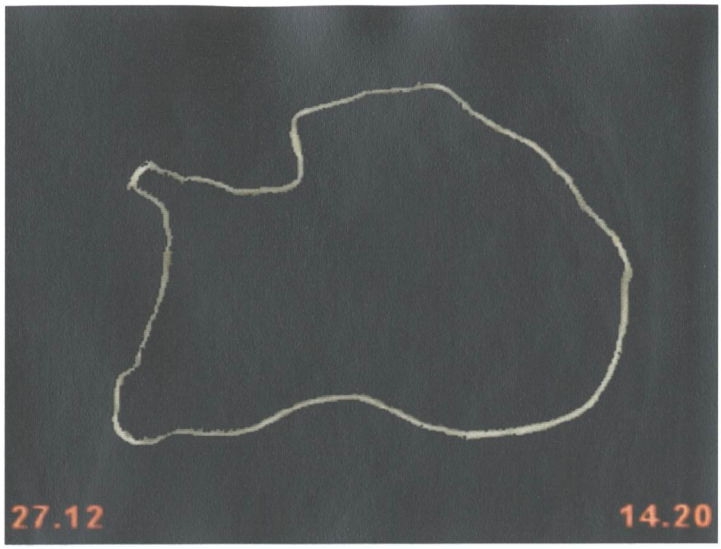

Figure 3.4 Axial view of initial model. Lower portion of tibia

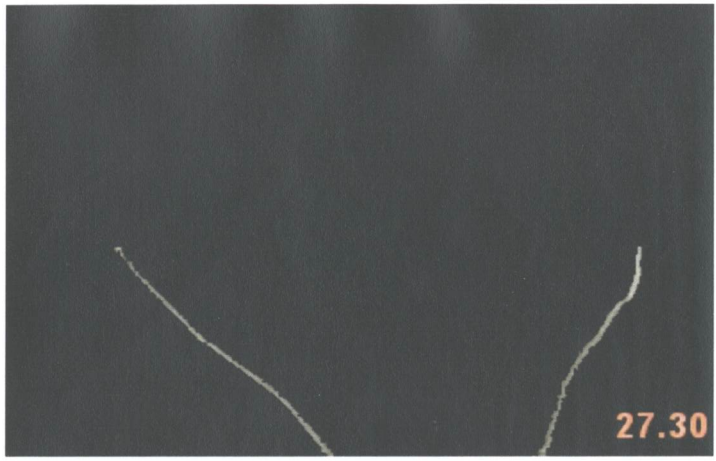

Figure 3.5 Coronal view of initial model. Lower portion of tibia

Figure 3.6 Sagittal view of initial model. Lower portion of tibia

3.1.2 Re-slicing along medial/lateral plane, and segmentation of re-sliced CT scans

In the re-sliced model, the segmentation procedure threshold process was similar to that of the lower portion of the tibia, with the difference only on the sectional view positions. Re-slicing of the images in the perpendicular plane was accomplished by drawing a line with direction from the lateral to the medial side of the tibia. Due to this process, there was a shift of the views in MIMICS; a shift of the sagittal view to the axial view occurred from the initial setup to the re-sliced setup. The axial view in the re-sliced model is given in Figure 3.7, followed by the Coronal and Sagittal views in Figure 3.8 and Figure 3.9, respectively.

In order to have a better capture of the tibial plateau (i.e., the top of the tibia), which was the region of interest for implant design, in the axial view; closure by a semicircle was applied to each individual slice enabling the generation of inner and outer polylines separately. . This shape closure was selected based on preference of having the polyline calculation based on the inner and outer edges of the plateau separately instead of having only one for both simultaneously. The latter would have had a large effect on the quality of the surface construction over these polylines because it would have introduced a large mismatch with the surfaces obtained in the initial model (lower portion of the tibia). This closure is shown in Figure 3.7, in the upper portion of the picture.

Figure 3.7 Axial view of the tibia plateau in the re-sliced model.

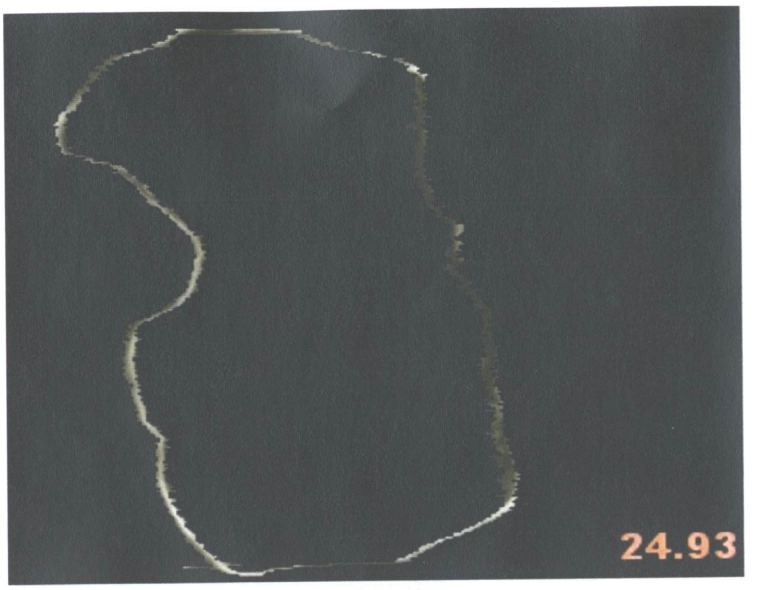

Figure 3.8 Coronal view of the tibia plateau in the re-sliced model.

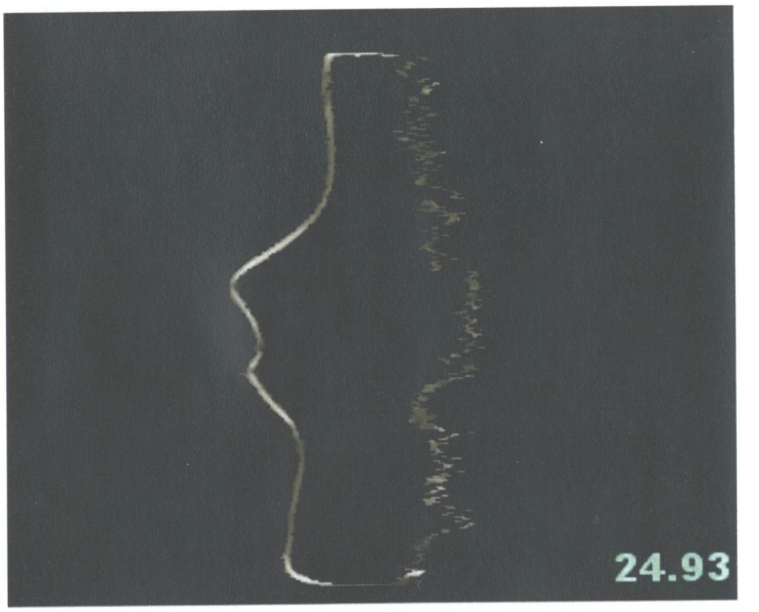

Figure 3.9 Sagittal view of the tibia plateau in the re-sliced model

The quality of the surfaces in the re-sliced model was highly dependent on the closure method employed. Avoiding sharp corners, and with a semicircular shape of an average width of three pixels (0.54 mm), caused the majority of the control points of the surface to fit onto the polylines. These surfaces represent the upper and inner surfaces of the tibial plateau.

3.1.3 Polyline creation and construction of surfaces

For both models, i.e., the lower portion of the tibia and the tibial plateau, the polyline construction was based on two MIMICS functions: 'Polyline calculation' and 'Polyline growing'. Polyline calculation is a function that calculates the best fit of, and constructs, polylines along the boundaries of the mask. These polylines are built based on the axial view of the layout. A major obstacle at this stage was the fact that some of the fit polylines intersected each other. By trial and error, the encountered polyline intersections were avoided by modifying the zones in which they occurred. This modification consisted of widening the strips of pixels representing the cortical width at a particular location, for approximately two to three slices before and after the slice where the intersections occurred. This problem was mostly encountered on the re-sliced model.

'Polyline growing' is a function that enables the creation of a set of polylines connecting the different cross-sectional slices, based on the previously calculated cross-sectional polylines. For each of the MIMICS models, two independent sets were created using these functions: one set for the inner and the other of the outer group of polylines. Based on these sets of polylines, outer and inner freeform surfaces were constructed, whose shape and characteristics depended on two fitting parameters, u and v. The u-parameter ran perpendicular to the image plane, while the v-parameter ran within the cross-sectional image plane. For each of these parameters, the order, number of control points, and the choice of either open or closed shape had to be selected. The order of polynomials used could be chosen from one to five. The number of control points available depended on the parameter: e.g., for the u-parameter with a 4^{th} order, the maximum number of the control points was 132, and for the 4^{th} order v-parameter, the maximum number of control points was 26.

In the present work, an 'Open' surface was selected for the u-parameter and a 'Closed' surface for the v-parameter. The best fit of the freeform surface upon the selected set of polylines was based on a combination of the number of control points and order of polynomials used for both parameters. As the number of control points increased, it increased the accuracy to which the surfaces fit to the polylines; however, this increase was limited by the fact that a choice of too many control points caused the

fitted polynomials to have the tendency to form a wave which no longer actually fit the surface. Therefore, many trials were conducted by varying the u and v parameters until the best overall fit of the surface to the polylines was achieved. This resulting combination of both models is shown in Table 3.2.

Table 3.2 Freeform surface's parameters

		U- Parameter		V-Parameter	
Model	*Surfaces*	*Order*	*Control Points*	*Order*	*Control Points*
Lower Portion of Tibia	*Outer*	*4*	*93*	*4*	*14*
	Inner	*4*	*105*	*4*	*21*
Tibia Plateau	*Outer*	*4*	*56*	*4*	*18*
	Inner	*4*	*58*	*4*	*24*

As seen in Table 3.2, the number of control points for the outer and inner surfaces within each model was different. These differences are the results of the effort to avoid surface intersection, especially on the lower part of the tibia. At the tibial plateau model intersections were allowed only on the semicircular closure, where no effect on the shape tibia plateau resulted.

The end result of the segmentation and polyline fitting was a set of surfaces representing the outer and inner (where the cortical met the cancellous) boundaries of the cortical bone IGS (Initial Graphics Exchange Specifications) format.

3.1.4 Conversion of cortical bone surface to solid model using SolidWorks

The creation of the 3D solid representation of the cortical bone from the surfaces obtained during modeling with MIMICS was accomplished using SolidWorks software. Surfaces obtained from MIMICS were imported into SolidWorks in IGS format, and the first objective was the construction of the solid cortical bone from these surfaces. The procedure was different for the lower portion of tibia model than the tibia plateau. For the lower portion, the solid was obtained by constructing bounding surfaces with borders at the edges of the surfaces imported from MIMICS. The solid obtained in this manner very accurately described the actual cortical bone boundary for the lower portion of tibia. The only simplification made during modeling was the attachment location of the patellar

tendon (located at the ventral side of the tibia). The cavity housing the ligament attachment was eliminated due to complications encountered during freeform surface construction with MIMICS as shown in Figure 3.10.

Another issue identified with the solid was the waviness of the inner and outer surfaces of the solid, as shown in Figure 3.10 which would likely pose problems during finite element meshing. This problematic feature was eliminated using Rhinoceros 3.0 software as explained in Section 3.1.5.

To obtain the solid form of the tibial plateau from the individual surfaces constructed in MIMICS, the solid models were first created from the inner and outer surfaces. The final solid model representing the cortical bone was obtained by subtracting the solid obtained from the inner surface from the solid model obtained from outer surface.

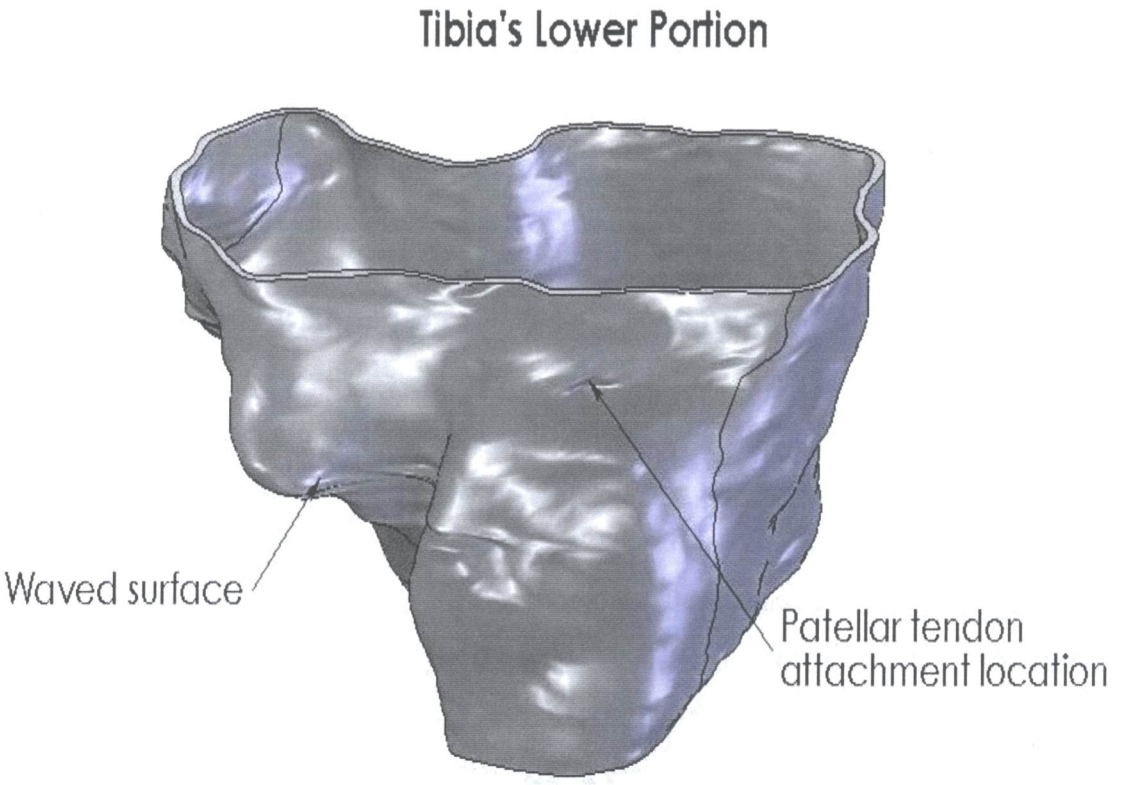

Figure 3.10 Lower portion of tibia in solid form. SolidWorks model

The resulting solid, which includes the true shape of the tibia plateau in addition to the shape obtained from the closure, was cut using the function 'Cut with a plane' available in SolidWorks at the proper height. The sectional view of the tibia plateau is shown in Fig. 3.11.

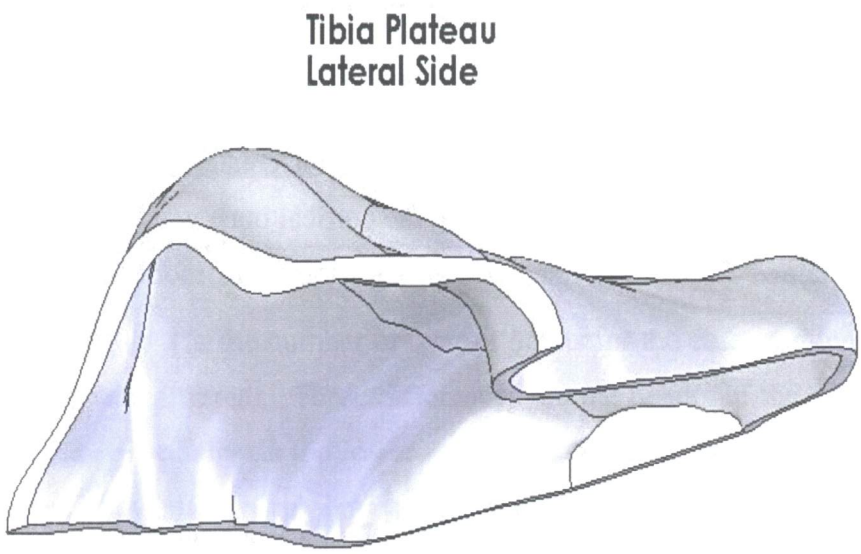

Figure 3.11 Tibia plateau sectional view

3.1.5 Smoothing of problematic areas in cortical bone with Rhinoceros

The solids representing the lower portion and the tibia plateau, were then joined together to create the representation of the total cortical bone (plateau and lower portion). The constructed cortical bone, despite the best efforts to minimize the mismatch between plateau and lower portion, possessed two zones in which there was still some mismatch (highlighted in red in Figure 3.12). These zones were generated by split lines and existed in both the inner surfaces (not shown) as well as the outer surface. The purpose of the bottom strips was to avoid the wavy surfaces (inner and outer) present at the mid-height of the model (areas between height of 8 mm and 1 mm). The reason for creating the upper strip was to provide a natural and smooth transition between the two solid cortical elements.

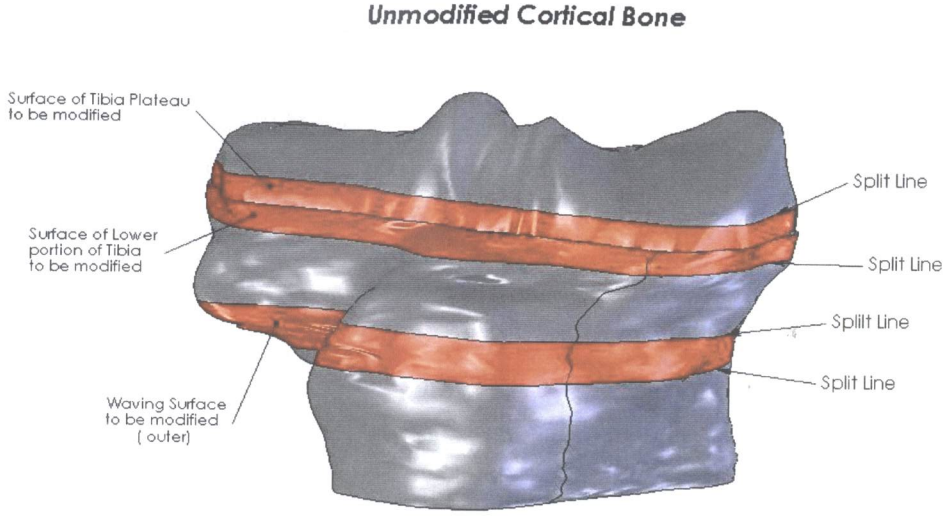

Figure 3.12 Unmodified cortical bones in SolidWorks.

Rhinoceros 3.0 provided the necessary capabilities for extensive surface manipulation Therefore flaws encountered during modeling with SolidWorks were eliminated by the use of this software. Rhinoceros 3.0 was used for several purposes which include: smooth transition between lower portion of cortical bone and tibia plateau, elimination of wavy surfaces, modeling of cartilage layers which included the repair of surfaces, and lastly for each implant it was used to generate the front face of the keel (see Section 3.2).

The model of the cortical bone, as shown in Fig 3.12, was imported, in IGS format, into Rhinoceros 3.0. The edges of the surfaces not needing to be modified (colored red) were divided into several segments through key points. At the convenient points aligned on one axis, new polylines were constructed. To keep the curvature of these polylines such that the surface that was being generated would be as close as possible to that of the surfaces being replaced, midpoints were used on the surfaces before they were deleted.

As an example, in Fig 3.13, the surfaces colored in red are the surfaces that will remain unchanged, the two new surfaces to be created are colored in cyan, and the faulty surface being replaced has already been deleted. Polylines were constructed from points

(1) to point (3) and from point (2) to point (4) through all corresponding points which lie on the horizontal axis between these points. Using these polylines as profile lines and using the edges of opposing surfaces (edges 3 and 4), new surfaces were constructed using the Rhinoceros functions *'sweep 2 rail'* or *'surface from edges'*. The same procedure was followed in replacing all transition surfaces and surfaces containing wavy areas. A similar procedure was used to repair the inner surfaces of the cortical bone and for the construction of the cartilage surfaces based on surfaces imported from SolidWorks.

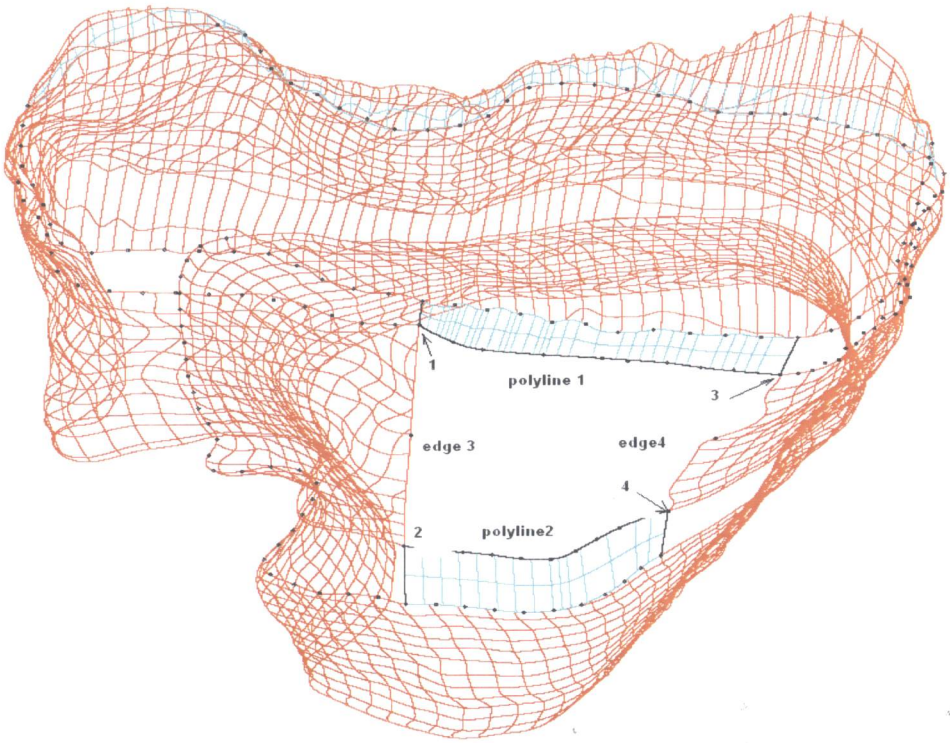

Figure 3.13 Cortical bone in Rhinoceros 3.0. Surface representation through isocurves

The end result of the modified cortical bone model is shown in Fig. 3.14, where the problematic areas are eliminated. This solid model was ultimately used to derive other portions of the model such as the cancellous bone and the top portion of the implant.

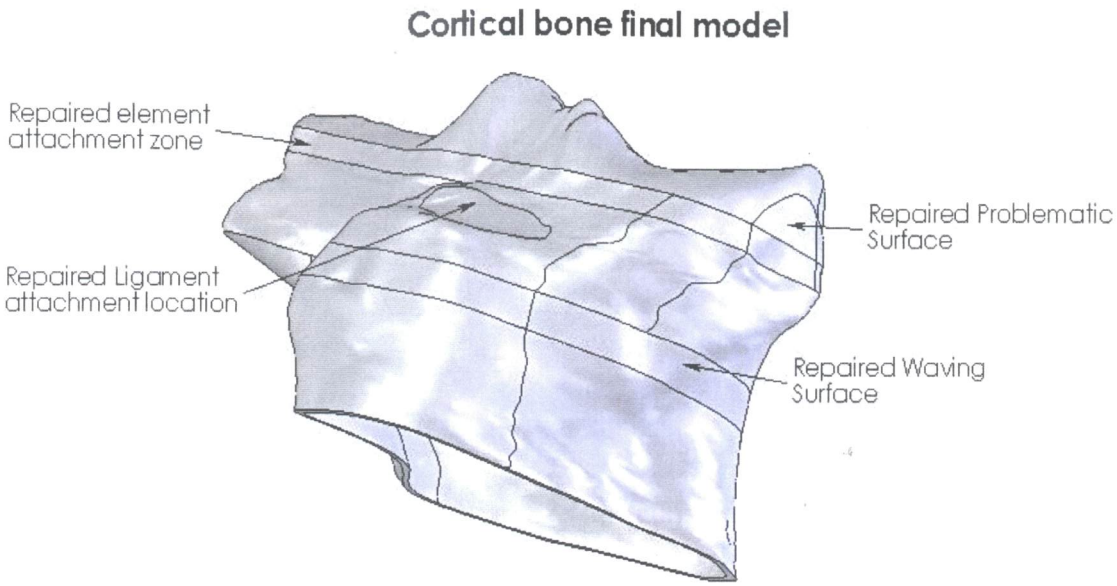

Figure 3.14 Final model of cortical bone

3.1.6 Generation of cancellous bone

The end result of the modified cortical bone shown in Fig. 3.14 was also used to obtain solids representing the cancellous bone and the (inner layer of spongy bone) was created by simply deleting all the outer surfaces, so that the resulting solid was based on the inner surfaces of the cortical boundary. To close the cancellous solid at the distal end, a planar area having boundary edges at these inner surfaces was used. During this process, the coordinate system created for the cortical bone was preserved for the cancellous bone, to make it easier to import into the finite element software. The resulting cancellous bone solid representation is shown in Fig. 3.15.

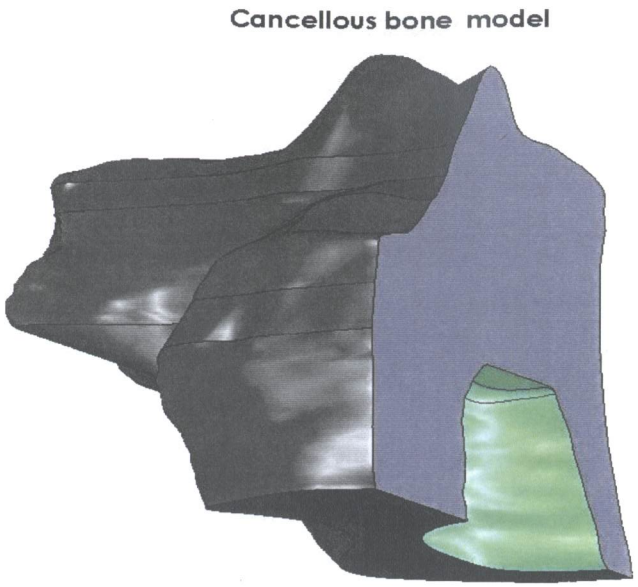

Figure 3.15 Sectional view of cancellous bone solid model.

3.2 Generation of solid model representing various prototype implants

The implant model was comprised of two parts: the body which was derived from the outer surfaces of the cortical bone shown in Fig. 3.13, and the keel which was constructed based on simple geometric shapes. The implant body, as shown in Fig. 3.16, was constructed from the outer surfaces of the cortical bone, ensuring the exact match with the replaced zone on the medial side.

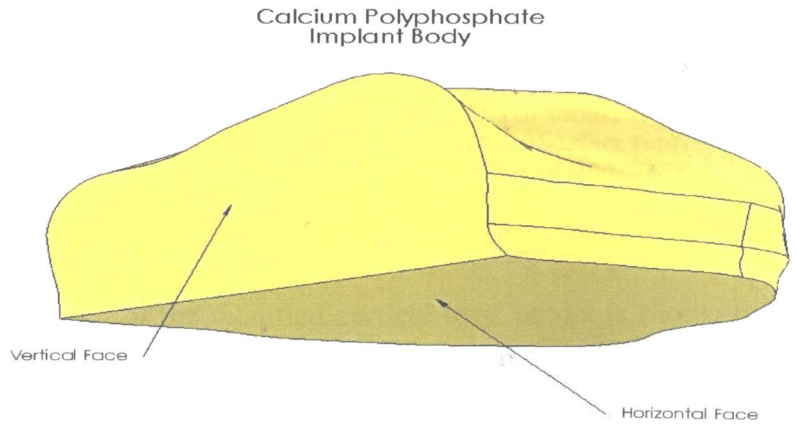

Figure 3.16 Calcium polyphosphate implant body

Two Calcium Polyphosphate (CPP) implant body lengths (i.e., the maximum distance from vertical face to the furthest point on the medial side) were analyzed: 22.65 mm and 16.9 mm. These lengths were derived by creating cutting planes parallel to the *'top plane'* (plane perpendicular to the medial-lateral direction), which was identical for all parts, with distances 27.36 mm and 33.11 mm respectively (measured from top plane which is parallel to the ventral-proximal plane) Initially the height of the implant was selected to be 9.5 mm (maximum height) which was derived by cutting with the *'front plane'* (plane perpendicular to the distal-proximal direction). Later, from the results of the finite element analysis, this height was increased to 10.75 mm (Section 5.1). The maximum height was the distance from the horizontal face to the highest point on the CPP implant upper surface.

To ensure that the implant could be easily slid into position after a surgical removal of the tibial plateau, and would remain stable while load bearing, a keel structure was implemented on the bottom (distal) surface of the implant (Fig. 3.17). Two basic shapes of the cross-section of the keel were analyzed: trapezoidal and semicircular. The final shape of the model was established by considering the method of implementation during surgical operation. Therefore, surgeon preference was strongly taken into consideration. The different geometric parameters varied to determine the final shape of the CPP implant are shown in Figs. 3.17 , 3.18, and 3.19.

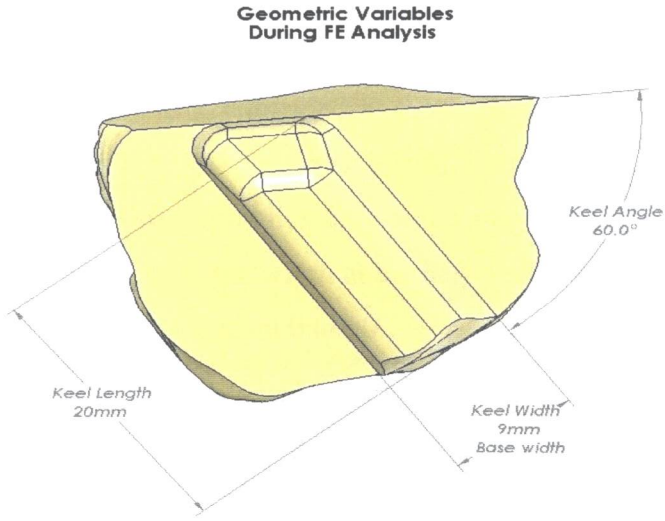

Figure 3.17 Variables used during FE analysis trapezoidal keel. 60^0 angle.

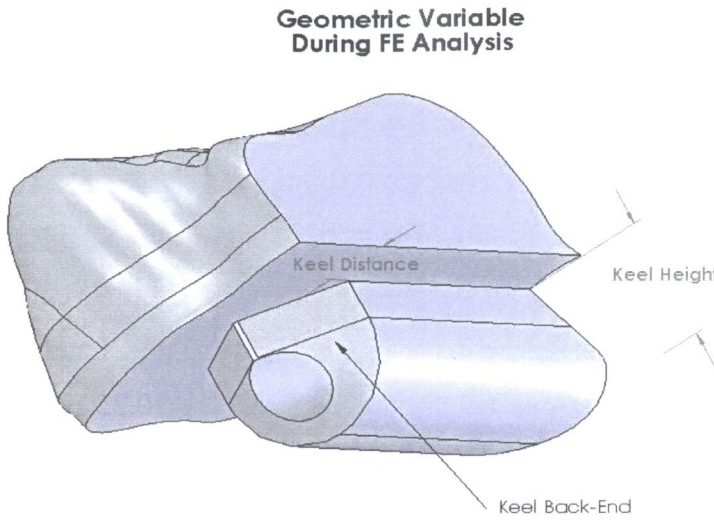

Figure 3.18 Variables used during FE analysis semicircular keel. 3mm keel distance back face semi-conical type

During the FE analysis (Section 5.1), it was quickly discovered that the implant performance was heavily dependent on the position where the screw exited the keel. Therefore, preferring this exit to be at the back face, the length of the keel was adjusted accordingly. Table 3.3 summarizes the various dimensions of the CPP implant models that were constructed and used in the FE analysis.

Table 3.3 Various CPP implant type models

Implant Height (mm)	Implant Length (mm)	Variables	Geometrical Keel Shapes			
			Trapezoidal Keel Cross-section	Semicircular Keel Cross-Section		
				Plane at 45^0 back face	Conical Back-end	Adjusted Back-end
9.25	22.65	Keel Distance (mm)	4, 5	-	-	-
		Keel Angle (degree)	0	-	-	-
		Screw Angle (degree)	12, 15, 20	-	-	-
10.75	22.65	Keel Distance (mm)	4, 5, 6, 7, 8	4, 5, 6	-	-
		Keel Angle (degree)	0 through 90	0	-	-
		Screw Angle (degree)	0, 5, 12, 15, 20	12, 15, 20	-	-
	16.9	Keel Distance (mm))	-	-	0, 1, 2, 3	0, 1,2,3
		Keel Angle (degree)	-	-	0	0
		Screw Angle (degree)	-	-	12,15,20	12,15,20

Implant models were derived as a combination of several variables: e.g., the height, length and keel angle were kept unchanged the implant behavior was analyzed as function of screw angle insertion. Depending on this angle, the length of the keel was adjusted to ensure that the screw exit coincided at the back surface. The for the screw insertion angles between 10 and 20^0 the keel length varied from 13.5 to 21 mm. Semicircular cross section keels having radius 6, 5, and 4 mm were investigated. For the trapezoidal cross-sectional shape keel, the width at the base varied between 8 and 12 mm, with the angle of the trapezoid varying from 0 to 90^o.

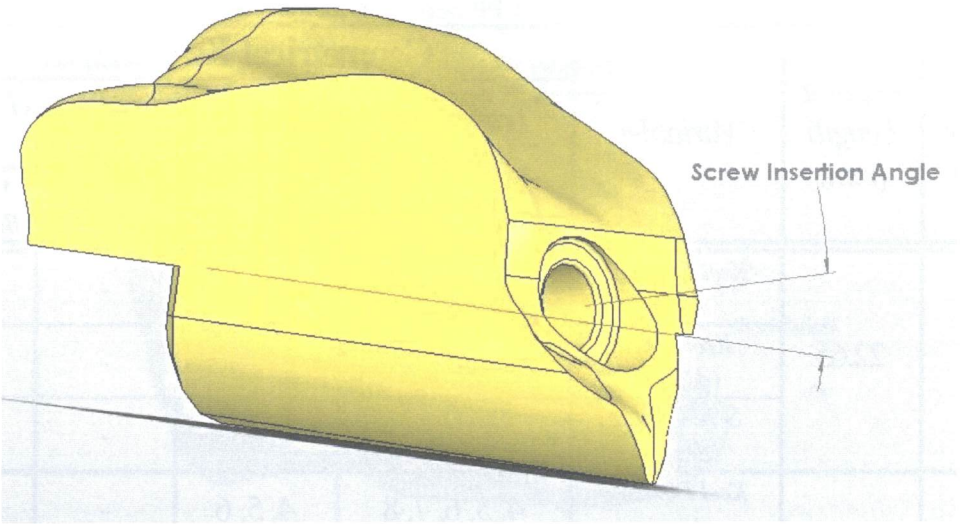

Figure 3.19 Screw angle insertions.

After presenting the candidate keel designs to the members of the surgical team working on the project, it was decided that only the keel with a semicircular cross-sectional shape with varying back end shape would be investigated in detail. It was felt that it was simpler to create the keel's imprint on the cancellous bone with a semicircular cross section, because only a simple vertical movement of the drill bit would provide the groove. However, two different types of back end design were investigated. The first was with a conical back end, exactly mirroring the shape left by the drill bit (Fig. 3.20) and the second model was with a slight modification of the conical back end where the tip of the cone was modified for reason explained in Section 5.2 (Fig. 3.21)

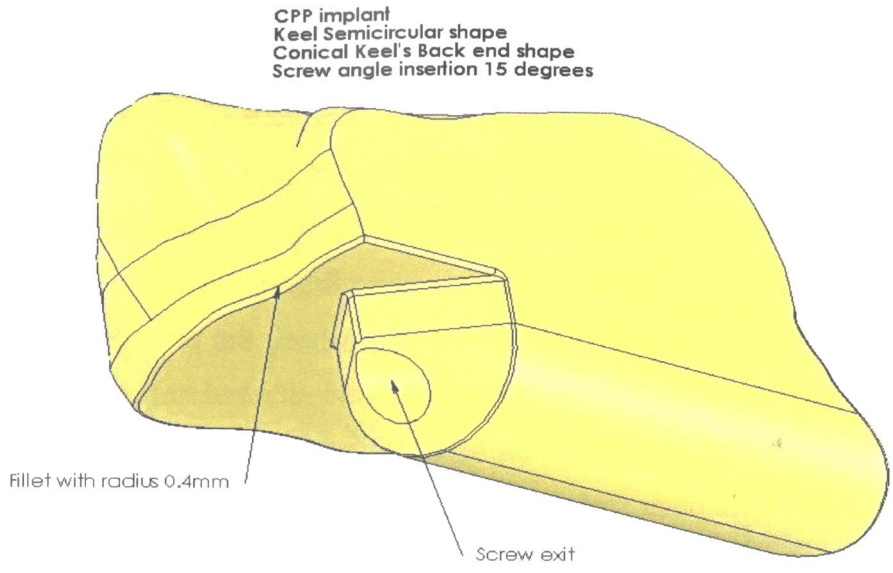

Figure 3.20 Implant with semicircular keel shape of radius 4mm

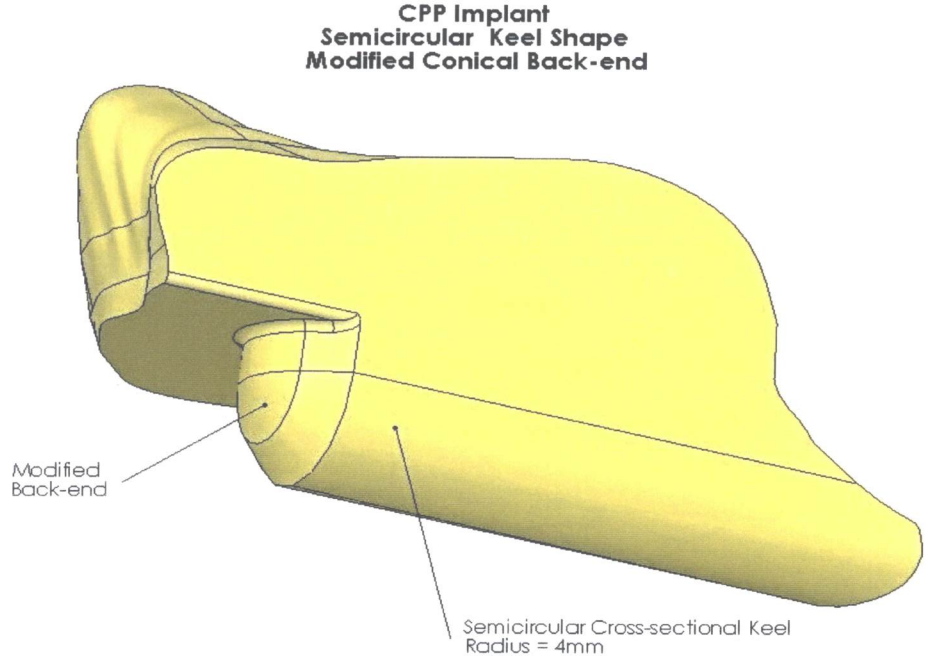

Figure 3.21 Implant with semicircular keel shape of radius 4 mm Modified conical back end

The height of the keel was maintained constant at 6 mm, and to achieve this height for the semicircular keel cross-sectional shape, a prismatic solid was added. For

example, for a 3 mm radius of cross section, a prism was added at the base with a height of 3 mm.

In all cases, the volume of the bone being replaced by the implant was extracted from the cortical and cancellous bone by the use of the 'cavity function' in SolidWorks, where the volume to be subtracted from the cortical and cancellous bone solids (shown in Fig. 3.14 and 3.15) was the volume of the implant itself.

For obtaining the front face of the implant's keel, the procedure was different. The body of the implant with the structure of the keel attached to the cortical bone was imported into Rhinoceros 3.0. The front face of the keel was obtained by trimming the corresponding area from outer surface of cortical bone, and using the obtained surface to trim the structure of the keel (shown in Fig. 3.22). In this way, there was exact match between keel front face shape and cortical bone in the bone assembly.

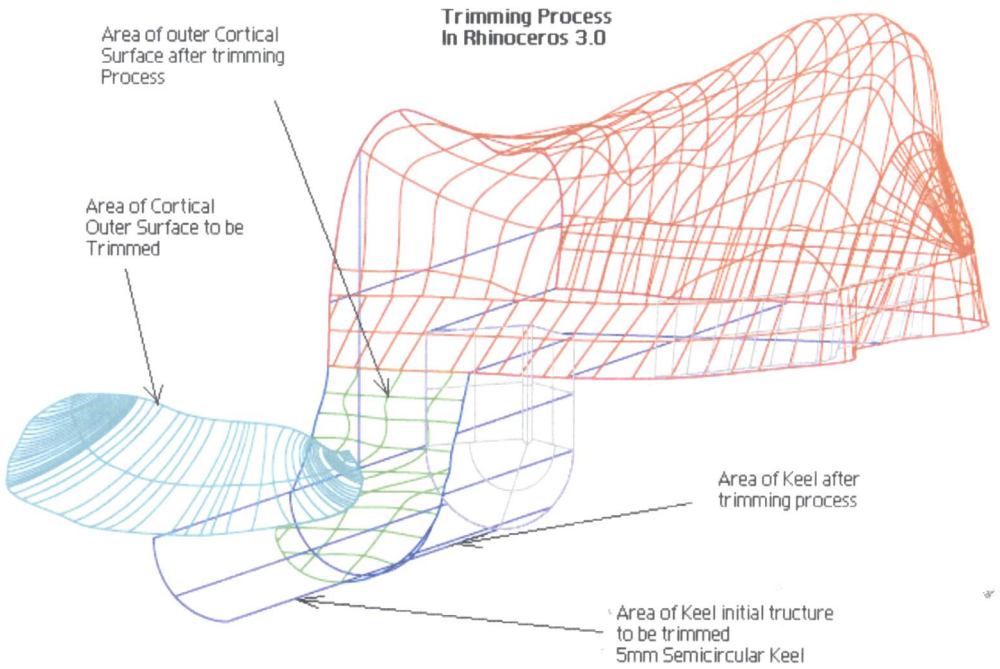

Figure 3.22 Rhinoceros 3.0 trimming stage. Cyan-outer cortical surface to be trimmed. Blue- part of keel structure to be trimmed or trimmed. Green- part of outer cortical surface trimmed

Prior to the export into Ansys Workbench, because the applied loading was to be distributed as a pressure over the surface of the CPP implant (Section 4.2), multi surfaces were generated by splitting the upper surface into 80 pressure surfaces.

These pressure surfaces (Fig. 3.23) were identical for all types of implants tested, allowing for identical loading conditions to be compared across all designs. The pressure surfaces were created in the following manner: From the *'right plane'* (perpendicular to the medial-lateral direction) of the coordinate system, a series of equally spaced (2.15 mm apart) parallel planes was generated with an initial distance from the right plane of 18.5 mm. From the vertical face, a series of parallel planes was constructed with distance of 1.28 mm. Then over the *'front plane'* (plane perpendicular to the axial direction) a series of lines was constructed over the planes generated. These lines were selected to be the split lines, generating the pressure surfaces over the upper surfaces of the implant.

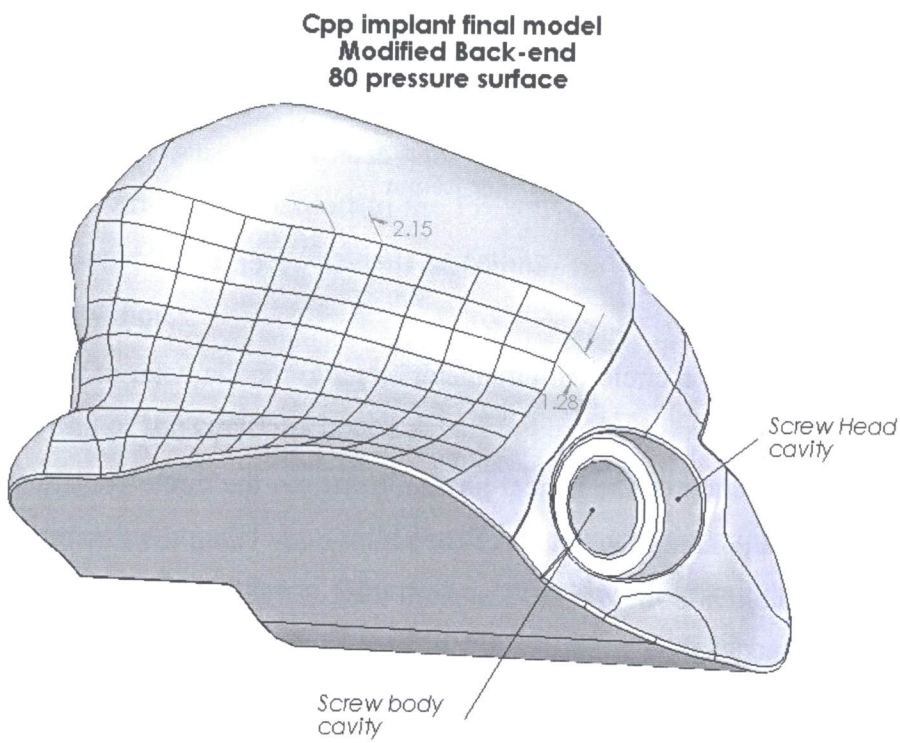

Figure 3.23 Implant with 80 pressure surfaces.

Attachment of the implant to the bone was achieved through the use of a titanium screw, which was also was modeled using CAD techniques. Initially, a cancellous screw

was modeled (Fig. 3.24) complete with threads. Initially a cylinder was constructed with diameter equal to that of the major diameter of the real cancellous screw (3.5 mm).

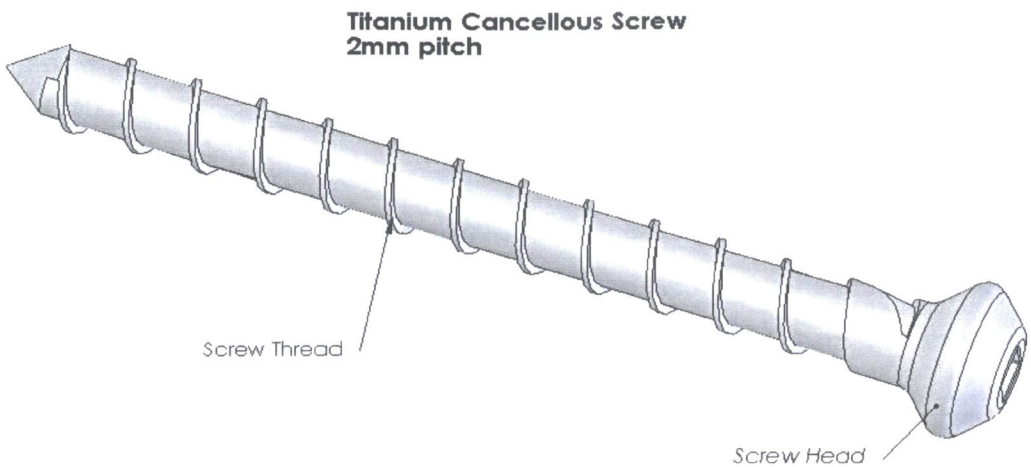

Figure 3.24 Cancellous screw. Pitch 2mm. Major diameter 3.5 mm. Minor diameter 2.6mm

and the chronological steps in creation of the threads were:

1) Drawing of a circle with diameter equal to the diameter of the major diameter of the screw.
2) Construction of the helical profile, based on the circle constructed during the first step, along the length of the screw body using the function *'Helix/Spiral'* available in SolidWorks. The pitch used at this stage was the same as the pitch of the cancellous screw.
3) Drawing of a rectangular profile, which was used to create the cavity following the helical profile constructed during the second step
4) Creation of the cavity, resulting in thread creation, using the function 'Cut-Sweep' available in SolidWorks.

The presence of threads on the screw and their mirrored grove in the cortical and cancellous bone would require a very large number of elements in the FE analysis. Due to restrictions on the number of elements with the license of the FE software, the use of a

fully modeled cancellous screw was abandoned in favor of a more simplified cylindrically shaped screw (Fig. 3.25).

Figure 3.25 Simplified cylindrical body screw. 3mm diameter

The implications of this simplification will be described in Chapter 4. For every assembly analyzed, prior to the export to the FE software, the volume occupied by the screw was subtracted from the cortical, cancellous and implant solids, leaving the properly sized screw holes.

3.3 CAD modeling of the cartilage layers

The last elements modeled in SolidWorks were the cartilage layers on the medial and lateral sides of the tibial plateau. This was achieved by offsetting the upper surfaces (plateau) of the cortical solid model given in Fig. 3.13, by a distance of 0.4 mm (the thickness of the modeled cartilage layer), and erasing every other surface present in the cortical model. The cartilage layer height at sheep varies from 0.4-0.5 mm. This formed a solid representation of the cartilage layer that would be placed on the top of the tibial plateau. The solid derived in this manner inherited many flaws, such as gaps and defective surfaces. Therefore all surfaces, offset and original were exported in IGS format into Rhinoceros 3.0 in order to reconstruct the defective surfaces and close the gaps.

From the Rhinoceros software, the modified cartilage model was imported back into SolidWorks in IGS format as a collection of surfaces, where the transformation into

a solid representing the model of the cartilage layer occurred. The cartilage solid model was cut into two parts: the lateral cartilage part which represented the native cartilage and the medial part which represented the implanted cartilage layer. Cartilage layers obtained in this manner had identical coordinate systems with all other element of the bone assembly and the contact surfaces matched exactly with cortical bone and implant.

When cartilage layer modeling was included in the analysis, pressure surfaces were also generated in the upper surface of the medial implanted cartilage instead of just the upper surface of the CPP implant. The process of generating these pressure surfaces, shown in Fig. 3.27, was identical to the process used for the pressure surfaces on the CPP implant solid model (Section 3.2).

3.4 Construction of bone assemblies with and without cartilage layer

Cartilage layers were introduced only in the final phases of the project, when the modeling of cartilage layers was performed in native Ansys (Section 5.6). During implant shape determination modeling, no cartilage layers were modeled, and Ansys Workbench was used. Thus, in these cases, the assemblies analyzed included the cortical bone, cancellous bone, CPP implant, and Titanium screw solid models.

The assemblies were generated by mating the bone parts by their three reference planes. This was easily accomplished, because all parts were generated based on the cortical bone coordinate system which was preserved during the solid generation of the cancellous bone, implant, screw, and cartilage layers. The assembly for the shape determination stage is shown in Fig. 3.26 and that used for the modeling of the assembly where the cartilage layer was included into the analysis is shown in Fig. 3.27.

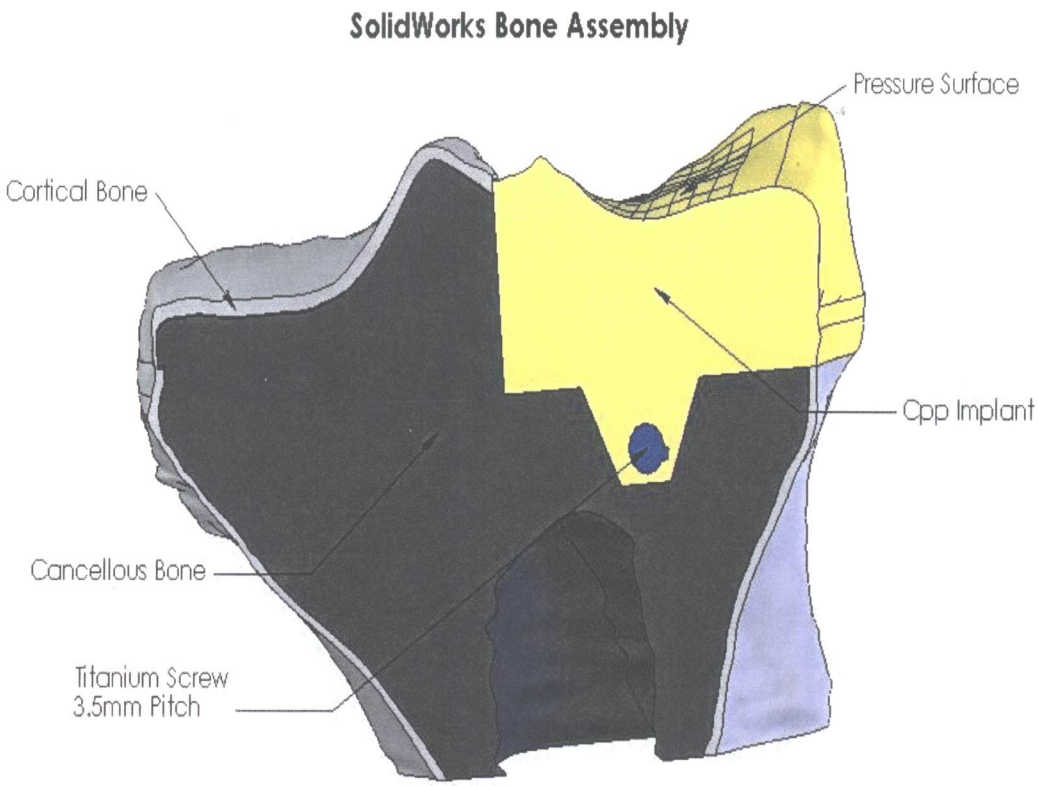

Figure 3.26 Bone assembly for shape determining analysis. Trapezoidal Keel 8mm. 6 mm position

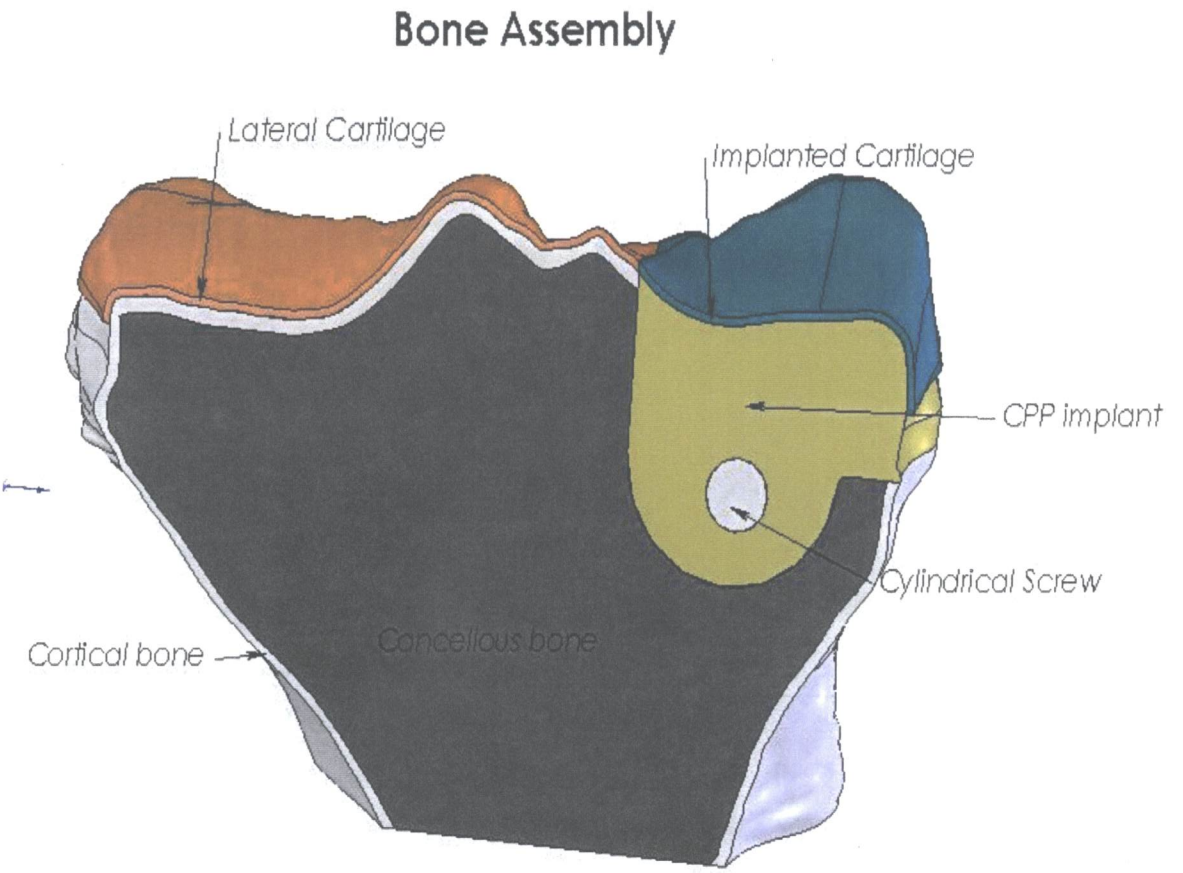

Figure 3.27 Bone assembly final model including cartilage layer. Semicircular keel of 12mm diameter.

CHAPTER 4

Optimization of Implant Shape using Finite Element Analysis: Input of Boundary Conditions and Material Properties

Using the models built during the CAD modeling phase (Chapter 3), a comparative analysis was pursued in order to determine the best possible geometrical shape of the CPP-Implant. For this purpose, all the models were imported into Ansys Workbench v.10.0, and analyzed under identical loading and material properties. A number of different contact conditions between the implant and bone were considered, each with a variety of changes in geometrical shape (and related changes) of the implant. This section describes the material properties, boundary conditions and applied distributed loads used, and the setup of the finite element analyses. The best performing model was further investigated under contact conditions which included frictionless type contact with the purpose of having a complete picture of implant behavior. This consisted the scope of the final stage design.

4.1 Material Properties

4.1.1 Isotropic material model

The majority of the finite element (FE) analyses were performed using isotropic material properties for the bone elements, CPP implant, and screw, in order to reduce the computational time. The isotropic assumption is often used in biomechanical studies of bone/implant systems, when comparative, rather than absolute values are desired [38]. This allowed the various implant geometries to be compared relatively quickly, so that the most promising designs could be selected for more in-depth analysis. Compared to when anisotropic properties for cortical and cancellous bone were used (provided in Tables 4.1 and 4.2), the models solved approximately 10% faster using isotropic properties.

The implementation of material properties into Ansys is straightforward. For the isotropic case, for each material only two inputs are required, Young's Modulus and Poisson's ratio. These values are presented in Table 4.1 for each bone type, CPP implant and Titanium alloy. Isotropic properties were also used to analyze the final, optimized model, representing the best possible choice. In this case, the only variable that changed in the analysis was the different type of contact condition at the various interfaces (Section 4.2).

Table 4.1 Isotropic properties of bone assembly used in Ansys Workbench 10.0

Assembly's Element	Young's Modulus (GPa)	Poisson's Ratio	Tensile Yield/Ultimate (MPa)	Compressive Yield/Ultimate (MPa)
Cortical Bone	20	0.36	115_{Yield}	182_{Yield}
			$133_{Ultimate}$	$195_{Ultimate}$
Cancellous Bone	1.1	0.36	-	-
Fixation Screw	110	0.33	$750_{Yied\ Strength}$	$750_{Yield\ Strength}$
CPP Implant	5.8	0.3	$28_{Ultimate\ Strength}$	$56_{Ultimate\ Strength}$

4.1.2 Anisotropic Material Properties

The assignment of anisotropic bone properties for cortical and cancellous bone was accomplished using a slightly different procedure. Because cortical bone exhibits transversely-isotropic properties [39, 40], a cylindrical coordinate system was defined with the origin at the same position as the global coordinate system. The theoretical background for this type of material properties was given in section 2.1.5, and cylindrical symmetry is described in Section 2.1.7, where the plane of isotropy is the plane on which the radial and tangential directions lie.

For the cylindrical coordinate system used in defining the cortical bone properties (shown in Fig. 4.1), the radial and tangential directions were defined as E_X and E_Y, respectively. As described in Section 2.1.5, the number of input parameters is six.

The cancellous bone was considered to be homogenous anisotropic with three planes of symmetry [39, 40]. The theoretical background for this type of symmetry was described in Section 2.1.4. and the number of required input parameters is nine.

Anisotropic properties of the cancellous bone were applied in relation to the global coordinate system.

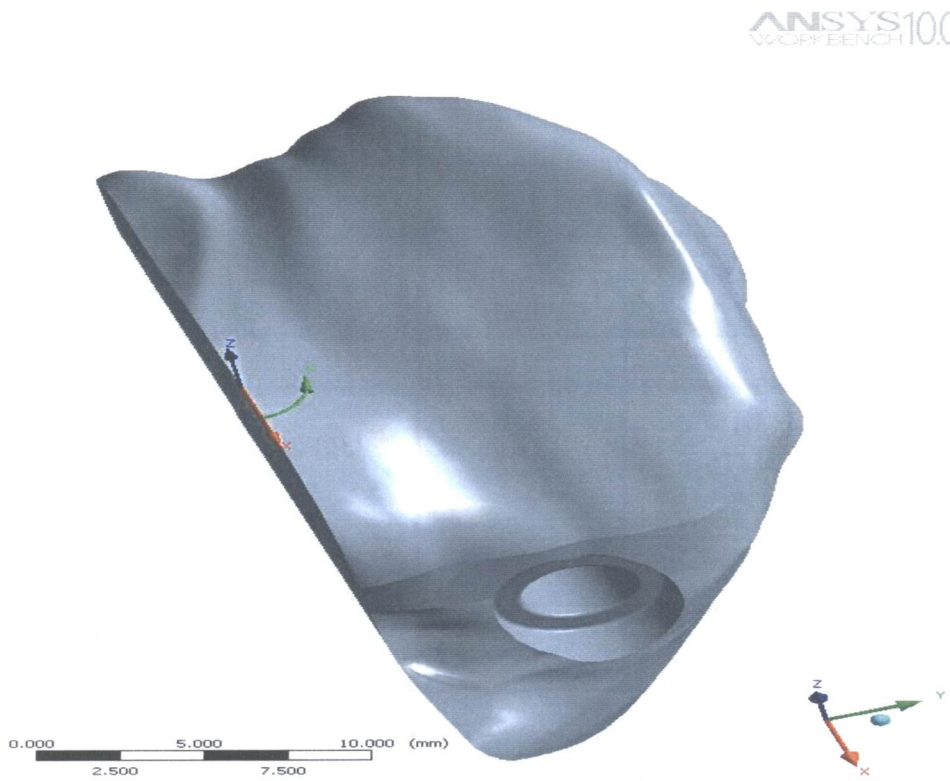

Figure 4.1 Cylindrical and Cartesian Coordinate System in Ansys Workbench 10.0. Cylindrical Coordinate system used to define anisotropic material properties of cortical bone (System shown onthe left) . Global Cartesian coordinate system used to define anisotropic material properties of cancellous bone (system shown bottom right corner). Y-axis aligned with lateral -medial direction, X-axis aligned with dorsal-ventral direction.

Anisotropic properties were imposed on the bone elements only in the final model, with the purpose to evaluate the stability of the design under more realistic conditions. For the sheep cortical bone, the properties were derived from elastic coefficients given in [3]. These coefficients are as follows:

$C_{11} = C_{22} = 17.5$ GPa; $C_{23} = C_{31} = 10.69$ GPa; $C_{44} = C_{55} = 5.11$ GPa (4.1)

$C_{33} = 24.76$ GPa; $C_{12} = 10.15$ GPa ; $C_{66} = 3.67$ GPa (4.2)

Table 4.2 Anisotropic properties of bone elements used in Ansys Workbench 10.0

Assembly's Element	Young's Modulus (GPa)	Poisson's Ratio	Shear Modulus (GPa)
Cortical Bone	16.5 Axial 10.51 Radial 10.51 Tangential	0.489 Radial-Tangential 0.387 Radial – Axial 0.387 Tangential-Axial	7.34 Radial-Tangential 10.22 Radial – Axial 10.22 Tangential-Axial
Cancellous Bone	1 Proximal-Distal Z-Direction 0.6 Ventral-Dorsal X-Direction 0.4 Lateral-Medial Y-Direction	0.36 Distal-Lateral Plane 0.36 Distal-Dorsal Plane 0.36 Doral-Lateral Plane	0.486 Distal-Lateral Plane 0.32 Distal-Dorsal Plane 0.22 Doral-Lateral Plane

Using the inverse of the matrix provided in eq. (2.34) with the coefficients provided in expression 4.1, the elastic properties of the cortical bone given in Table 4.2 result.

The Young's moduli and Poison's ratios for the anisotropic properties of the sheep cancellous bone were taken from [42]. Because anisotropic shear data is not available for sheep cancellous bone, it was considered to be similar to that of human tibial cancellous bone, as it has been found that humans and sheep have similar organic and inorganic cancellous content, resulting is similar anisotropic elastic properties [43].

4.1.3 Design criteria implemented in the analyses

The criteria used to determine the best possible design were maximum stress observed in the model and relative micromotion at the interface between the implant and bone. Limiting values the maximum stresses observed in the CPP implant were thus set at 28 MPa, the ultimate tensile and 56 MPa, and the ultimate compressive stress values. The maximum relative micromotion between CPP implant with cortical/cancellous bone interfaces was limited to 50 μm, a value at which the bone ingrowth process is compromised.

The easiest way to determine the maximum stress and location in the model is through the implementation of the 'failure criteria' option in ANSYS Workbench. Use of this feature resulted in contour plots of safety factor (i.e., ratio of failure stress to calculated stress), which were used to identify the critical areas where fracture or failure was most likely to occur. Selection of the best possible model was based on these safety factors for each CPP implant model.

Depending on the material, three failure criteria were used in the analyses: the maximum tensile stress theory, the Mohr-Coulomb failure theory, and the maximum shear stress theory (i.e., Tresca criterion).

A short description of these failure theories is given in the following:

a) Maximum Tensile Stress Theory [44, 45]

Failure will occur when the maximum principal stresses equals or exceeds the tensile stress limit. This theory can be used for both brittle and ductile materials, depending on the type of the tensile stress considered (Ultimate or Yield stress). For brittle materials:

$$\frac{\sigma_1}{\sigma_{UT}} < 1 \tag{4.2}$$

where σ_{UT} (ultimate stress in tension) is the ultimate tensile or compressive stress for the brittle material. For ductile materials, the theory states that:

$$\frac{\sigma_1}{\sigma_{YT}} < 1 \tag{4.3}$$

where σ_{YT} is the yield tensile stress for the ductile materials.

b) The Mohr-Coulomb failure [44, 45] theory states that failure occurs when the combination of maximum and minimum principal stresses at one location equals or exceed their respective stress limits. The design goal, for this theory, is thus to limit the maximum and minimum principal stresses to their ultimate strength values, expressed mathematically as:

$$\frac{\sigma_1}{\sigma_{UT}} + \frac{\sigma_3}{\sigma_{UC}} < 1 \tag{4.4}$$

where σ_{UT} and σ_{UC} are the ultimate tensile and compressive stresses for brittle materials respectively. The Mohr-Coulomb failure theory can also be applied to ductile materials, by replacing the ultimate stress by the yield stress

c) The Maximum Shear stress failure theory [44, 45] for ductile materials states that failure occurs when the maximum shear stress equals or exceeds a specific shear limit. This theory can be expressed by:

$$\tau_{\max} \geq f \cdot S_{limit} \tag{4.5}$$

Where f is a fraction that can be manually selected, usually taken as 0.5 (Tresca criterion). The limiting value for the stress S_{limit} can be either the yield or ultimate stress. Maximum shear stress τ_{max} represent the maximum value of shear stresses given by the formulas:

$$\begin{aligned} \tau_1 &= \frac{|\sigma_2 - \sigma_3|}{2} \\ \tau_2 &= \frac{|\sigma_3 - \sigma_1|}{2} \\ \tau_1 &= \frac{|\sigma_1 - \sigma_2|}{2} \end{aligned} \tag{4.6}$$

Where σ_1, σ_2, and σ_3, are the principal stresses at a point.

For the Calcium Polyphosphate implant, the two failure theories used were: (i) the maximum calculated tensile stress was compared to the ultimate tensile stress of the CPP implant (Table 4.1), and (ii) Mohr-Coulomb failure theory was applied using the ultimate tensile and compressive stresses. For the Titanium alloy screw, the two failure theories that were used were: (i) the maximum tensile stress was compared with the yield stress of the Titanium alloy (Table 4.1), and (ii) the maximum shear stress theory (Tresca) criterion was applied using the yield stress.

4.2 Distributed Applied Load and Boundary Conditions

The loads applied onto the tibial plateau, were provided in the form of a distributed pressure, locally normal to the surface, from *in-vivo* Fuji pressure film measurements on a sheep. This pressure film had a minimum sensitivity value of 2 MPa, which meant that values of pressure smaller than this value were recorded as zero. The reference coordinate

system has its origin at the lowest point between two tips on the tibia plateau (Fig 4.2). These loads correspond to a three year old sheep weighting 60 Kg.

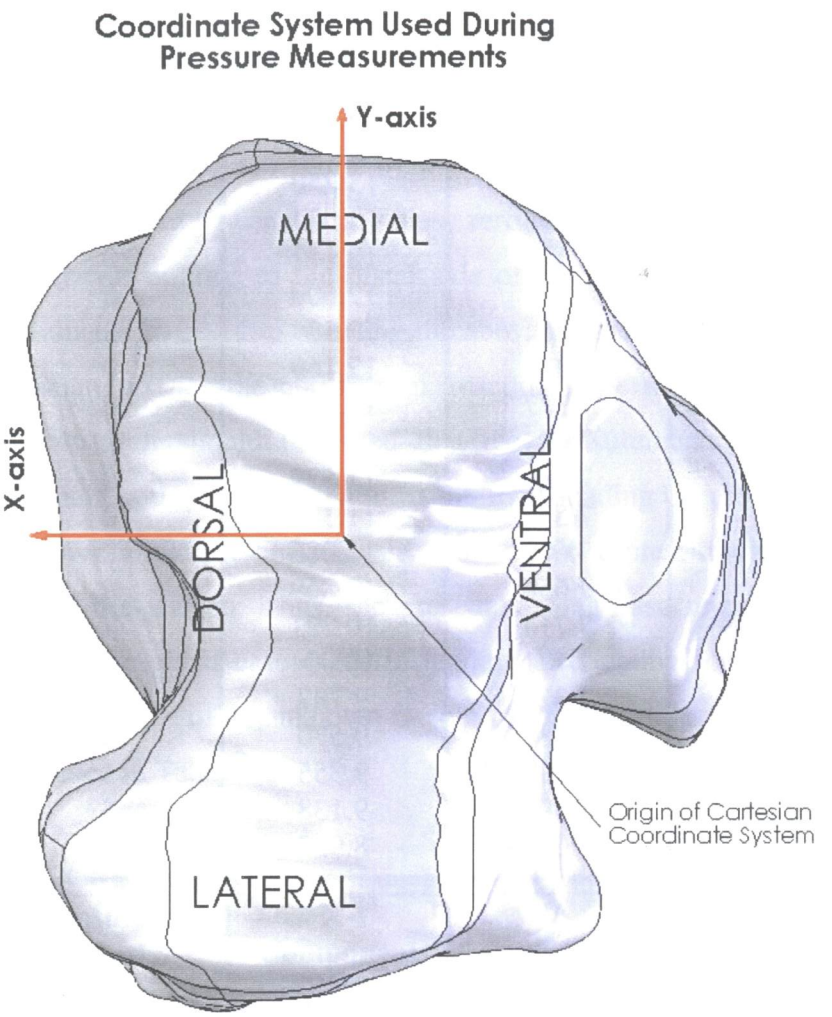

Figure 4.2 Origin of coordinate system used for load distribution measurement

The reference axis directions during the FE analysis are shown in Figs. 4.2 and 4.3, with the z-axis being perpendicular to the X-Y plane and pointing in the direction of the reader.

Table 4.3 Sample of load distribution over tibia plateau

X *(mm)*	Y *(mm)*	Pressure *(Mpa)*
6.702	14.416	0
6.758	14.332	0
6.814	14.116	0
6.871	13.899	0
6.927	13.683	0
6.983	13.466	0
7.039	13.250	0
7.096	13.034	0
7.152	12.812	0
7.2.9	12.600	0
7.264	12.384	0
7.321	12.169	0
7.377	11.952	0
7.433	11.735	2
7.789	11.529	0
7.545	11.302	0
7.602	11.086	2
7.658	10.869	0
7.714	10.221	4
7.771	10.004	5
7.827	9.787	4
7.882	9.570	5
7.939	9.355	5
7.995	9.138	5
8.052	8.922	8

The average of the pressure data, when considering all the zeroes as true pressure values, was 1.3 MPa. When considering these zero values to be just below the sensitivity threshold $(\approx 2MPa)$, the average of the data was 3.2 MPa.

In the Fuji film measurements, only the normal pressure was measured. To account for the unmeasured tangential stress over the tibial plateau, the raw data was used in the following manner, resulting in an average stress of 5.3 MPa. Because the loads were provided as pressures at various coordinates on the tibial plateau, and Ansys only allows pressure to be applied over finite areas, it was necessary to divide the tibial plateau surface into a number of finite load application surfaces, as described in Section 3.2. Each pressure application surface had an x-direction length (on the xy-plane) of 2.18 mm

and a width of (y-axis) of 1.28 mm, as shown in Fig. 3.23. The applied pressure on each of these surfaces was held constant at the value described using the following procedure: In cases where, within the pressure surface the corresponding pressure data were all zeroes, the pressure applied in the analysis was 2 MPa. When the data for a pressure surface was greater than 5 MPa, all zero pressure values were disregarded in the load value determination. Lastly, for the cases when the majority of the data values with a given pressure surface were zero, and there were values between 2 and 5 MPa, the average pressure was determined by considering these zero data values to be 2 MPa.

A fixed support was applied to the distal side of the model, and the resultant reaction force was evaluated to be 1296 N, using the above pressure estimation scheme. This value is approximately twice the 600 N peak reaction force measured in a sheep during a gait cycle [46]. It should be noted that the measurements of [46] were performed during the gait cycle as the reaction to the total loading on the sheep knee, whereas the reaction force in the present analysis was a result of pressures applied only over the medial part of the plateau. Thus, the present loading case represents a very conservative estimate of the worst case scenario loading, accounting for any sheep to sheep variation in knee loads, or other unknown factors. Reaction forces evaluated at the fixed supports are provided in Table 4.4.

Table 4.4 Reaction forces and their components at fixed supports

Fixed Support	Resultant Reaction (N)	X-Component (N)	Y-Component (N)	Z-Component (N)
Cortical	**790.2**	**149.2**	**-59.9**	**773.7**
Cancellous	**506.3**	**26.9**	**-52.9**	**502.8**

Due to the very complicated plateau surface pattern, the nature of the load played a critical role on the stability of the implant, not only because of the value and location of the maximum compressive/tensile stresses observed on the CPP implant/Cortical (Cancellous) interfaces, but also the value and location of interfacial micromotion

observed in each individual model. These observations will be presented in detail in Chapter 5.

4.3 Force applied by Fixation Screw

The fixation screw provided a force that kept the implant attached to the bone, and which could be conveniently implemented in Ansys using the "bolt force" option. Evaluation of the force applied on the fixation screw was based on axial deformation theory, where the force was evaluated for different geometric misfit values. These values were chosen to be 20, 50, 100, and 200 μm. The geometrical misfit is the difference in length of the screw between the case where the screw head is just snug up against the CPP implant with the cases where the screw is tightened resulting in its length being shortened by the amount assigned. The geometric parameters used in the evaluation of the bolt force are shown in Fig. 4.4.

The sum of the axial forces is:

$$F_1 + F_2 = 0 \tag{4.7}$$

where F_1 is the force exerted by the screw head on the CPP implant and F_2 is the CPP reaction.

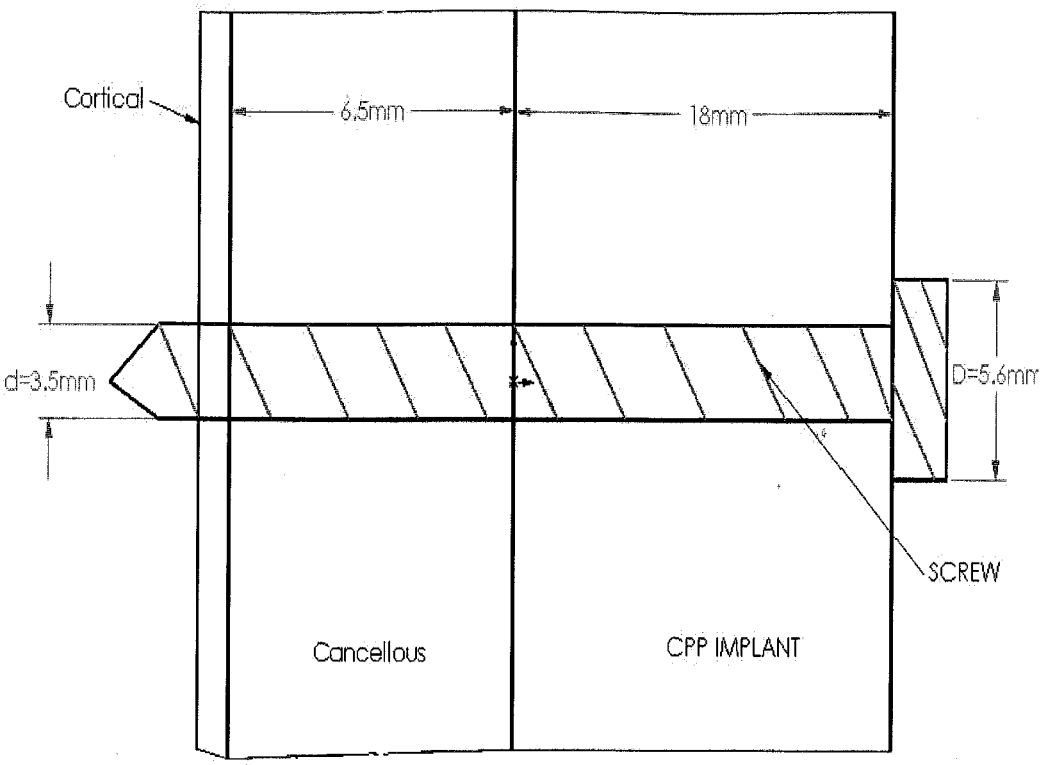

Figure 4.3 Bolt Force. Parameters used in calculations

Elongations are evaluated by the formulas:

$$\begin{cases} e_{screw} = f_{screw} F_{screw} \\ e_{CPP} = f_{CPP} F_{CPP} \\ e_{CANC} = f_{CANC} F_{CANC} \end{cases} \tag{4.8}$$

where e_{Screw}, e_{CPP} and e_{CANC} are the elongations that the screw, CPP and cancellous bone experience, and f_{Screw}, f_{CPP} and f_{CANC} are the flexibility coefficients of the screw, CPP implant and cancellous bone. The formulae for calculating the flexibility coefficient are given below:

$$\begin{cases} f_{screw} = \left(\dfrac{L}{AE}\right)_{screw} = \dfrac{(24.5)(10^{-3})}{\pi\left(\dfrac{3.5}{2}\right)^2 (10^{-3})^2 \cdot 110(10^9)} = 0.023(10^{-6})\,m/N \\ f_{CPP} = \left(\dfrac{L}{AE}\right)_{CPP} = \dfrac{(18)(10^{-3})}{\pi\left[\left(\dfrac{5.6}{2}\right)^2 - \left(\dfrac{3.5}{2}\right)^2\right](10^{-3})^2 \cdot 5.8(10^9)} = 0.207(10^{-6})\,m/N \\ f_{CANC} = \left(\dfrac{L}{AE}\right)_{CANC} = \dfrac{(6.5)(10^{-3})}{\pi\left[\left(\dfrac{5.6}{2}\right)^2 - \left(\dfrac{3.5}{2}\right)^2\right](10^{-3})^2 \cdot 1.1(10^9)} = 0.394(10^{-6})\,m/N \end{cases} \quad (4.9)$$

These calculations assumed that the axial force is transmitted to the CPP implant and cancellous bone (Fig. 4.4) through a tube with outer diameter equal to the outer diameter of the screw head (D = 5.6 mm) and the inner diameter equal to the outer diameter of the screw body (d = 3.5 mm).

Geometric compatibility requires that:

$$e_{screw} - (e_{CPP} + e_{CANC}) = \delta \quad (4.10)$$

where δ is the amount of the distance that working length of the screw shortens during the tightening of the screw. Replacing the expressions for the elastic elongations evaluated by eq. 4.8, eq. 4.10 yields:

$$f_{screw} F_{screw} - (f_{CPP} + f_{CANC}) F_{reaction} = \delta \quad (4.11)$$

By solving equations (4.11) and (4.7) simultaneously, for different value of unknown δ, the corresponding values of the force exerted (Bolt force) can be evaluated and are tabulated in Table 4.5.

Table 4.5 Bolt force vs. displacement

Displacement 'δ' (μm)	Bolt Force (N)
50	80
100	160
200	320
500	801

The effect of the bolt force applied to the assembly is investigated only for the final optimized model. During the comparative analyses, the bolt force was considered to be 75 N. The effect of the tightening force can be found in Chapter 5.

4.4 Treatment of Contact Conditions in Finite Element Analysis

The determination of the best design was greatly affected by the type of contact selected during the analysis. It was assumed that the contact areas remained well defined during the lifespan of the implant (i.e., the geometrical shape of the CPP remained unchanged) despite the bone ingrowth process, thus assumed that only the contact formulation changed as the bone ingrowth process occurred. Contact combinations used to describe the various situations during the implant life span are listed in table 4.6.

Table 4.6 Combinations of contact types used in comparative analyses

CONTACT Combinations		CPP Implant				Cortical Bone	Fixation Screw	
		Cortical Bone	*Cancellous Bone*	*Screw-Body*	*Screw-Head*	*Cancellous Bone*	*Cortical Bone*	*Cancellous Bone*
Comparative Stage	*1*	*Bonded*	*Bonded*	*Bonded*	*Noseparation*	*Bonded*	*Bonded*	*Bonded*
	2	*Noseparation*	*Noseparation*	*Bonded*	*Noseparation*	*Bonded*	*Bonded*	*Bonded*
	3	*Noseparation*	*Noseparation*	*Noseparation*	*Noseparation*	*Bonded*	*Bonded*	*Bonded*
Final Modeling Stage	*4*	*Bonded*	*Bonded*	*Noseparation*	*Noseparation*	*Bonded*	*Bonded*	*Bonded*
	5	*Noseparation*	*Bonded*	*Noseparation*	*Noseparation*	*Bonded*	*Bonded*	*Bonded*
	6	*Frictionless*	*Frictionless*	*Friction*	*Friction*	*Bonded*	*Bonded*	*Bonded*
	7	*Frictionless*	*Frictionless*	*Frictionless*	*Frictionless*	*Bonded*	*Bonded*	*Bonded*

The bonded type contact describes a glued contact where no sliding or separation between the surfaces is allowed, any existing gap is closed, and all initial penetration is. In Ansys, No-separation type contact is treated the same as Bonded type, except that a small amount of frictionless sliding is allowed. For both of the above types of contact the solution is linear because the contacting surfaces remain unchanged during the FE solution.

With all other parameters kept unchanged, each CPP implant model was analyzed with the different combinations of contact conditions outlined in Table 4.6. As mentioned in Chapter 1, due to the stress level and micromotion requirements that the implant structure must fulfill, the comparative stage of the design was based on the result of the three contact conditions combinations provided in Table 4.6. These contact conditions approximately reflect the real situation that the CPP implant would encounter during its life span after the surgical insertion. The material properties of the calcium polyphosphate implant were assumed to remain constant in the initial stages of bone ingrowth despite the biodegradation process.

4.4.1 Contact Type selection

There is a variety of contact options available in Ansys to represent the different interface conditions. For bonded and no-separation type contact regions, choosing one pair of contacts causes the automatic closure of any possible gaps and any penetration is ignored in the analysis. The only difference between the bonded and no-separation type is that, for the former, the surfaces are glued together (sliding and separation are not allowed), and for the latter, some small amount of frictionless sliding is allowed between the surfaces. In both bonded and no-separation contacts, separation of the surfaces is not allowed [44]. For these types of contacts, the solution is linear since the contact areas do not change during the load application.

When selecting frictionless and frictional type contacts, the contact interfaces need to be adjusted so that they barely touch. For both of these type of contacts, relative

separation of the contact surfaces can occur, and when this happens, the normal pressure is set equal to zero. For the frictionless case, the friction coefficient is considered zero, allowing free sliding between the surfaces. For the frictional case, sliding occurs when the shear stresses exceed a certain value (determined as a fraction of the contact pressure). For shear stresses smaller than this value, sticking will occur. For both of these types of contact, the solution obtained is nonlinear since the surface regions which are in contact can change during loading [44].

A bonded type contact between the CPP Implant and the cortical and cancellous bone was considered to exist after the surgical insertion of the implant, due to the presence of the screw. As indicated in [27], bone ingrowth is normally observed within CPP for a period of six weeks after the insertion. Thus, to represent the time span from implantation to six weeks, at the CPP implant-cortical/cancellous bone interfaces, bonded, no-separation and frictionless contact types were compared. The contact condition of no-separation and frictionless type is used to describe the early stages after the implant insertion. The no-separation type contact leads to smaller solutions time and it is used in the comparative stages of the design.

The interfaces between the fixation screw and both the cortical and cancellous bone regions were always represented as bonded, an approximation accounting for the 'bite' of the screw threads. For the screw-CPP implant interface, several conditions were considered. This interface was considered bonded, if the screw was fixed to the CPP implant with a hole diameter smaller than or equal to the major diameter of the fixation screw. If, however, the screw was inserted into the CPP implant with a hole diameter larger than the major screw diameter, then either no-separation or frictionless type contact conditions were selected. The interface between the fixation screw head-CPP implant was described by a no-separation or friction type contact. For the latter, the friction coefficient was approximated as the value of the interface between Titanium and wood (another porous cellular material); i.e. $\mu = 0.3$ [48], since the true value of the coefficient of friction for interface Titanium-CPP material is unknown. The interface between cortical and cancellous bone was assumed to be bonded, for all FE simulations.

4.4.2 Contact behavior and solution algorithm

Based on Ansys guidelines [44], contact pairs were selected depending on the type of material constituting the pair. Each contact pair, selected manually, was composed of two surfaces: 'Contact' and 'Target' surfaces which were selected as such based on the guidelines provided in [45], presented as well in the first paragraph of Section 4. The number of contact surfaces between implant and cortical/cancellous bone was dependent on the type of keel used (trapezoidal or semi-cylindrical), the size of the keel, and the position of the keel relative to vertical implant's surface. In a contact pair, the surface belonging to the softer underlying material was selected to be the 'Contact' surface, while the surface belonging to the stiffer underlying material was selected to be the 'Target' in the contact pair. Besides the interface between cortical and cancellous bone where symmetric behavior was preferred, for all other interfaces the behavior was selected to be asymmetric ("one- pass contact" where one surface of the contact pair is designated as contact and the other as target). This selection was based on the fact that for this type of behavior, the sliding between the contacting surfaces is better captured using asymmetric type behavior compared to the symmetric type. When the symmetric type of contact is selected, Ansys generates two (companion) identical contact pairs based on the surfaces chosen, where each pair is identical to the target surface of its companion, and vice versa [42]. The scope mode in Ansys describes the method used in selecting the contact surfaces, either manual or automatic. An automatic type was selected for cortical-cancellous bone, fixation screw–Cortical bone, and for fixation screw-Cancellous bone interfaces. For all other interfaces, manual contact regions were preferred, due to the advantages in modeling possible large sliding that this type of contact modeling possesses compared to automatic contact detection [42]. Another reason for use of manual contact is related to the fact that during contact modeling, unnecessary extra surfaces were observed when initial automatic contact was accomplished by Ansys Workbench for the CPP implant-cortical bone and CPP implant-fixation screw interfaces. Table 4.7 gives the contact data used in the final model.

Table 4.7 Contact regions. Final model

Contact Interface	Type Of Contact	Number of Contact Regions	Scope Mode	Contact/Target In Contact Pair	
				Contact Surf.	Target Surf.
Cortical Bone – CPP Implant	*Asymmetric*	*3*	*Manual*	*CPP Implant*	*Cortical Bone*
Cancellous Bone – CPP Implant	*Asymmetric*	*4*	*Manual*	*Cancellous Bone*	*CPP Implant*
Cortical Bone – Titanium Screw	*Asymmetric*	*1*	*Automatic*	*Cortical Bone*	*Titanium Screw*
Cancellous Bone – Titanium Screw	*Asymmetric*	*1*	*Automatic*	*Cancellous Bone*	*Titanium Screw*
CPP Implant – Titanium Screw	*Asymmetric*	*2*	*Manual*	*CPP Implant*	*Titanium Screw*
Cortical Bone – Cancellous Bone	*Symmetric*	*1*	*Automatic*	*Cancellous Bone*	*Cortical Bone*

Two solution algorithms were used in this project: the penalty method and augmented Lagrangian method. The bulk of the analyses were based in the usage of the Augmented Lagrangian, because it has some advantages over the Penalty method, as described in Section 2.5. The penalty method was used for comparative purposes, where the solutions obtained were compared to the solutions obtained using the Augmented Lagrangian method. The difference between the results obtained using these two methods is described in Section 5.2.

The solution convergence was heavily dependent on the type of the contact selected. For the combinations of contact conditions consisting of only bonded and no separation, the convergence for the linear solution was obtained based on a convergence factor of 13% (a convergence factor of smaller than this value was not possible to obtain). For the combination involving the nonlinear effects introduced by the presence of the frictional and frictionless type contacts, the solutions convergence were based on a convergence factor of 20%, and below this value the solution took unrealistically long time to be completed for smaller convergence criteria. During the solution of the nonlinear type conditions, auto time stepping was introduced into the solution with maximum substep number of 1000 (step size of 100). The adaptive convergence is a method integrated within the solution process and is based on the error norms and other information output of the solver. It two main option are the refinement loops and depth. Adaptive convergence settings were selected to be at their maximum: refinement loops were selected at ten and the refinement depth at three. These settings for the comparative stages were chosen to be seven and two respectively.

The solution for the nonlinear case was obtained for a modified version of the final model shown in Fig. 3.21. The final model shown in Fig. 3.20 did not converge due to the stress concentration observed in the horizontal surfaces near the tip of the keel's back surface. This type of solution, contact combination 6 and 7 as listed in table 4.6 was applied only to the final model due to the time required for achieving the converged solution.

4.5 Model Mesh

Meshing of the solid model was accomplished using Solid187 Ansys elements, having a tetrahedral shape, and a quadratic displacement behavior. Tetrahedral elements are well suited to modeling cortical, cancellous, and CPP implants, which possess highly irregular geometrical shapes. Because Solid187 elements which were used to mesh the underlying solids are high-order element (i.e. elements with midside nodes), meshing of the contact regions was accomplished using 3D 8-Node surface to surface contact elements (Contact174) and their associated element 3D target element (Target170). Detailed descriptions of the solid and contact elements can be found in [44].

The accuracy of the analysis is intrinsically related to the accurate finite element modeling of the contact between the assembly elements, and thus mesh refinement was performed over the contact regions describing the interface between the CPP implant and the fixation screw, cortical, and cancellous bone. In Ansys workbench, the 'relevance' controls the mesh density in a given surface, component, solid, etc. The higher the value of relevance selected, the finer the resulting mesh, giving more accurate results, with a penalty in the computational speed (maximum relevance is +100). Exploiting all the elements limited by the FE package license (maximum of 125,000 nodes or elements), meshing of the cortical, cancellous bone, and CPP implant was performed with the relevance value set at -50 (-100 for high speed and +100 for high accuracy). The relevance of the fixation screw was left at the default value (zero relevance). Then the contact regions mentioned above were refined with the following element sizes for the maximum mesh density: CPP implant-Cortical bone contact region having an element size of 0.5 mm, CPP implant-Cancellous bone with 0.6 mm, and for the fixation screw – CPP implant contact region, the refining was done with contact element size of 0.65 mm. Contact regions between the fixation screw- cortical /cancellous bone, and the region between cancellous-cortical bones were left unchanged from the mesh density constructed with the initial relevance. The dependency of the solution from mesh density is the treated in section 5.2.

Tables 4.8 and 4.9 show the types and the number of elements used in meshing the solid models and contact regions for the two extreme cases. The first is the case with the minimum possible relevance, with no refinement introduced into the assembly, and the second represents the maximum possible mesh density achievable with the limits on the Ansys license.

The number of nodes for the FE model with a minimum mesh density was 35,801 and the overall number of active elements was 26,683. For the maximum mesh density FE model, where the refinement of the contact region was completed, the overall number of elements was 95,428 (including solid and contact elements) and the number of nodes was 124,056. These statistics correspond to the FE modeling of the CPP implant where the cartilage layer was not included. Information regarding the modeling of the cartilage layer is provided in Chapter 6.

Table 4.8 Solid meshing

Solid	Element Type	Minimum Mesh Density *(Element Number)*	Maximum Mesh Density *(Element Number)*
Cortical Bone	*Solid 187*	*7088*	*13084*
Cancellous Bone	*Solid 187*	*7635*	*29439*
CPP Implant	*Solid 187*	*1652*	*33758*
Fixation Screw	*Solid 187*	*4344*	*4288*

Table 4.9 Contact mesh refinements

Contact Region Number	Contact Region	Minimum Mesh Density Element Number		Maximum Mesh Density Element Number	
		Contact	*Target*	*Contact*	*Target*
1	*Cancellous-Cortical Bones*	*1408*	*2625*	*3561*	*4320*
2	*Cortical Bone- Fixation Screw*	*20*	*31*	*38*	*20*
3	*Cancellous Bone-Fixation Screw*	*51*	*107*	*202*	*172*
4	*CPP Implant-Fixation Screw (Body)*	*110*	*277*	*539*	*646*
5	*CPP Implant-Fixation Screw (Head)*	*215*	*272*	*190*	*268*
6	*Cancellous Bone-CPP implant (Vertical Surface)*	*38*	*55*	*555*	*623*
7	*Cancellous Bone-CPP Implant (Horizontal Surface)*	*89*	*89*	*576*	*680*
8	*Cancellous Bone-CPP Implant (Keel Back Surface)*	*46*	*42*	*214*	*224*
9	*Cancellous Bone-CPP Implant (Keel Conical Bottom Surface)*	*56*	*58*	*826*	*943*
10	*Cancellous Bone-CPP Implant (Vertical Surface)*	*55*	*42*	*594*	*116*
11	*Cancellous Bone-CPP Implant (Horizontal Surface)*	*62*	*32*	*602*	*94*
12	*Cancellous Bone-CPP Implant (Keel Conical Bottom Surface)*	*58*	*28*	*924*	*71*

Figures 4.4 -4.8 show the final meshed model of the cortical, cancellous bone, CPP implant, and fixation screw respectively, for the case of an implant having a semi-cylindrical 6 mm radius keel cross section, and a conical shaped keel back end. The figures show the case of maximum mesh density, where the mesh refinements took place at contact surfaces, as described above

One major factor in determining the element number is the quality of the surfaces imported into Ansys Workbench, where the presence of many small lines is inherited not only from the initial stage of CT scan translation using MIMICS, but also from the CAD repair stage using Rhinoceros 3.0. Some of these small lines were removed using SolidWorks, resulting in a satisfactory mesh distribution in the meshed model in Ansys Workbench. This problematic situation was completely overcome when the model was analyzed in Ansys (rather than Ansys Workbench), where the presence of the CAD repairs tools enabled the possibility to eliminate the small lines (average length of 0.1 mm). The CAD repair procedure in Ansys will be explained in Chapter 6, where the modeling of the cartilage layer is presented.

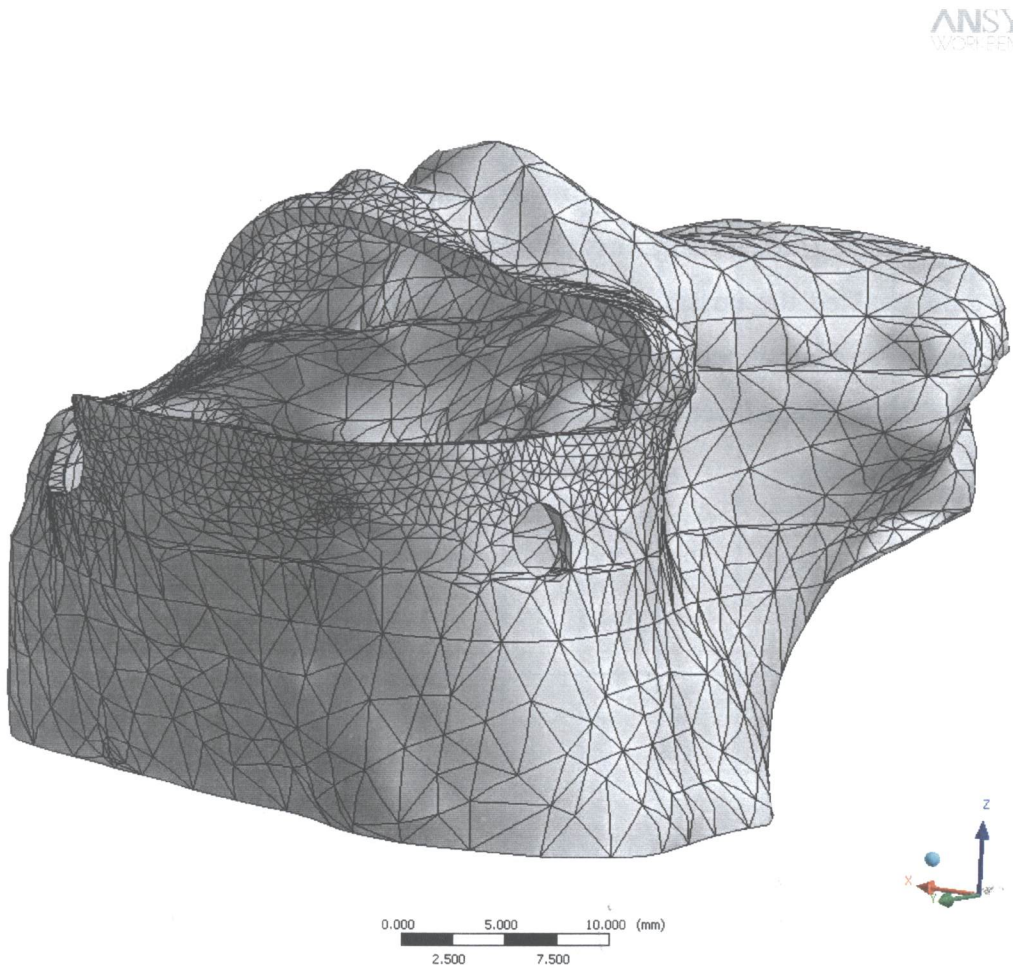

Figure 4.4 Mesh of the cortical bone solid model

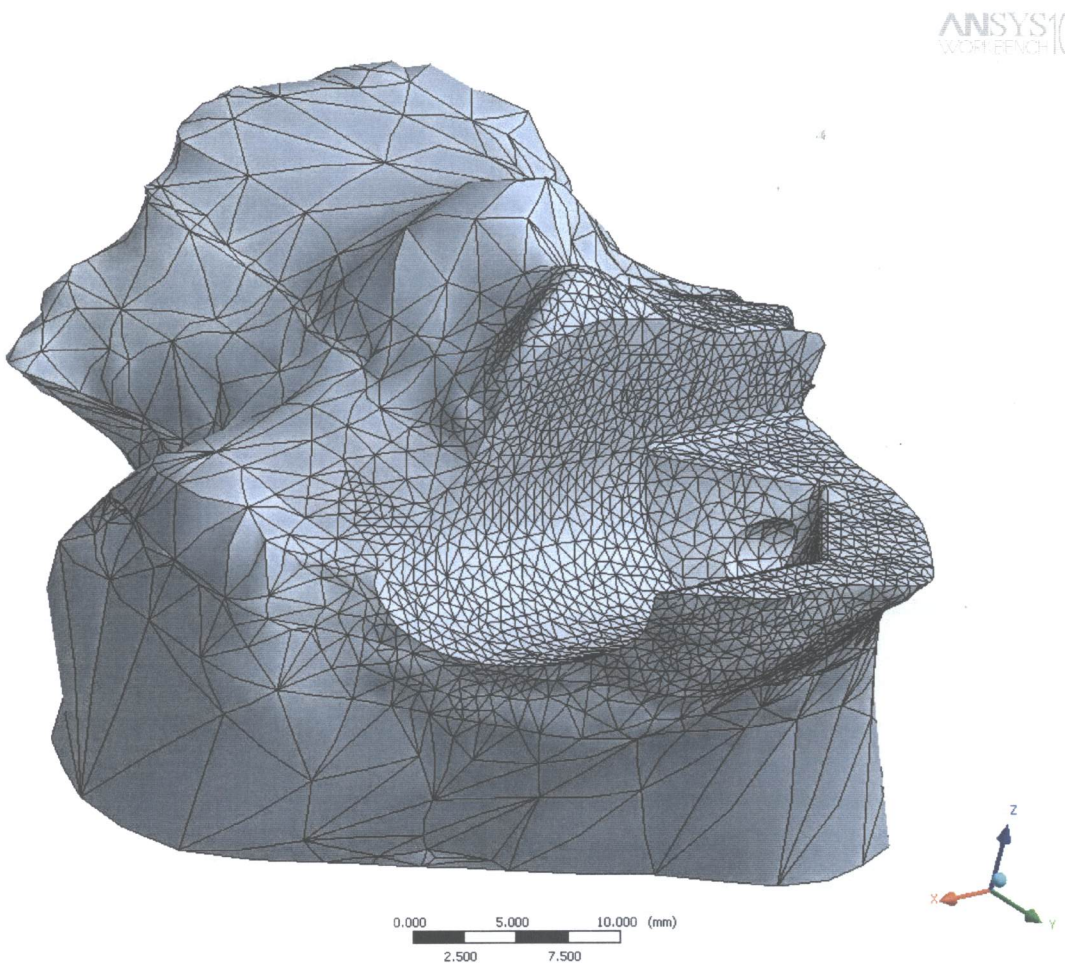

Figure 4.5. Mesh of the cancellous bone solid model

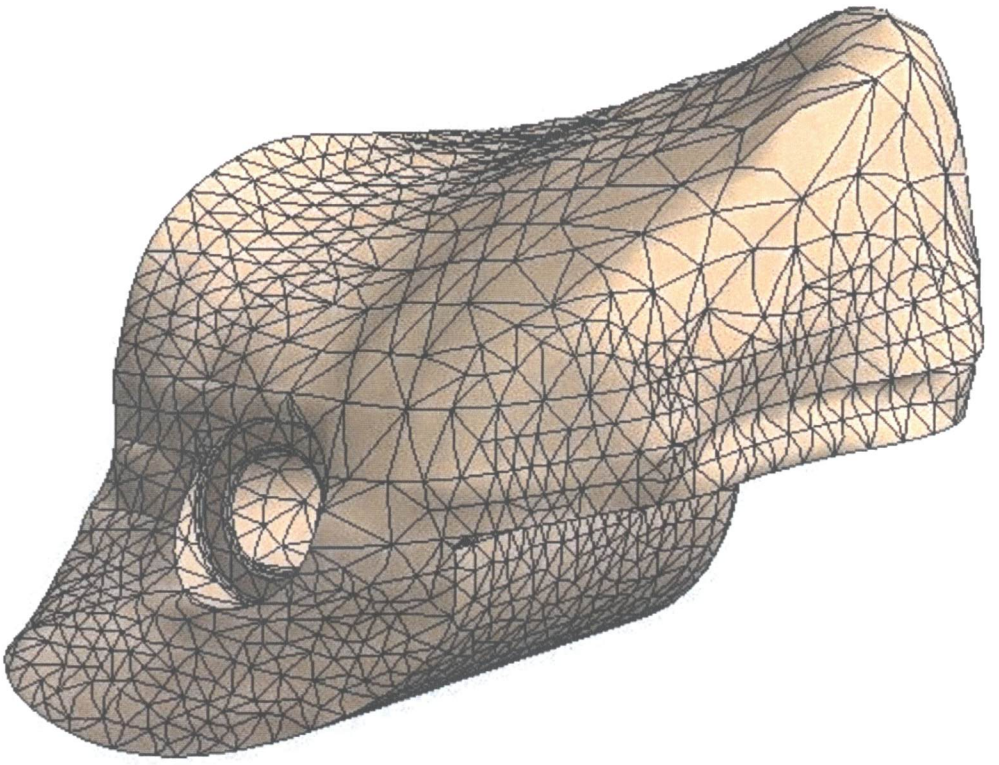

Figure 4.6 Mesh of the CPP Implant solid model. Final Design. Ventral-Dorsal view

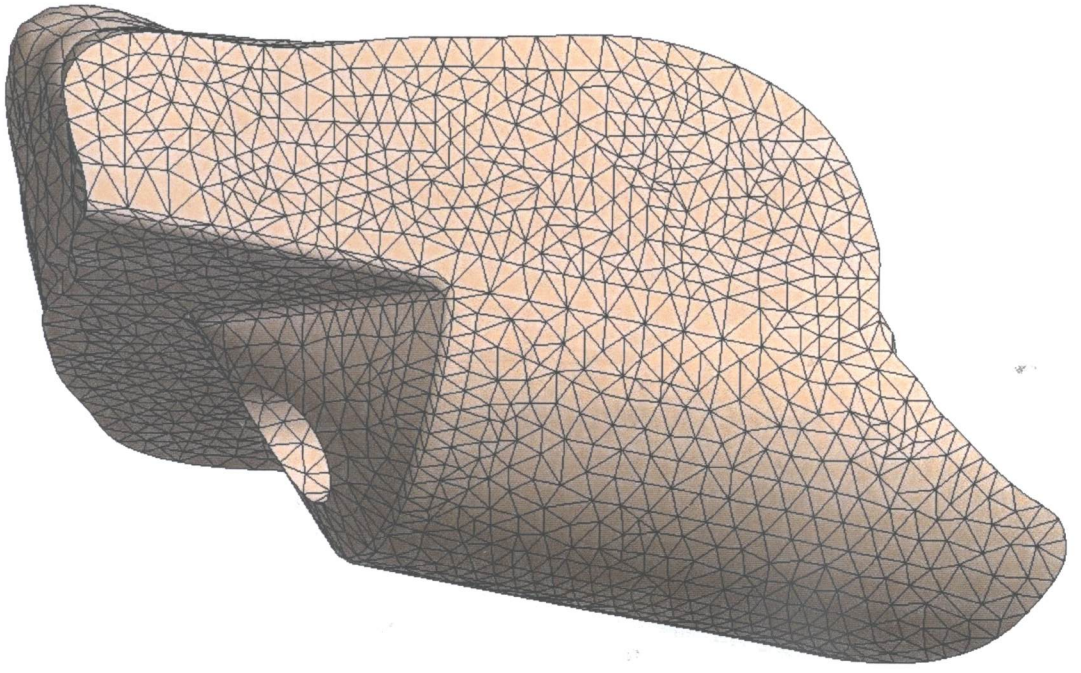

Figure 4.7 Mesh of the CPP Implant solid model. Final Design. Lateral-Medial view

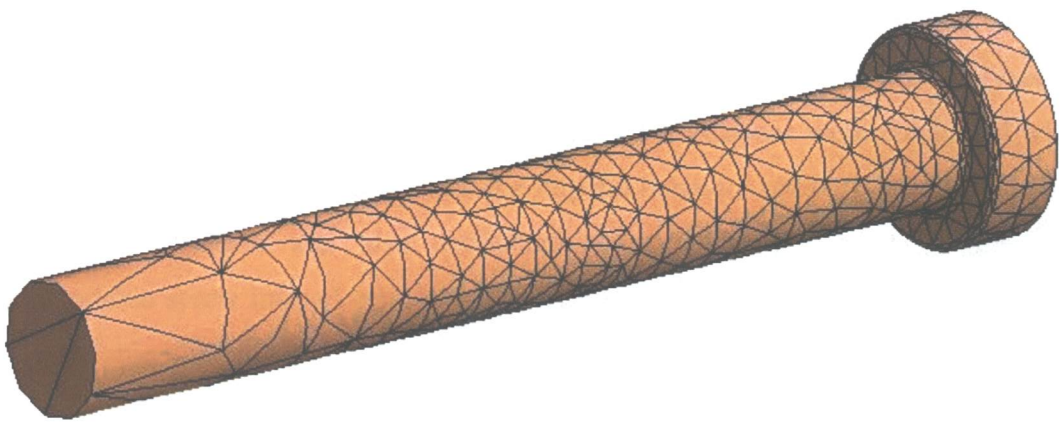

Figure 4.8. Mesh of the fixation screw solid model. Simplified titanium screw

CHAPTER 5

Finite Element Analysis
Results and Discussions

In this chapter, the derivation of the optimal geometrical shape through finite element analysis results will be presented. There are several factors considered during the design including geometrical, formulation characteristics such as various contact type implementations, and surgeon preferences.

The initial design stage of the project is presented in section 5.1, where the design was based upon the whole medial side of the tibia. The design of the model based on the partial medial part of the tibia was based upon surgeon preferences. Another surgeon input is related to the geometrical shape of the keel analyzed. The preference was towards a geometrical shape which was easy to be generated over the bone in real surgical conditions. Therefore a keel with geometrical shape which would imitate the imprint left by a simple vertical movement of the surgical drill bit was analyzed. This analysis is presented in section 5.2, where several FE analyses were conducted with the purpose of gathering information about the implant behavior over different stages of bone healing. Investigation was also conducted towards the possibility of the use of biodegradable screw instead of surgical titanium screw, which would have led to a total biodegradable implanting process.

Reliability of the solutions obtained was the focus of the section 5.3. In this section, the solution based upon maximum and minimum parameters value (such as stress, reaction force, etc.), and for values at specific locations (use of probes) was analyzed for different element size.

The experimental analysis was conducted on the final model of the design, and the result and considerations are presented in section 5.4. In this section, a FE model was constructed approximately to the assembly of the experimental model, for comparison purposes.

5.1 Complete medial implant design

In the present section is presented the first step in the design of the biodegradable implant, which consisted of the design of the medial half of the tibial bone plateau. During this stage, the first two combinations of contact types in Table 4.6 were considered, implemented for the keel with trapezoid cross-sectional shape with a base (i.e., the larger length) of 8 mm and 12 mm. The first type of implant was used to determine the dependency of the performance on the keel orientation, and is presented in section 5.1.1. Section 5.2.1 is presents the design of the straight oriented keel with base width of 12 mm. The screw insertion angle (Figure 3.19) was held at 10^{o} for these cases.

5.1.1 Dependency of implant performance upon keel orientation.

Implant models under investigation had their keel oriented relative to the vertical face of the implant in different angles as shown in Figure 3.17. These angles of orientation varied from zero where the insertion direction of the implant was ventral-dorsal to 90^{o} where the insertion direction was medial-lateral. The large base length of the keel was 8 mm and was maintained unchanged during this investigation. The results returned by FE analysis for each of the models are listed in Tables 5.1 and 5.1 for contact combinations one and two respectively. Isotropic material properties are assumed and the material properties implemented are listed in Table 4.1.

Implant stress distribution and sliding distances of the implant bone interfaces, for contact combination one are well under the tensile strength of the CPP material indicating that for this combination the implant structure was well behaved. The same conclusion can be reached based on the sliding distances listed at the last column, where the maximum sliding distance is registered for the 0^{0} angle orientation and the minimum for the 90^{o} degree. There are three models for which the compressive stress experienced by the implant exceeded the tensile strength in compression of the CPP (56 MPa). These models correspond to the angle orientations of 15, 20, and 70^{o}. The model with keel orientation of 80^{o} has resulting principal stresses which also exceed the compressive strength of the CPP material resulting in the drop of safety factor in compression below unity.

Table 5.1 Stress distribution and maximal sliding distance for trapezoidal cross-section keel in different angles. Contact combination 1

Angle	Normal Stress (MPa) Proximal-Distal z-axis		Normal Stress (MPa) Lateral-Medial y-axis		Normal Stress (MPa) Dorsal-Ventral x-axis		Shear Stress (MPa) x-y Plane		Shear Stress (MPa) x-z Plane		Shear Stress (MPa) z-y Plane		Sliding Distance (10^{-6})
	Max Tensile	Max Comp	Max Tensile	Max Comp	Max Tensile	Max Comp	Max Positive	Max Neg.	Max Positive	Max Neg.	Max Positive	Max Neg.	
0	6.44	-10.7	7.2	-6.9	7.2	-4.5	6.2	-4.9	7.5	-5.8	12.9	-7.3	16
5	21.2	-35.5	16.2	-12.7	0.8	-6.2	7.7	-5.5	11.5	-10.8	8	-8.5	15
10	10	-23.2	6.8	-9.0	2.9	-8.6	10.1	-7.9	6.2	-6.8	6.2	-4.1	11
15	2.9	-62.8	11.6	-8.4	8.5	-3.5	7.6	-5.6	3.6	-11	3.5	-2.5	9.4
20	9.2	-63.0	11.6	-8.4	14.4	-11.0	7.2	-13.3	3.6	-2.5	7.2	-13.3	12.2
30	4.9	-13.6	4.9	-9.9	8.6	-14.2	6.1	-6.2	2.8	-2.7	1.4	-2.7	1
40	5	-15	20.4	-25.4	9.9	-14.1	6.7	-4.4	9.5	-14.5	4.5	-7	1
70	1.9	-61.2	7.7	-7.7	6.7	-6.3	10.9	-9.1	2.3	-11.4	3.2	-3.7	0.4
80	4.2	-50.9	8.6	-34	17.5	-18.9	8.1	-8.6	6.4	-8.6	3.7	-6.4	2
90	-74.4	10.3	11.4	-16	7.3	-8.2	6.4	-6.1	5.5	-3.9	6.3	-8.7	0.5

Table 5.2 Stress distribution and maximal sliding distance for trapezoidal cross-section keel in different angles. Contact combination 2

Angle	Normal Stress (MPa) Proximal-Distal z-axis		Normal Stress (MPa) Lateral-Medial y-axis		Normal Stress (MPa) Dorsal-Ventral x-axis		Shear Stress (MPa) x-y Plane		Shear Stress (MPa) x-z Plane		Shear Stress (MPa) z-y Plane		Sliding Distance ($10^{\wedge -6}$)
	Max Tensile	Max Comp	Max Tensile	Max Comp	Max Tensile	Max Comp	Max Positive	Max Neg.	Max Positive	Max Neg.	Max Positive	Max Neg.	
0	5.7	-58	-2.8	-67	36	-28	13.5	-16.5	20	-4	20	-24	11
5	1,800	-900	2,072	-1,006	-787	-889	540	-666	322	-371	1,200	-995	-
10	27.2	-74.3	18.3	-16.1	7.7	-5.5	8.6	-4.2	4.3	-7.8	8.8	-14.2	16
15	39.6	-78	36	-20	20	-4	2.9	-8.6	9.1	-8	1.7	-8.4	16.8
20	51	-37.5	29.3	-33.9	30	-67.7	23.4	-25.6	23.5	-25.6	40.4	-29.9	23
30	84.6	-105.4	180.5	-97.6	64.8	-86.6	58.8	-72.2	64	-62.1	93.1	-81.4	-
40	36.1	-38.6	18.2	-15.9	30.1	-30.9	24.1	-16.2	15.9	-18.6	43	-39.6	22
70	9.8	-45	6.4	-29.4	18	-18.4	8.9	-9.3	16	-12.1	4.9	-17.3	20
80	19.9	-34.3	67.5	-63.4	34.9	-42.7	20.8	-11.5	13.9	-20.1	12.5	-18.1	13.1
90	12.1	-80.8	12	-28	11.9	-45.7	31	-34.4	25.5	-72.1	15.6	-24.8	14

As can be observed from the data in table 5.2, the performance of the implants was greatly deteriorated when the contact combination 2 was used in the FE analysis. This is due to the nature of the formulation of this type of contact, where the sliding between the contact surfaces is allowed but not the separation, having a direct effect on the stress distribution over the implant's structure. High values of tensile and compressive stresses were registered for several models indicating structural failure in both modes. The stress distribution in the x-axis for the 5° of angle orientation of the keel is shown in Figure 5.1, indicating the location of the failure at the screw exit on the dorsal side of the keel.

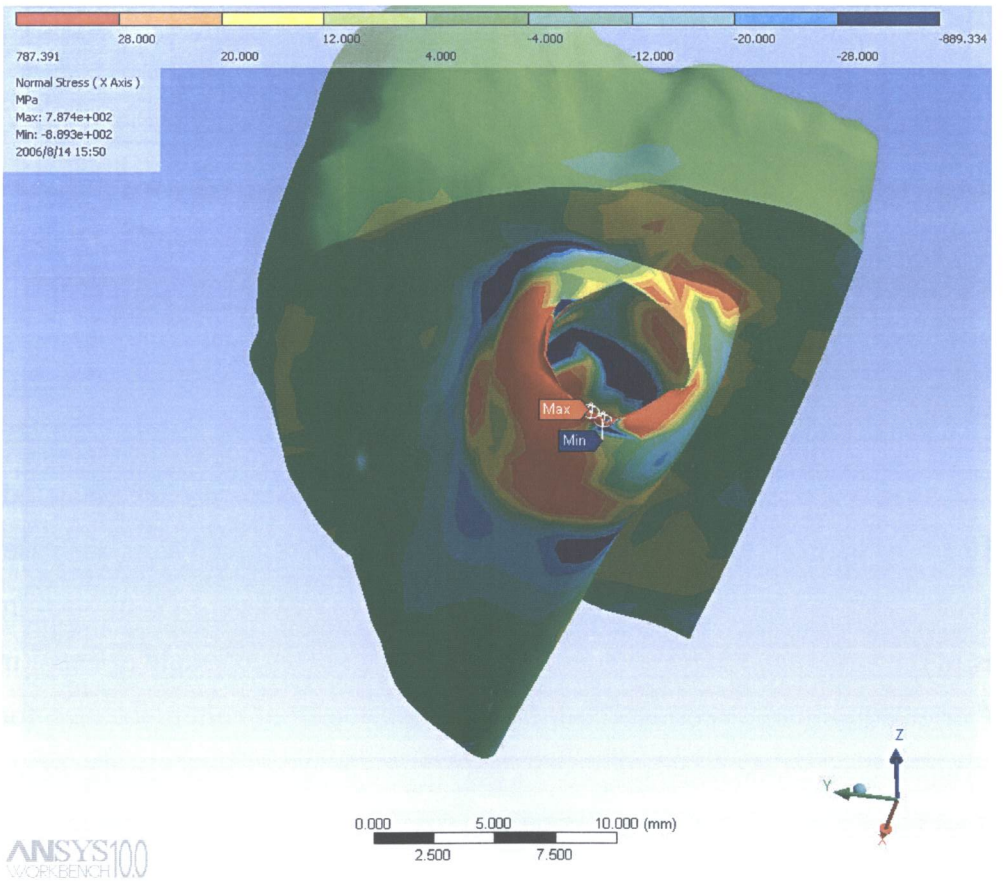

Figure 5.1 Normal stress distribution x-axis. 5o angle oriented keel. Combination 1.

The same failure location of was observed for the model with the keel oriented at 30°, as is shown in the Figure 5.2.

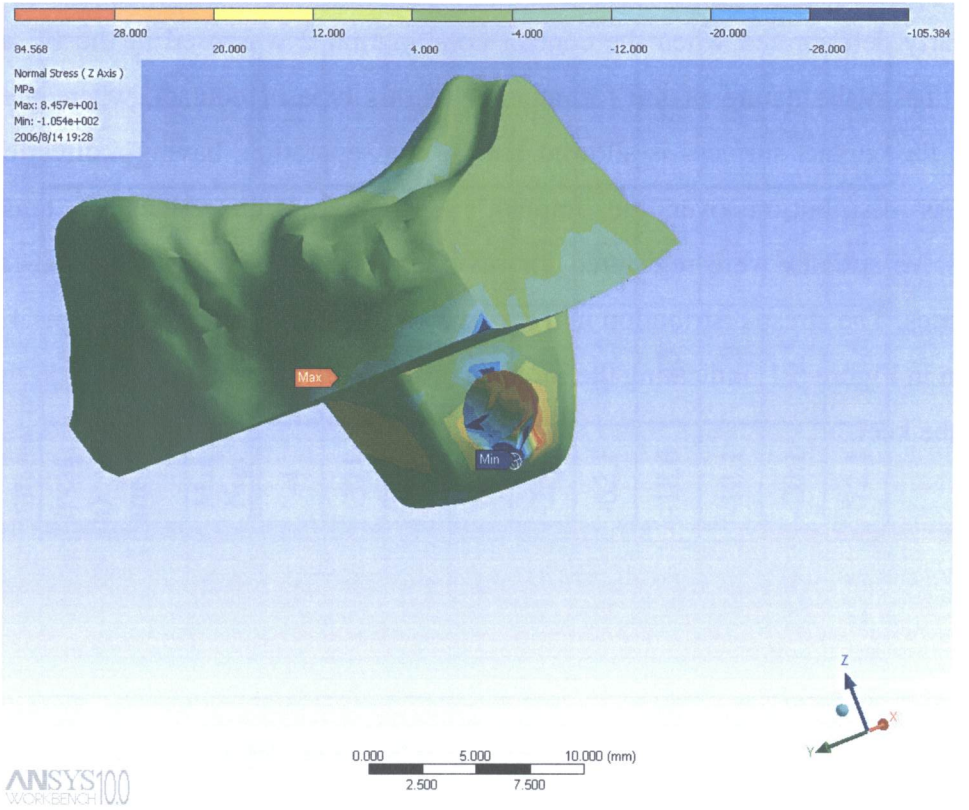

Figure 5. 2 Failure location of model with keel oriented at 30° angle. Combination 2

Figures 5.3 and 5. 4 indicate that failure for the models was encountered at the frontal part of the keel at the interface with the cortical bone, such as in the case of the 90° oriented keel and at the interface between screw head and the CPP implant interface such as in the case of 20° angle oriented keel. Similar to the 20° angle oriented implant, the 40° oriented implant experienced the same failure location. Failure location for the 0° angle oriented keel model is at the ventral part at the interface between the implant and cancellous bone.

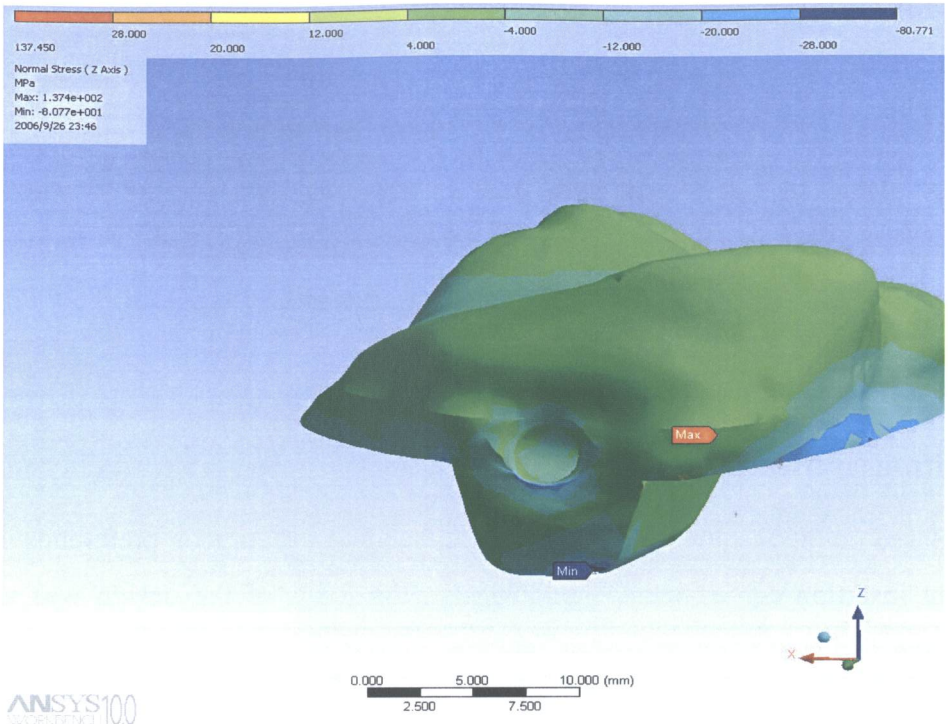

Figure 5. 3 Normal stress distribution over implant structure. 90° keel oriented model Z-axis direction. Combination 2

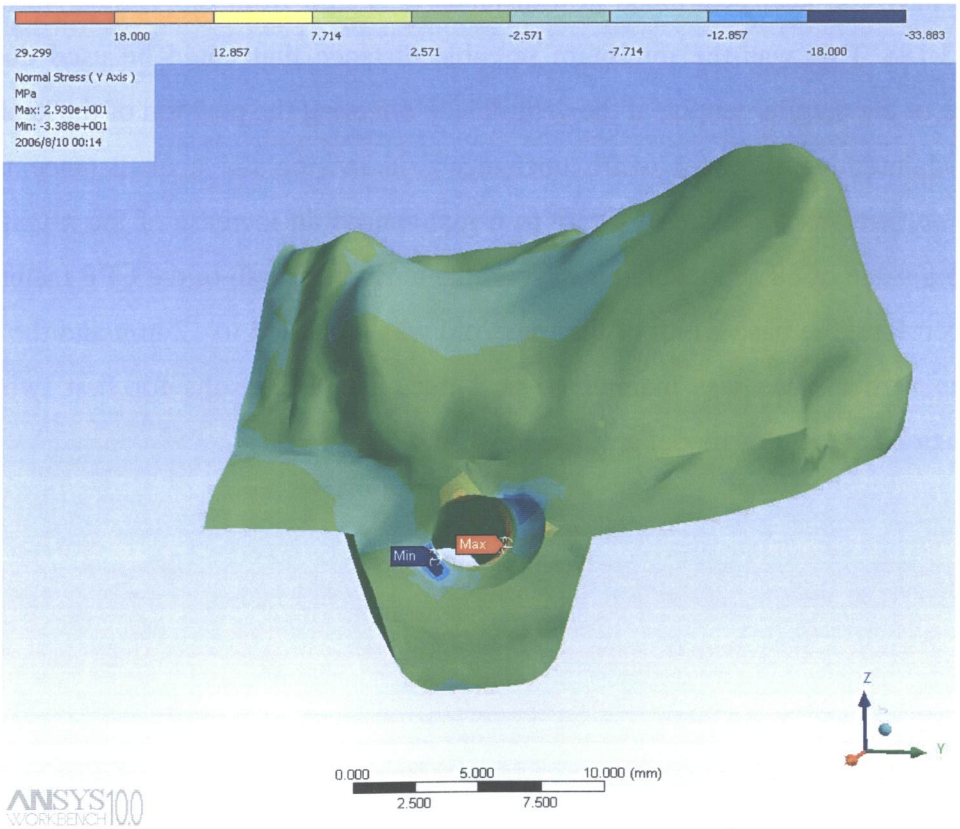

Figure 5. 4 Normal stress distribution over implant structure. 20° keel oriented model Z-axis direction. Combination 2

It can be concluded that for each of the orientations, the location of the highest stress, and consequently the location of the failure, can be uniquely related to the keel orientation itself. It can be concluded that each model, due to a combination of keel orientation, complex load applied, and complex geometrical shape of upper surface where the load is applied, contributes uniquely to the failure mode of the CPP implant structure.

5.1.2 Straight oriented keel model

Based on the results listed in 5.1 and 5. 2 and on the surgeon preference of having a implant insertion on ventral-dorsal direction, the focus of the design was shifted to improve the design of the zero keel orientation angle implant.

Keel location played a very important role in the stability of the implant structure. Implants that have a geometrical shape whose data are listed at the first row of Tables 5.1 and 5.2 have the keel positioned at a distance of 4 mm from the vertical surface (see Figure 3.18). This was the minimum possible distance that could be used due to the presence of the patellar tendon at the ventral side affecting the position of the keel.

Maintaining the keel width unchanged, increasing the keel distance from the vertical surface from a value of 4 mm to 6 mm caused an increase of the x-axis normal stress to a value of 38 Mpa which is beyond the tensile strength of the CPP material (Fig. 5.5). Therefore, the base width of the trapezoid was increased to 12 mm and the distance from the vertical face was maintained at 4 mm. The FE results for first two contact combination for the new model are listed in Table 5.3.

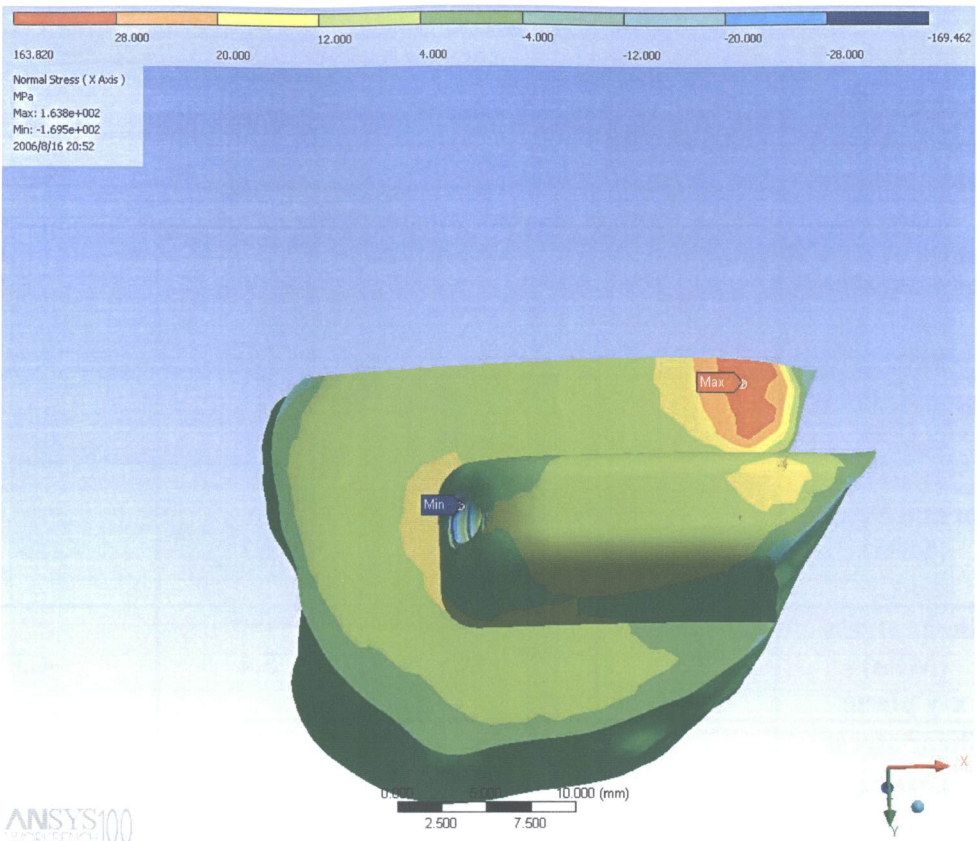

Figure 5.5 Stress distribution x-axis, keel location 6mm, keel orientation 0°. Combination 2

Table 5. 3 FE analysis results for 12 mm wide trapezoidal keel. 4 mm location

Trapezoidal cross-sectional keel with width 12mm	1st Combination		2nd Combination	
	Tensile/Positive	Compres./Negative	Tensile/Positive	Compres./Negative
Normal Stress (MPa) x-axis	**3.7**	**-11.3**	**6.9**	**-12.7**
Normal Stress (MPa) y-axis	**6**	**-7.3**	**8.7**	**-14.7**
Normal Stress (MPa) z-axis	**2.7**	**-22.9**	**9.3**	**-33**
Shear stress (MPa) x-y plane	**3.9**	**-3.6**	**5.4**	**-4.3**
Shear stress (MPa) y-z plane	**3.9**	**-5**	**4.5**	**-5.3**
Shear stress (MPa) x-z plane	**6.9**	**-5.9**	**7**	**-9.7**
Maximum Sliding Distance ($10^{\wedge-6}$)	**1**		**24**	

The increase of the size of the keel had a direct impact in the implant performance when compared with the data listed in the first row of Table 5.2. There is no presence of high compressive and tensile stresses that was found in the model with the thinner keel. The figures 5.6 and 5.7 show the normal stress distribution in the x and z directions.

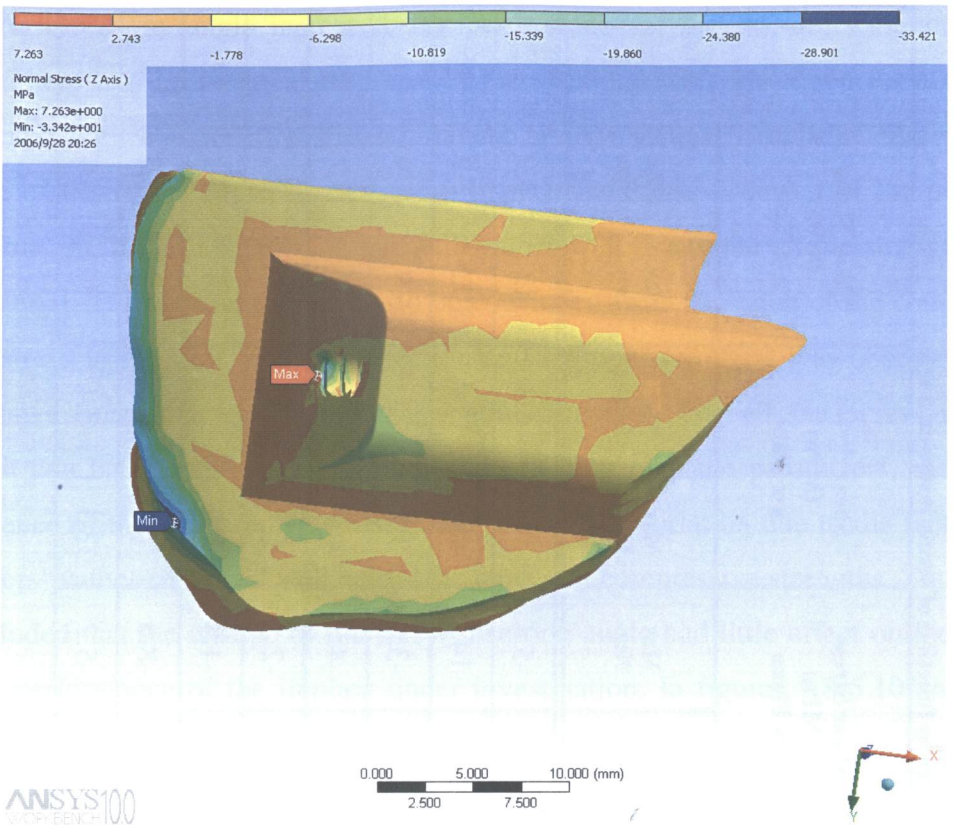

Figure 5. 6Normal stress distribution z-axis.
Trapezoid cross-section keel width 12mm .Combination 2

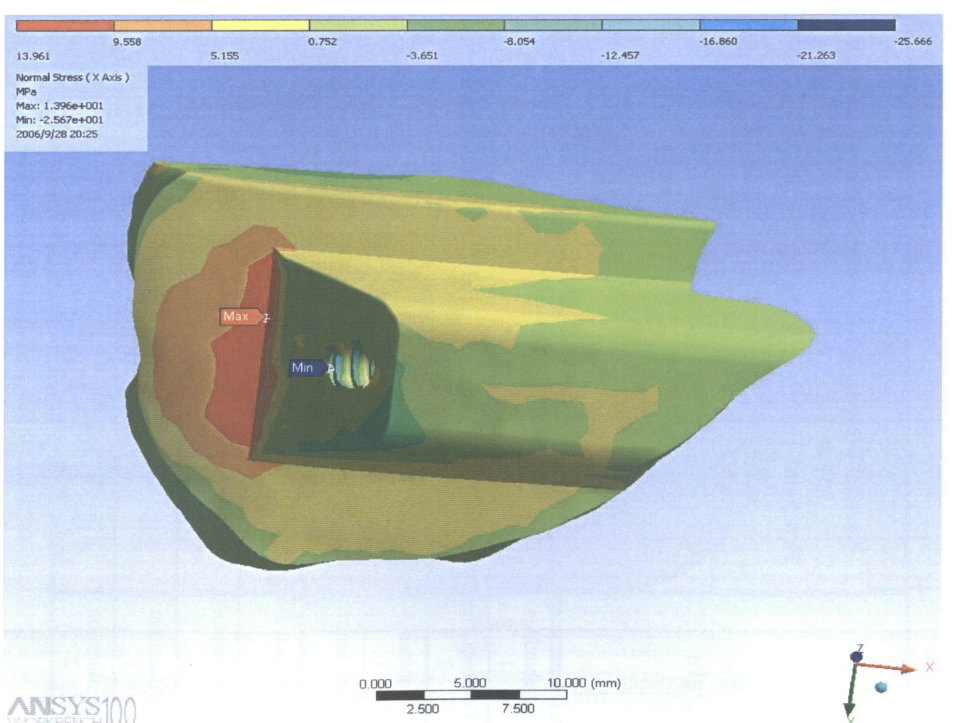

Figure 5.7 Normal stress distribution x-axis.
Trapezoid cross-section keel width 12mm .Combination 2

Table 5.4 Stress distribution over CPP implant structure as function of screw insertion angle.

Screw Angle		Normal Stress (MPa) Proximal-Distal z-axis		Normal Stress (MPa) Lateral-Medial y-axis		Normal Stress (MPa) Dorsal-Ventral x-axis		Shear Stress (MPa) x-y Plane		Shear Stress (MPa) x-z Plane		Shear Stress (MPa) z-y Plane		Sliding Distance ($10^{\wedge-6}$)
		Max Tensile	Max Comp	Max Tensile	Max Comp	Max Tensile	Max Comp	Max Pos.	Max Neg.	Max Pos.	Max Neg.	Max Pos.	Max Neg.	
5	Combination 1	3.7	-23.8	5.2	-6.5	5.6	-8.6	3	-5.4	3.7	-6.3	3.2	-4.9	1.2
	Combination 2	10.4	-33.8	10.2	-24	14.8	-23.5	5.3	-14.7	4.6	-11.4	10.5	-8.2	16
10	Combination 1	2.7	-22.9	6	-7.3	3.7	-11.3	3.9	-3.6	3.9	-5	6.9	-5.9	1
	Combination 2	9.3	-33	8.7	-14.7	6.9	-12.7	5.4	-4.3	4.5	-5.3	7	-9.7	24
15	Combination 1	2	-22.2	5.6	-7.5	9.2	-13.2	2.7	-2.5	5.3	-8	6.9	-7.8	1
	Combination 2	7.3	-33.4	12.6	-11.1	13.9	-25.7	4.5	-4.9	7.5	-17.1	8.4	-6.2	16
20	Combination 1	3.4	-23	6	-6	6	-14	6.7	-8.6	8	-11.8	6.2	-9.5	1
	Combination 2	4.6	-33.3	9.9	-9.9	9.4	-18.8	4.2	-5.2	13.1	-7.4	8	-5.4	23

As the screw angle increased, the performance of the implant was not greatly altered. There was an identical response in the proximal-distal direction for all models investigated with compressive stresses having similar values. It appears that with the decrease of the screw angle an increase in the tensile stress occurred in the proximal-distal direction, for combination 2, but with values well below the tensile strength of the CPP material. The same observation can be concluded from the value of the compressive normal stress in the lateral-medial direction and the opposite trend was observed in the compressive normal stresses in dorsal-ventral direction. For all the screw insertion angles, it can be concluded that, despite the variation of some parameters, the overall performance of the CPP implant was unaffected by this variation due to the fact that all parameters' values remained well below the tensile or compressive strengths. Thus, it can be concluded that the change of the screw insertion angle had little effect on the overall stability performance of the implant under investigation. In figures 5.8-5.10 are shown some of the most significant stress distribution for various models.

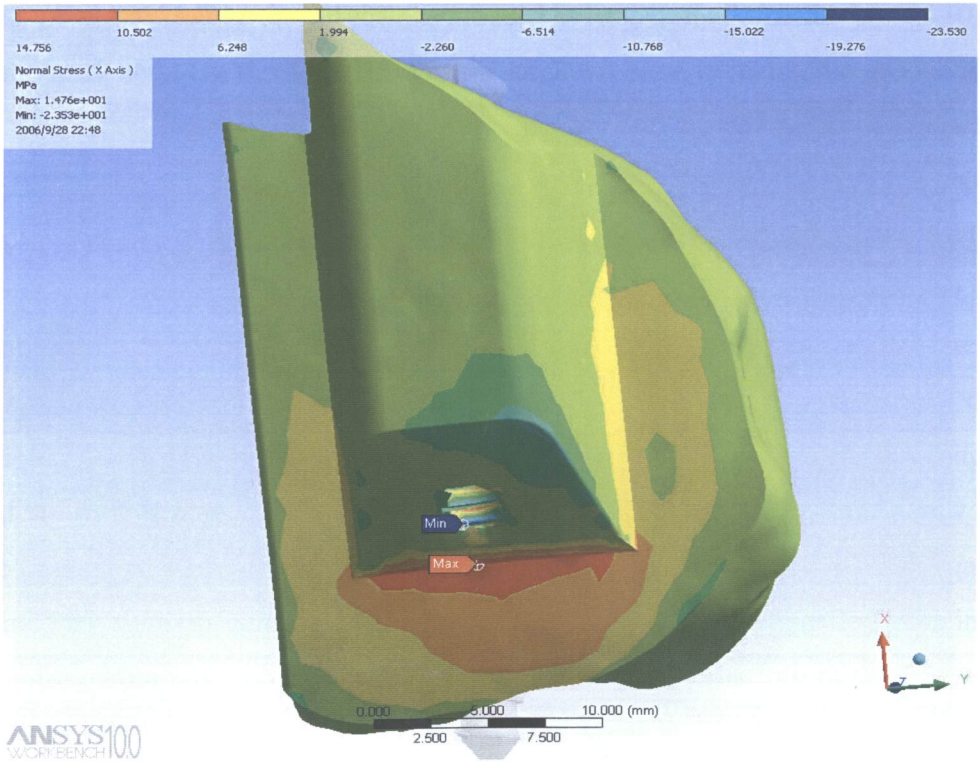

Figure 5.8Normal stress distribution over implant structure. Combination 2 Keel located 4 mm from vertical face. Screw angle insertion 5°. 12 mm keel

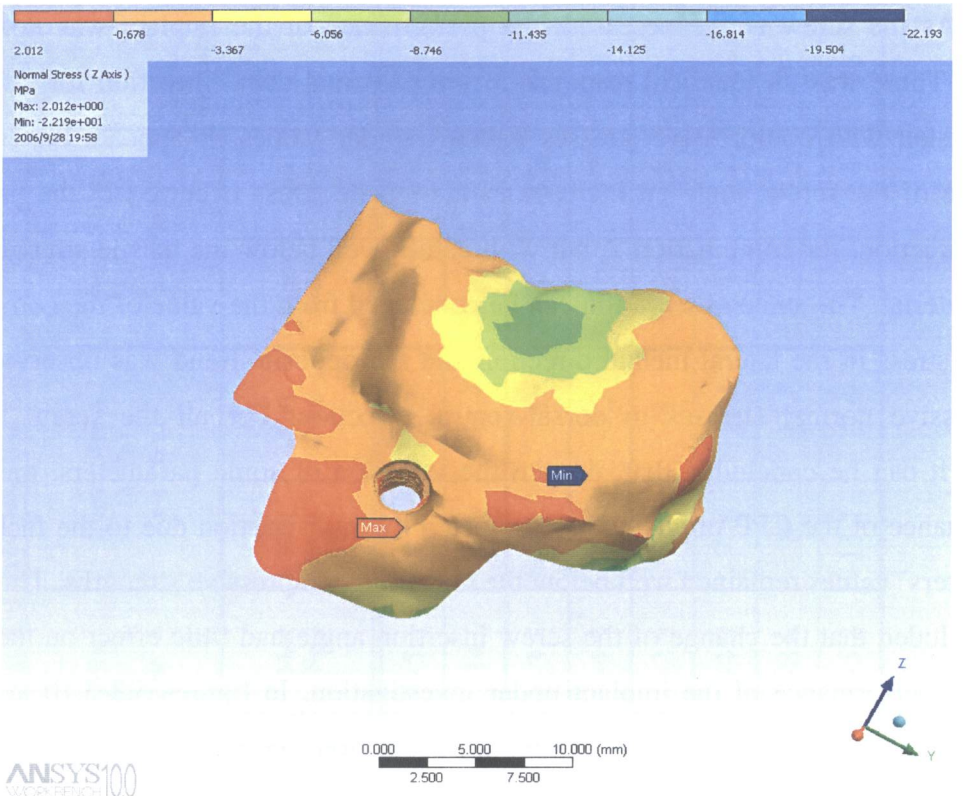

Figure 5.9 Normal stress distribution over implant structure. Combination 2 Keel located 4 mm from vertical face. Screw angle insertion 15°. 12 mm keel

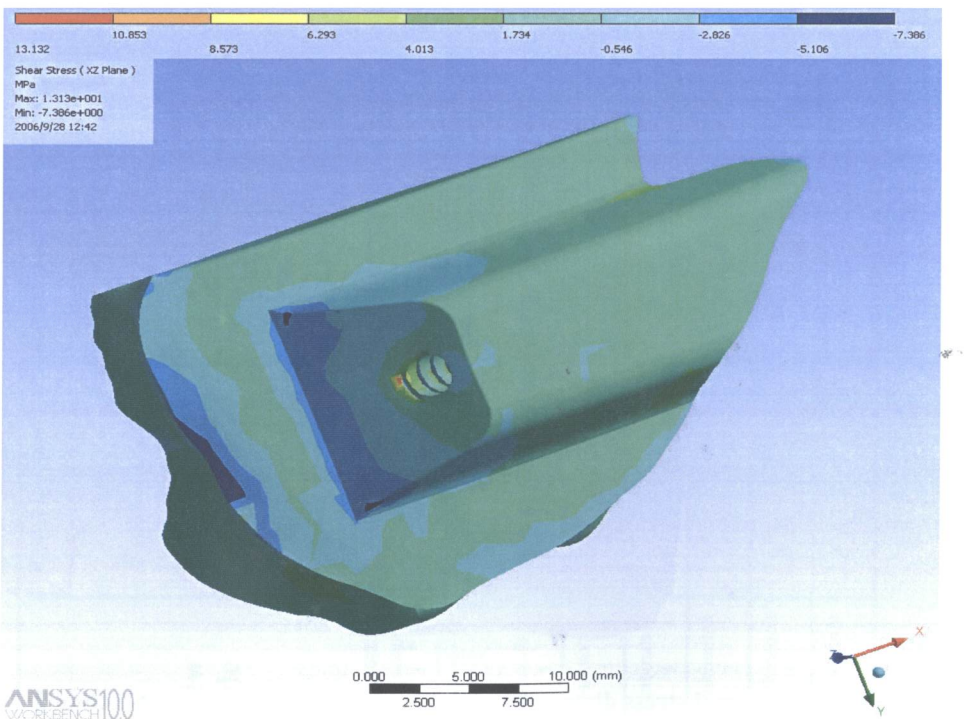

Figure 5.10 Shear stress distribution over implant structure. Combination 2 Keel located 4 mm from vertical face. Screw angle insertion 20°. 12 mm keel

`5.2 Implant Design: Comparative Stage with Semi-Circular Cross Section Keel.

In this section, the focus of the analysis is the design of the implant based on e determining the optimal shape of the implant by trying to minimize the amount of the removed bone while ensuring a stable and strong implant structure. Determination of the optimal design was achieved by the investigation of the effect of several factors: keel length and associated screw angle for various keel sizes (Section 5.2.1), keel width (Section 5.2.2), screw insertion force (Section 5.2.3), and the possibility of the use of a biodegradable screw (Section 5.2.4).

5.2.1 Effect of keel width and screw angle insertion

As seen in the Section 5.1, the keel width made a large difference in the resulting stresses, for the trapezoidal cross section keel. To determine whether a similar trend held for keels of semi-circular cross section, models having keel diameters of 12, 10, and 8 mm, were analyzed. On the dorsal end of the keel, to properly match the groove left by a simple vertical movement of a drill bit by the surgeon, a half cone was attached, to imitate the drill bit tip shape. The length of the implant's keel was adjusted according to the screw angle insertion. For screw angles of 10, 15, and 20°, the keel length was adjusted so that the screw hole exited in the conical part of the keel, resulting in keel lengths of 20.5, 17.5, and 13.5 mm, respectively. Note that this keel length corresponds to the maximum length of the keel; i.e. the distance from the most ventral part of the keel to the tip of the half cone in the dorsal position. A variation of 2° in the screw angle was allowed, for each of the angles considered in the analysis, to ensure that the screw did not exit the implant on the horizontal surface or within the keel cylinder. Failure conditions are created by such an exit, as shown in Figure 5.11, where the tensile stress in the X direction (maximum of 45 MPa) greatly exceeded the tensile strength of the CPP ceramic material (28 MPa). Figure 5.12 shows the state of shear stress in the X-Z plane. For the situation shown in the mentioned figures the contact condition 1 (from Table 4.6) was used in the solution of the FE model.

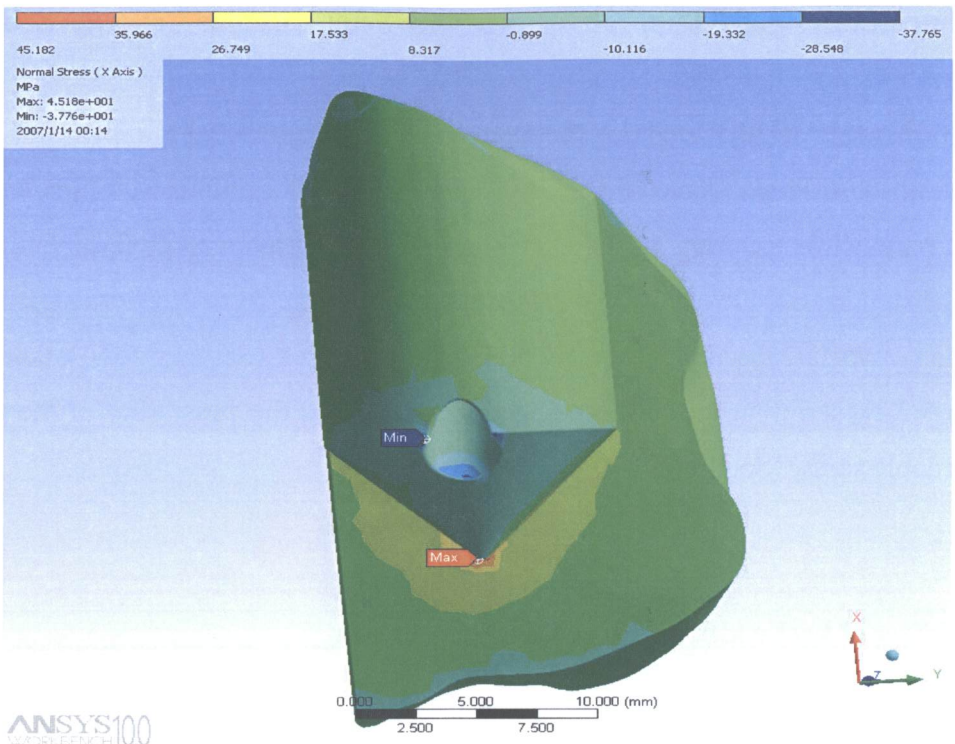

Figure 5.11 Normal stresses in x direction for screw exiting in cylindrical portion of keel. Screw insertion angle 20°, keel length of 17.55mm

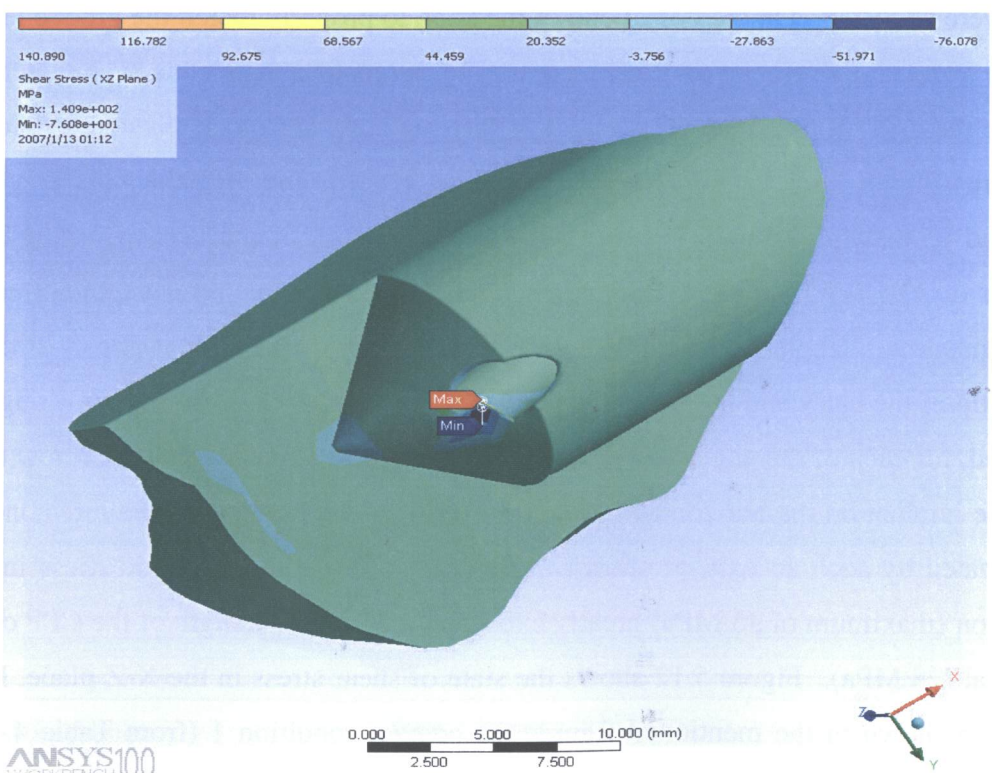

Figure 5.12 Shear stress in x-y direction for screw exiting the cylindrical portion of the keel. Screw insertion angle 20°, keel length of 17.55mm.

Table 5.5 Performance of the implant with a keel diameter of 12 mm.

Keel Diameter 12 mm	Keel Length 13.5 mm Screw Insertion Angle 20°				Keel Length 17.5 mm Screw Insertion Angle 15°				Keel Length 20.5 mm Screw Insertion Angle 10°			
	Contact Combination 1		Contact Combination 2		Contact Combination 1		Contact Combination 2		Contact Combination 1		Contact Combination 2	
	Tensile/ Positive	Comp/ Negative	Tensile/ Positive	Comp/ Negative	Tensile/ Positive	Comp/ Negative	Tensile/ Positive	Comp/ Negative	Tensile/ Positive	Comp/ Negative	Tensile/ Positive	Comp/ Negative
Normal Stress (MPa) X-axis	5.1	-10.6	27.1	-23.4	20	-38.1	43	-38.7	8.2	-11.9	22.6	-12.5
Normal Stress (MPa) Y-axis	12	-8.7	18.9	-35.7	21.8	-9.6	26.6	-25.4	8.6	-12.6	12.1	-21.8
Normal Stress (MPa) Z-axis	4.9	-28.4	6.3	-53.8	18.7	-19.4	39.5	-23.4	8.3	-32	13.7	-49.8
Shear Stress (MPa) X-Y plane	2.8	-3.5	7.6	-8	6.3	-12.1	8.4	-10.8	4.4	-4.1	8.9	-5.1
Shear Stress (MPa) Y-Z plane	6.3	-4.8	11.3	-7.8	5.9	-5.3	11.8	-6.4	8.4	-7	13.1	-9.3
Shear Stress (MPa) X-Z plane	4.1	-8	12.4	-17.3	15.4	-5.1	8	-14.3	5.6	-11.23	5.7	-15.1
Maximal Sliding distance ($10^{\wedge-6}$)	23		42		12		30		6		25	
Safety Factor Tensile Stress theory	1.86		0.8		0.8		0.5		2.4		0.98	

Table 5.5 summarizes the FE results for the implant with a keel diameter of 12 mm, using three different lengths and associated screw insertion angles. The best performer from this group of models was the model with the keel length of 20.5 mm (the longest keel) and with an associated screw insertion angle of 10^{o}.

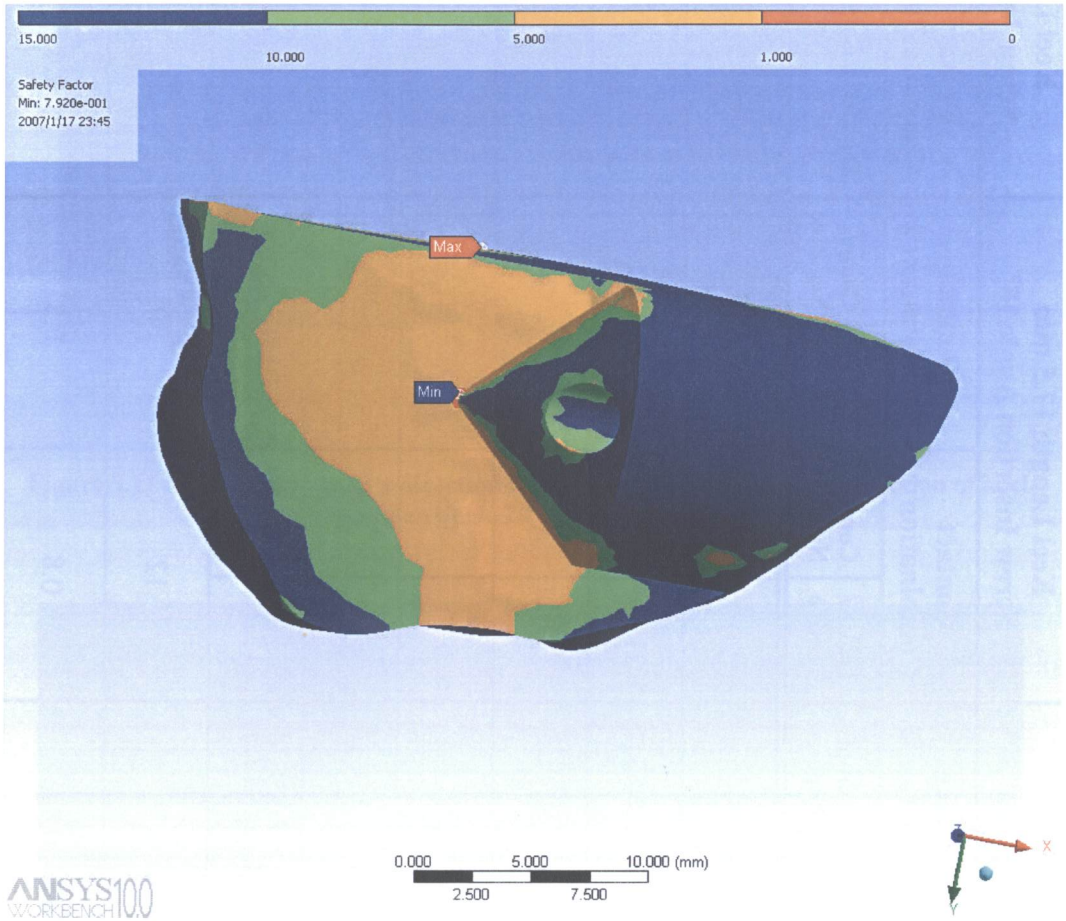

Figure 5.13 Safety factor (Maximum Tensile Stress theory), using contact combination 1. Keel diameter of 12mm and keel length of 13.5mm.

Figure 5.13 shows the safety factor (i.e. ratio of maximum stress to failure stress) based on the Maximum Tensile Stress theory, distribution over the implant structure. The location of the minimum is at the tip of the conical part of the keel.

Figures 5.14 and 5.15 show the safety factor and Y direction normal stress distributions for the implant with a keel length of 17.5 mm.

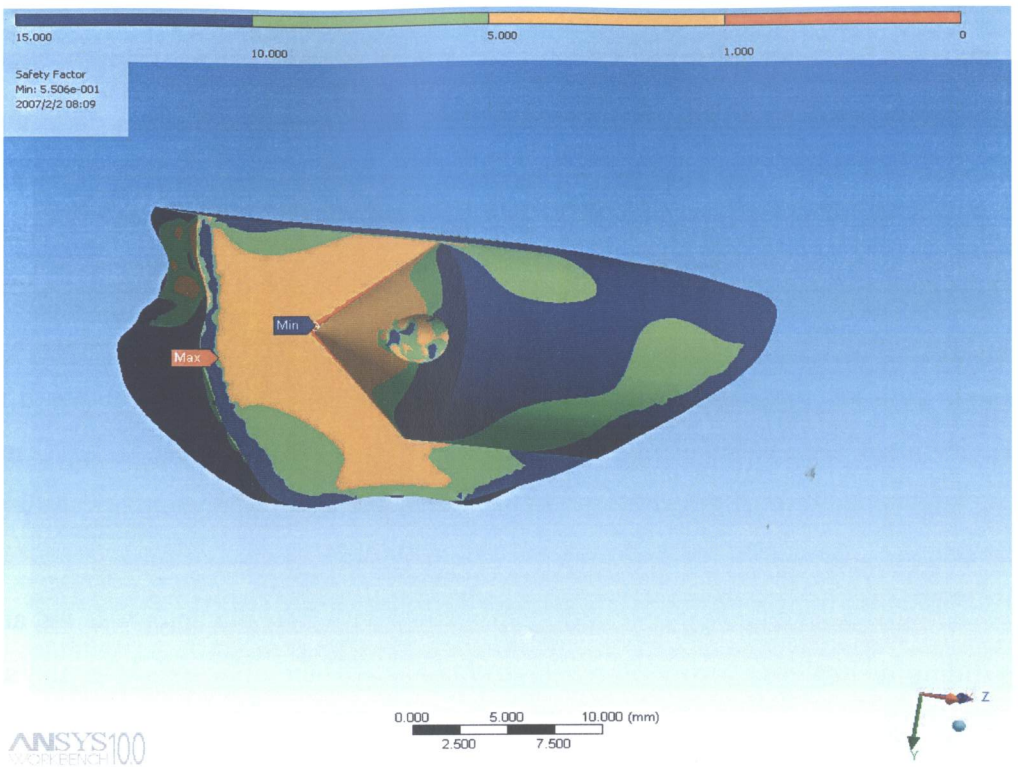

Figure 5.14 Safety factor (Maximum Tensile theory) using contact combination 2. Keel diameter of 12mm and keel length of 17.5 mm.

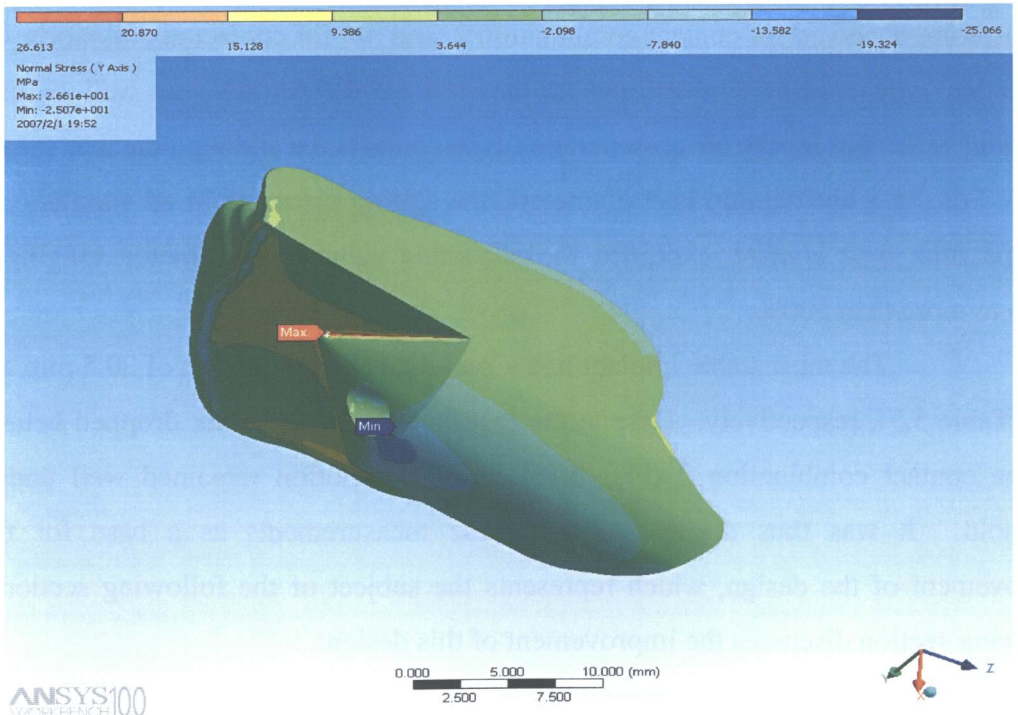

Figure 5.15 Normal stress in Y direction using contact combination 2. Keel diameter of 12mm and keel length of 17.5 mm.

The results listed in Table 5.5 suggest that an increase in keel length does not guarantee an increase in the structural bulk strength. For example, while the implant with keel length of 13.5 mm experiences an increase in overall normal tensile stresses in all directions, the implant with keel length of 17.55 mm concentrations of high stress are observed along the keel's dorsal side near the level of horizontal surface as shown in Figures 5.14 and 5.15. The same conclusion can be reached by examining the result for the models with keel diameters of 8 and 10 mm (Tables 5.6 and 5.7). Compared to the model with a keel diameter of 12 mm (Table 5.5), the 8 and 10 mm diameter models result in very similar tensile stress distributions, reflected in the similar safety factor values.

The only parameter that changed significantly with keel diameter was the amount of the sliding distance occurring along the implant's contact. For example, the sliding distance for the implant with 10 mm keel diameter increases from the model with keel diameter 12 mm by an amount of 640 %. The same increase in sliding distance is experienced by the implant with keel diameter 8 mm which the increase is 690 %. These increases are observed for contact combination 2, and not for contact combination 1. For all-bonded type contact simulations, the amount of the sliding was well within the threshold value, but for the all-no-separation type contacts the sliding increased greatly.

For the 8 and 10 mm keel diameters, the sliding distances in all simulations, for no-separation type contact, exceeded the allowable value by an amount ranging from 200% to more than 500%.

The most stable implant had a keel diameter and length of 20.5 mm and 12 mm (Table 5.5), respectively. Despite the fact that the safety factor dropped below one for the contact combination 2 (Fig. 5.16), the micromotion remained well under the threshold. It was thus decided to use these measurements as a base for further improvement of the design, which represents the subject of the following section. The following section discusses the improvement of this design.

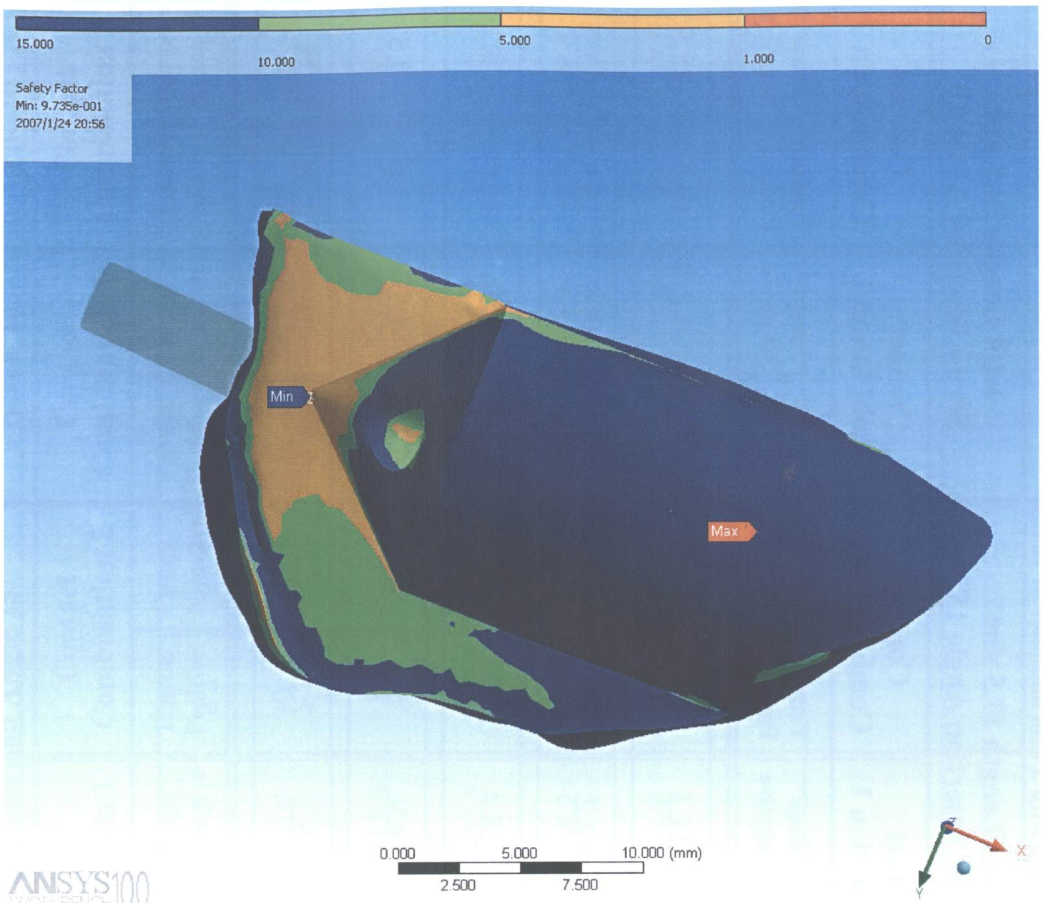

Figure 5.16 Safety factor (Maximum Tensile theory). Diameter 12mm. Length 20.5 mm. Combination 2.

Table 5.6 Performance of the implant with a keel diameter of 10 mm.

Keel Diameter 10 mm	Keel Length 13.5 mm Screw Insertion Angle 20°				Keel Length 17.5 mm Screw Insertion Angle 15°				Keel Length 20.5 mm Screw Insertion Angle 10°			
	Contact Combination 1		Contact Combination 2		Contact Combination 1		Contact Combination 2		Contact Combination 1		Contact Combination 2	
	Tensile/ Positive	Comp/ Negative	Tensile/ Positive	Comp/ Negative	Tensile/ Positive	Comp/ Negative	Tensile/ Positive	Comp/ Negative	Tensile/ Positive	Comp/ Negative	Tensile/ Positive	Comp/ Negative
Normal Stress (MPa) X-axis	14.5	-11.6	37.8	-14.8	16.2	-11.1	39	-15	7.1	-9.5	19.4	-25.5
Normal Stress (MPa) Y-axis	12	-10	18.1	-19.6	17.3	-9.2	19.5	-15.6	9.4	-15.6	13.9	-63.9
Normal Stress (MPa) Z-axis	8.9	-28.1	25.4	-36.1	11.7	-28.4	30.2	-38.9	2.1	-19.9	15.6	-28.9
Shear Stress (MPa) X-Y plane	3.7	-4.4	7	-6.9	4.9	-4.9	5	-5.2	6.4	-4.5	11.6	-9.5
Shear Stress (MPa) Y-Z plane	6.8	-4.5	6.6	-9	9.1	-5.1	7.1	-6.4	7.9	-10	21.8	-25
Shear Stress (MPa) X-Z plane	5	-7	10.4	-15.9	5.4	-6.6	5.7	-17.6	3.6	-4.6	6.3	-12.8
Maximal Sliding distance (μm)	23		243		20		223		22		102	
Safety Factor Tensile Stress theory	1.54		0.57		1.3		0.52		2.4		0.86	

Table 5.7 Performance of the implant with a keel diameter of 8 mm.

Keel Diameter 8 mm	Keel Length 13.5 mm Screw Insertion Angle 20°				Keel Length 17.5 mm Screw Insertion Angle 15°				Keel Length 20.5 mm Screw Insertion Angle 10°			
	Contact Combination 1		Contact Combination 2		Contact Combination 1		Contact Combination 2		Contact Combination 1		Contact Combination 2	
	Tensile/ Positive	Comp/ Negative	Tensile/ Positive	Comp/ Negative	Tensile/ Positive	Comp/ Negative	Tensile/ Positive	Comp/ Negative	Tensile/ Positive	Comp/ Negative	Tensile/ Positive	Comp/ Negative
Normal Stress (MPa) X-axis	11.9	-18.2	40.1	-15.6	14.2	-6.9	39.5	-13.8	12.1	-11.6	29.1	-23.9
Normal Stress (MPa) Y-axis	18.9	-14	15.6	-16	13.9	-13.5	15	-19.3	13.2	-13	13.6	-39.5
Normal Stress (MPa) Z-axis	9.9	-26.3	23.9	-44.6	16.2	-32.5	33.5	-37.6	4.2	-31.1	19	-53
Shear Stress (MPa) X-Y plane	5.6	-6.3	5	-9.6	7	-8.2	4.6	-6.1	3.9	-3.8	7.5	-9.5
Shear Stress (MPa) Y-Z plane	4.9	-8	9.6	-12.3	9.5	-6.6	9.8	-8.9	7.6	-7.6	15	-17.6
Shear Stress (MPa) X-Z plane	12.2	-4.3	8.7	-19.3	6.1	-5.2	6	-16.3	4.7	-12	7.6	-16
Maximal Sliding distance (μm)	51		265		44		165		32		85	
Safety Factor Tensile Stress theory	1.1		0.57		1.1		0.42		1.56		0.7	

5.2.2 Modified implant: Final Modelling Stage.

Investigation of the implant structure behavior in the initial phase just after the insertion into the host bone represents a very important step in determining the effectiveness of the design. In the previous comparative modeling stages, only the first two contact combinations listed in Table 4.6 were used to establish the best overall geometrical shape (i.e., keel size, location, shape, etc) for the implant . During these preliminary analyses, the types of contact considered were glued (bonded) and sliding without contact separation (no-separation). These linear analyses allowed a fast and reasonably reliable confidence in the accuracy of the solution, which was important considering the large number of models that were considered.

To have a more complete picture of the performance of the selected design, and to simulate the contact conditions which the implant would encounter immediately after its insertion, the use of a frictionless type contact is more appropriate. By imposing into the assembly this type of contact, the system of equations describing the FE model becomes nonlinear, due to the fact that not only sliding but contact separation is allowed. As explained in Section 4.4.1, because the friction coefficient of the CPP material when in contact with cortical and cancellous bone has never been measured, a worst case frictionless condition was assumed. For the case of the contact between the bone and fixation screw, a similar problem arose, and the coefficient of friction was approximated by the value for contact between titanium with wood (i.e., 0.3).

Using frictionless contact conditions with the implant having the base geometry as determined from Section 5.2.1 (i.e., the most promising design, having a keel diameter and length of 20.5 mm and 12 mm, respectively) resulted in non convergence of the solution. This was due to the sharp corner at the tip of the conical shaped dorsal part of the keel (see Figure 3.19). Therefore, as discussed in Section 3.2, a modification to the dorsal side of the keel was made which not only ensured the convergence of the nonlinear contact problem, but also resulted in a slight improvement in the performance of the structure. In this modified model (Fig. 3.21), the sharp corner was eliminated, and the model converged for the frictionless contact case.

A summary of the results for the modified models is shown in Tables 5.8 and 5.10 for all contact combinations listed in Table 4.6.

Table 5.8 Stress results for the modified CPP implant. Combination of contact conditions from Table 4.6.

Modified Model		Combination 1	Combination 2	Combination 3	Combination 4	Combination 5	Combination 6	Combination 7
Normal Stress (MPa) X-Axis	Tension	7.7	19	19.2	5.2	5.2	14.8	17.2
	Compression	-7.5	-10.9	-18.1	-10.1	-10	-45.2	-60
Normal Stress (MPa) Y-Axis	Tension	6	11.9	18.9	8	8.1	8.3	9.1
	Compression	-14.4	-29.8	-25.3	-7.9	-7.9	-61.4	-66.2
Normal Stress (MPa) Z-Axis	Tension	3.6	11.4	14.2	4	3.6	9	12.8
	Compression	-27.4	-39.9	-24.1	-19.9	-20	-46.3	-41.3
Shear Stress (MPa) XY-Plane	Positive	3.9	6.8	7.9	3.9	3.9	14.2	11.9
	Negative	-3.6	-5.7	-8.9	-5.3	-5.1	-11.7	-11.9
Normal Stress (MPa) YZ-Plane	Positive	10.5	17.8	16.8	10.3	10.4	21.8	24.3
	Negative	-5.2	-6.8	-12..5	-5.7	-5.8	-18.3	-22.3
Normal Stress (MPa) XZ-Plane	Positive	5.4	6.8	9.4	7.6	7.7	8.4	7.8
	Negative	-7.8	-12.2	-16.2	-9.6	-8.8	-13.5	-15.9
Safety Factor	Max. Tensile	3.1	1.2	1.1	2.91	2.9	1.45	1.1
	Shear Stress	1	0.64	0.75	1	1	0.58	0.4
	Mohr-Coulomb	1.8	1.1	0.86	1.8	1.8	0.95	0.83

Table 5.9 Strain results for the modified CPP implant. Combination of contact conditions from Table 4.6.

		Combination 1	Combination 2	Combination 3	Combination 4	Combination 5	Combination 6	Combination 7
Normal Strain 10^{-3} X-Axis	Maximum	1.2	2.7	3.1	1.3	1.3	2.5	2.6
	Minimum	-0.8	-1	-2.1	-1.5	-1.5	-5.7	-8.4
Normal Strain 10^{-3} Y-Axis	Maximum	0.8	1.6	2.4	2	2	3	2.7
	Minimum	-0.8	-3	-3.7	-0.8	-0.8	-9.6	-10.7
Normal Strain 10^{-3} Z-Axis	Maximum	0.6	1.4	1.9	0.7	0.4	0.6	3.2
	Minimum	-4.1	-5.6	-3.9	-3.2	-3.3	-4.3	-5.5
Shear Strain 10^{-3} XY-Plane	Maximum	1.8	3.1	3.6	1.7	1.7	6.3	5.3
	Minimum	-1.6	-2.5	-4	-2.4	-2.3	-5.2	-5.3
Normal Stress 10^{-3} YZ-Plane	Maximum	4.7	8	7.5	4.6	4.6	9.7	10.9
	Minimum	-2.3	-3.1	-5.6	-2.6	-2.6	-8.2	-10
Normal Stress 10^{-3} XZ-Plane	Maximum	2.4	3.1	4.2	3.4	3.4	3.8	3.5
	Minimum	-3.5	-5.5	-7.3	-4.3	-4	-6	-7.1

Figures 5.17-5.27 show the most important results obtained from the FE analysis for the various contact conditions. As discussed in Section 4.4, the contact combinations are meant to represent different time periods, and bone ingrowth, after implant insertion. In contact combinations 1 and 2, the screw contact with the implant was considered bonded, due to the presence of the screw threads, while in the other simulations this was considered non-bonded. Combinations 1 and 4, and 6 and 7 describe two extreme cases. Combinations 1 and 4 describe the contact conditions after an initial six week time period, where the bone ingrowth process is well under way. Combinations 6 and 7, on the other hand, describe the time period immediately after implant insertion, when there is little bone ingrowth. The remaining combinations describe different time periods after the insertion, where it has also been noted (combination 5) that the cancellous bone, being more vascular, would likely display earlier ingrowth into the CPP, compared to the cortical bone.

Keeping in mind that the analysis was extremely conservative, due to the large applied distributed load (see Section 4.2), the ultimate aim of the design was to obtain stress and strain safety factors (i.e. ratio of stress or strain to critical stress or strain for failure) as close as possible to one. When using contact combinations 1, and 2 compared to the unmodified implant (Table 5.5), the modified implant resulted in lower stresses. For example, the maximum z-direction stress was reduced from 49.8 MPa (Compression) in the previous model to 39.9 MPa in the modified model. Moreover, the stress concentration observed at the tip of the keel on the dorsal side was eliminated with the new design. The sliding distance for both models remained approximately the same, at 34 % below the threshold value of 50 μm for both models.

For the contact combinations involving frictionless contact between implant and the bone (combinations 6 and 7, shown in Figures 5.23-5.27), representing the early stages after the surgery, the implant was as expected, less stable than in the bonded contact cases combinations 2 and 5 are shown in Figures 5.17 and 5.18. For example, the maximum sliding distance at the implant interface increased by 2000%, and the maximum stress in the y direction increased by 360 % when contact combination 7 (frictionless) was compared to contact combination 1 (bonded).

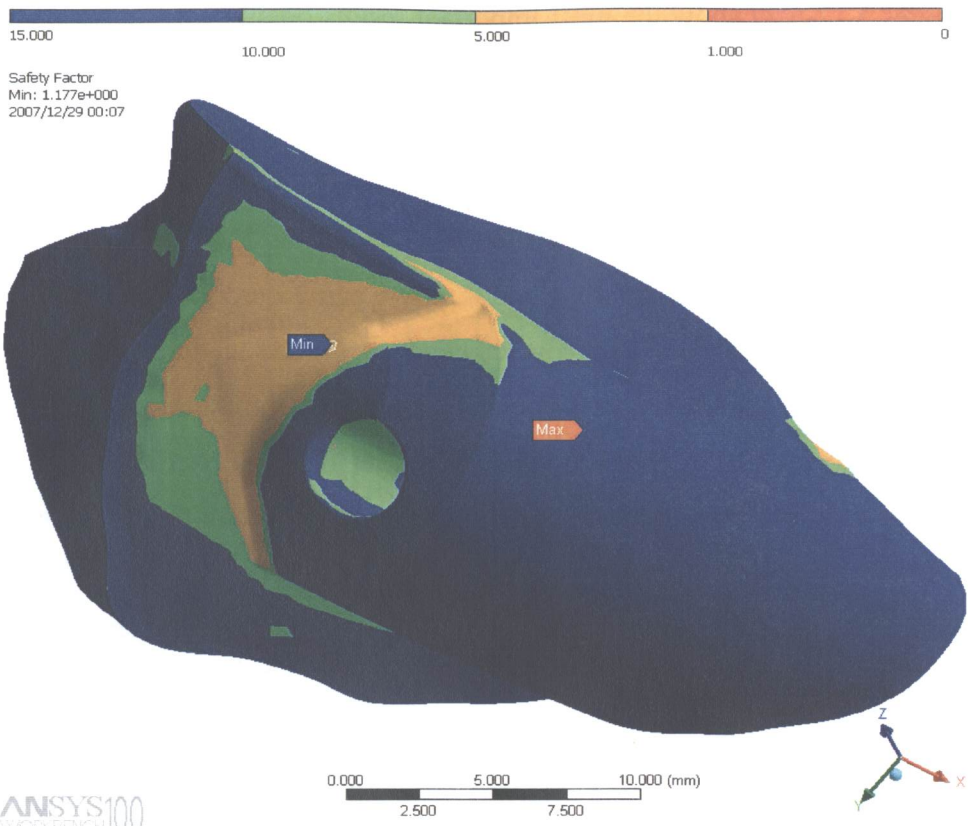

Figure 5.17 Safety Factor (Modified Model Using Tensile Stress Theory) Combination 2.

Table 5.10 Sliding distances. Titanium fixation screw

Implant Contact Combinations From Table 4.6	Maximum Sliding Distances (μm)
1	2
2	32
3	37
4	3
5	2
6	156
7	213

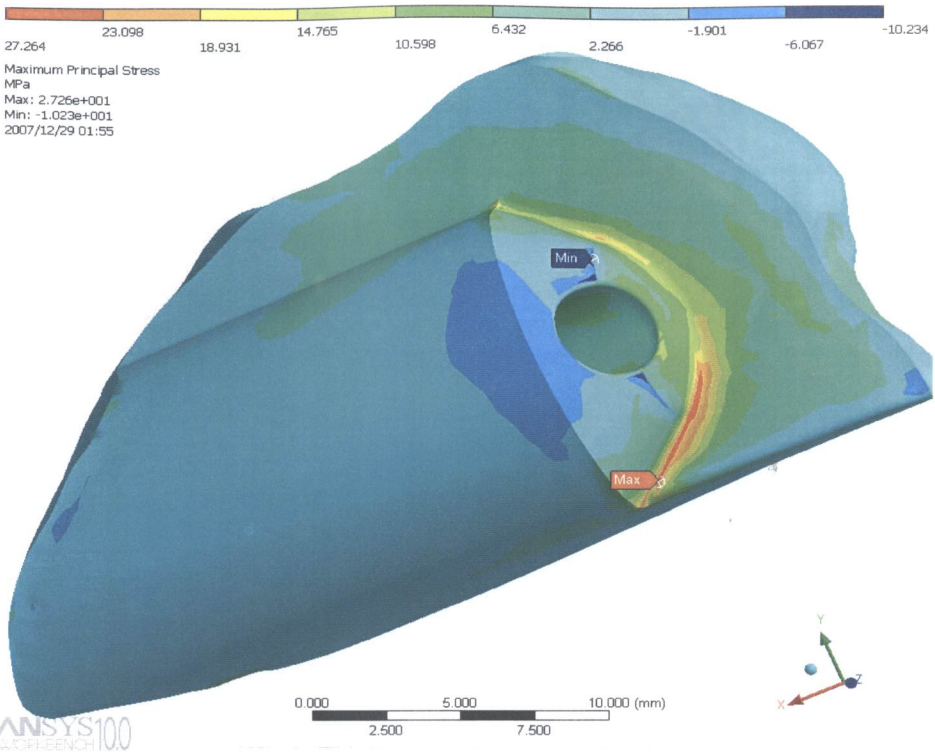

Figure 5.18 Maximum principal stresses. CPP implant. Combination 3

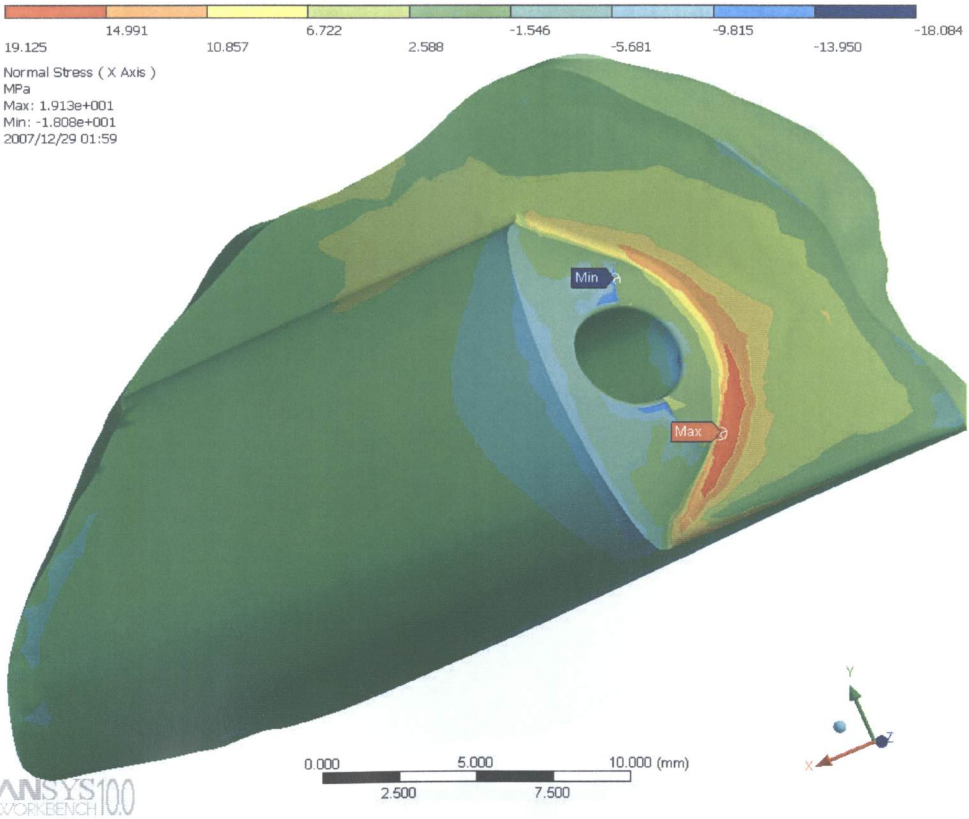

Figure 5.19 Stress distribution X-axis. CPP Implant. Combination 3

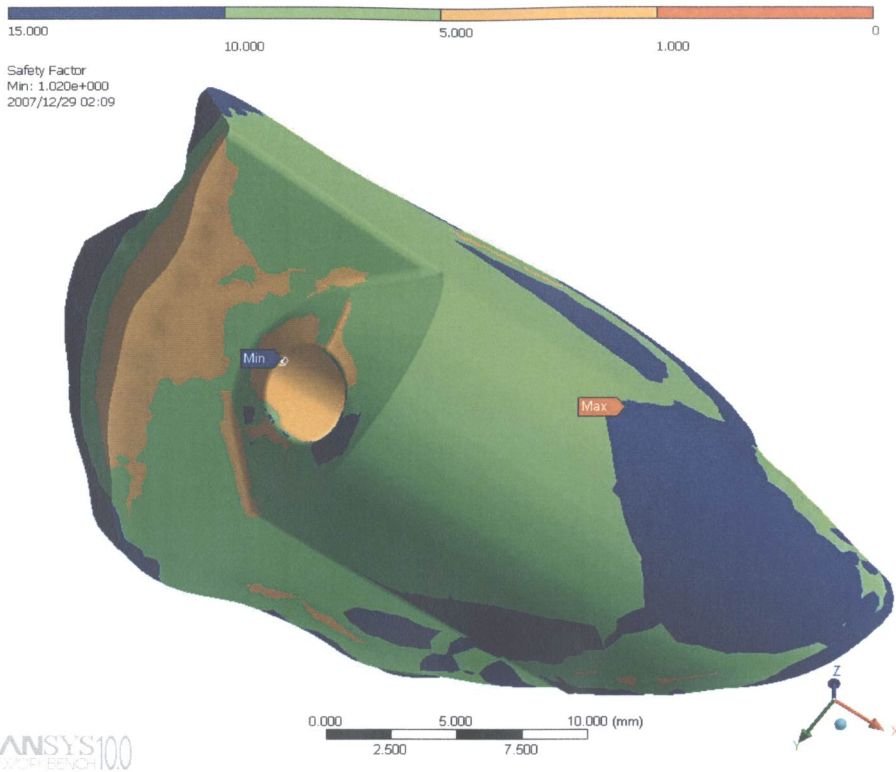

Figure 5.20 Shear factor distribution. CPP Implant. Combination 5

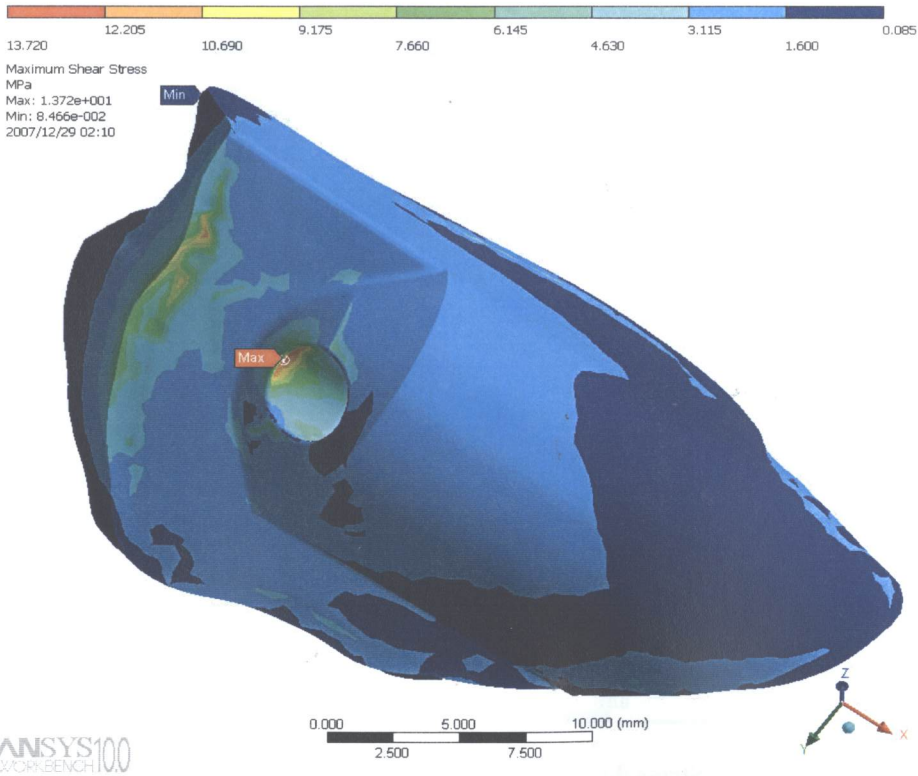

Figure 5.21 Maximum shear stress. CPP Implant. Combination 5

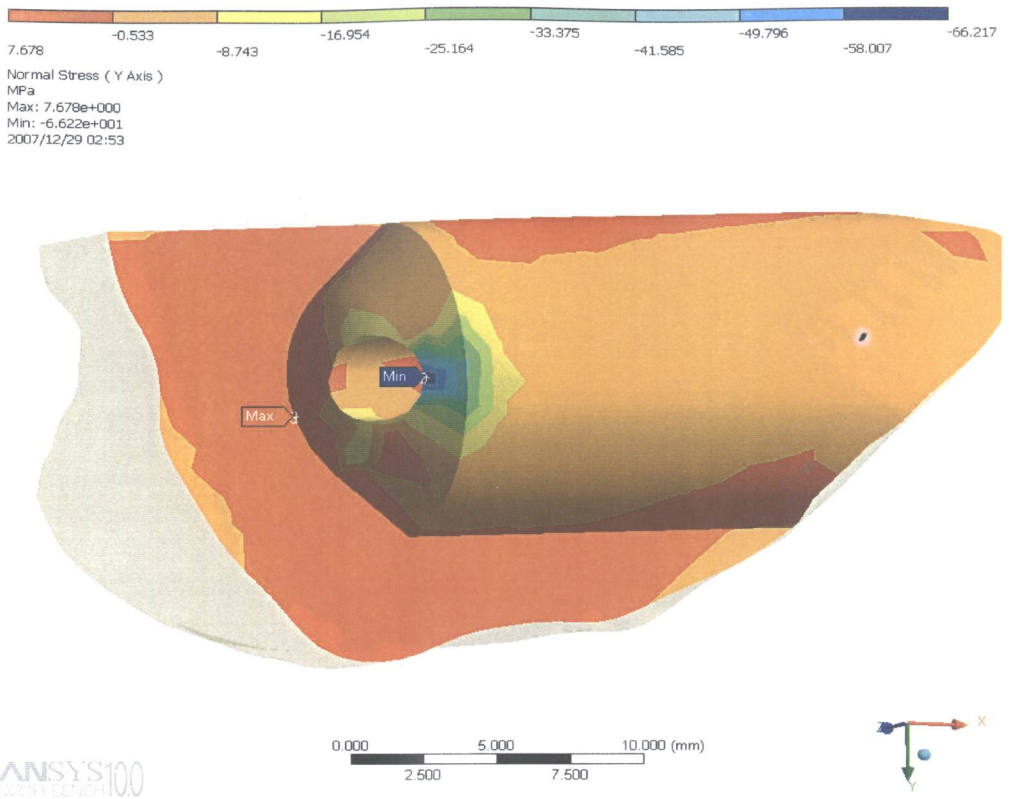

Figure 5.22 Normal stress Y-axis. CPP Implant. Combination 7

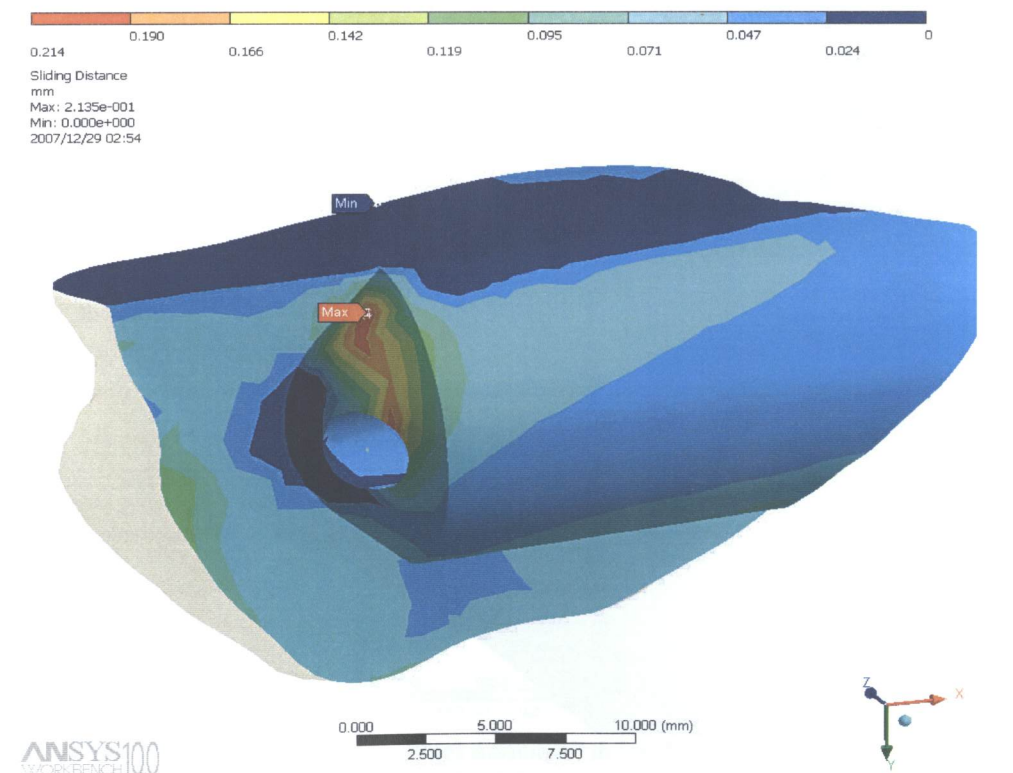

Figure 5.23 Sliding distance. CPP Implant. Combination 7

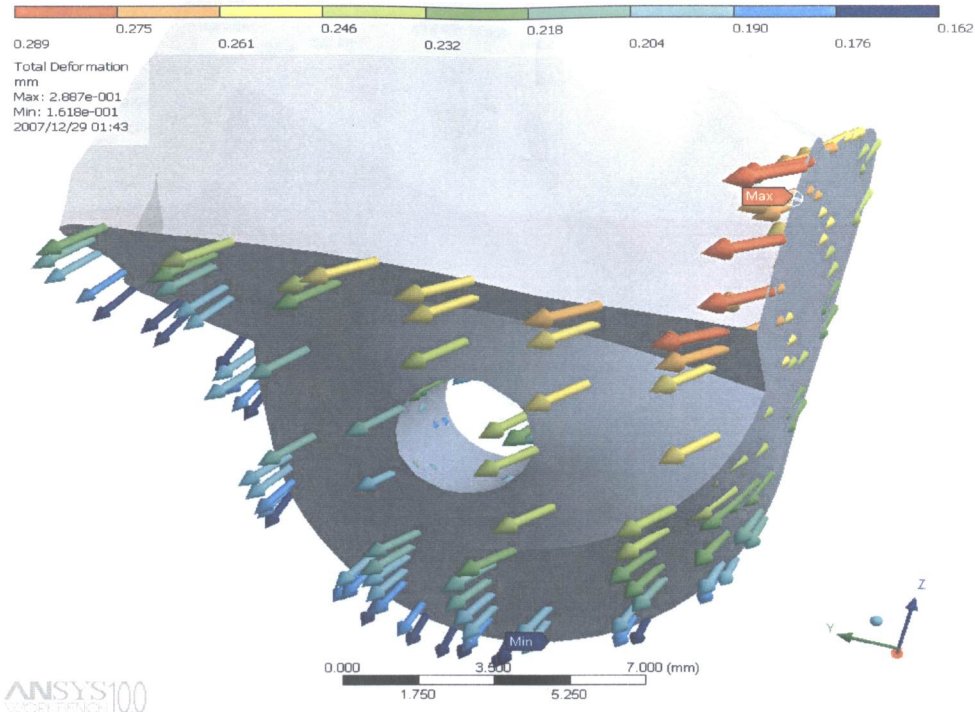

Figure 5.24 Total deformation of CPP Implant Contact Surfaces. Combination 7.

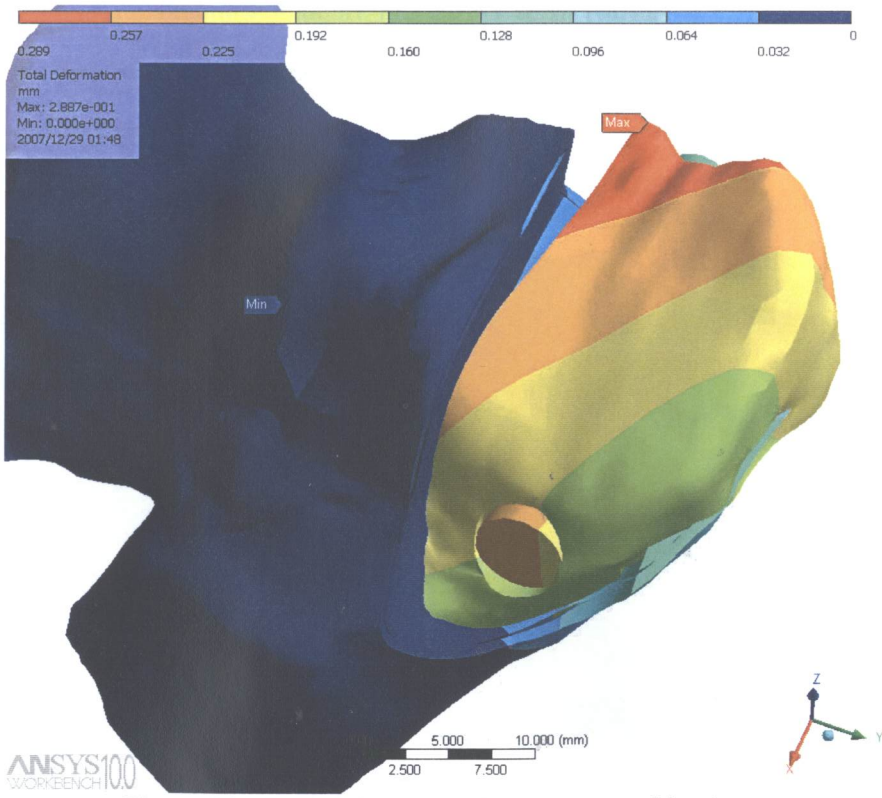

Figure 5.25 Total deformation for contact combination 7.
Note that the illustration of the deformation is exaggerated.

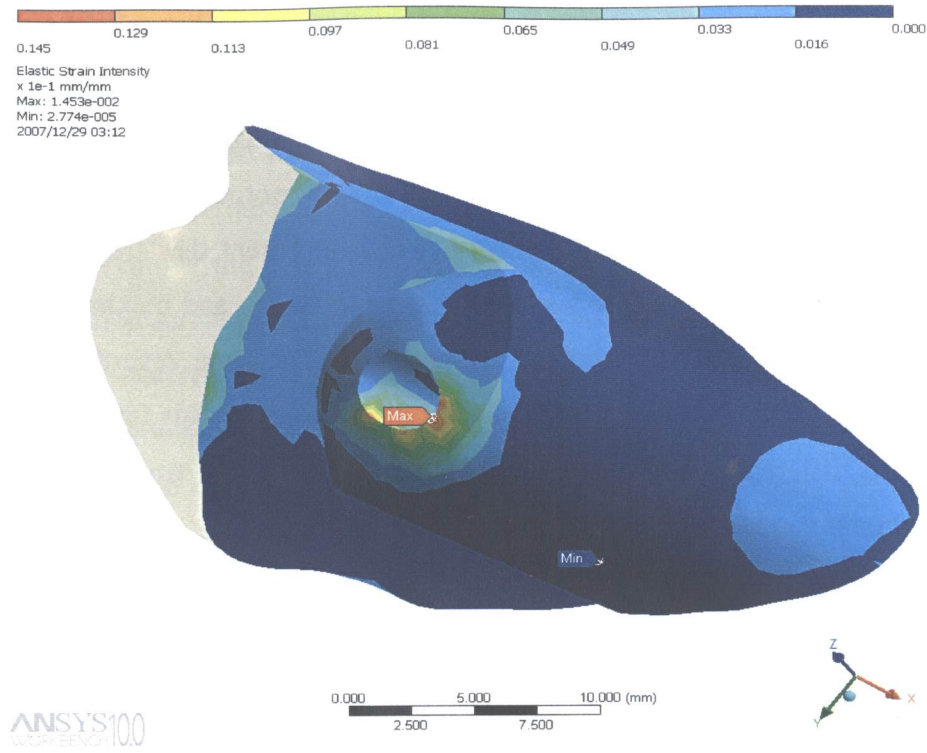

Figure 5.26 Strain intensity Distribution. CPP Implant. Combination 7

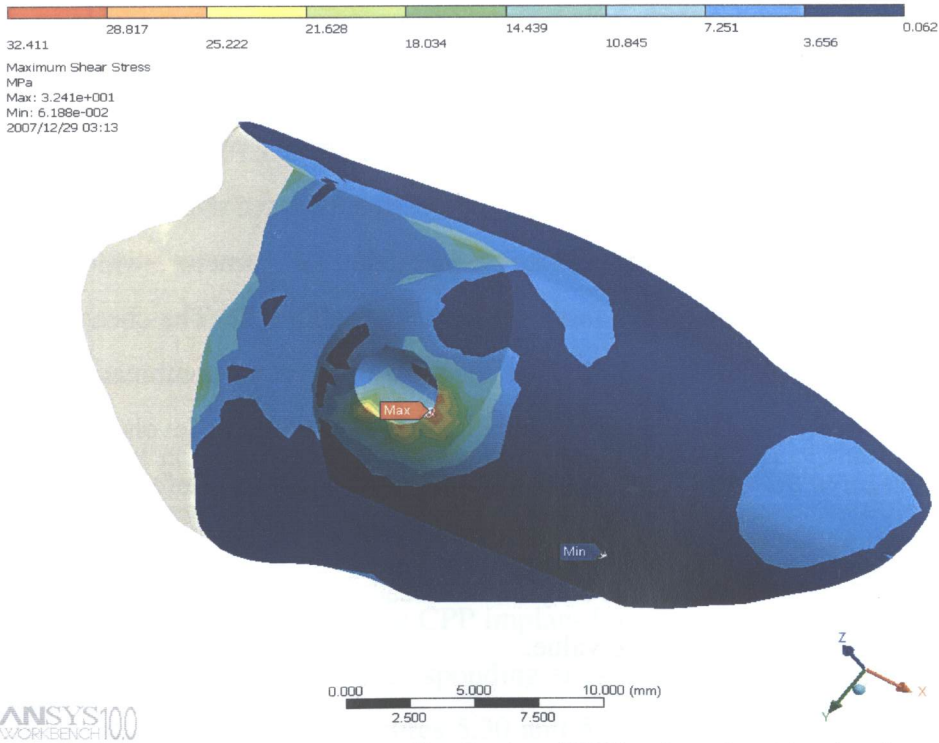

Figure 5.27 Maximum shear stress distribution. CPP Implant. Combination 7

For contact combination 7, the location of the highest shear stress occurred on the dorsal side keel surface, as shown in Figure 5.27. The largest sliding distance occurred at the dorsal keel surface/cancellous bone interface, in the location which is shown in Figure 5.23. The location of maximum normal stress in the y-direction coincided with the elastic stress intensity (which represent the stress at a point due to pressure from combined tensile and compressive stresses), and maximum shear stress as shown by Figures 5.22, 5.26, and 5.27, respectively. The same, regarding the locations of the maximum values of the stress and sliding distance, also holds for contact combination 6, the only difference being that the values are 7% and 22 % smaller, respectively, than contact combination 7 (see Table 5.10).

As described in Section 4.4, the early stages of the implant life span are described by two type of contacts: no-separation and frictionless. For combination 3 and 7, the contacts between the CPP implant and the other assembly elements are solely described by these two types of contacts. Ansys predicts similar tensile response, which is reflected by a similar value of the safety factor based on the maximum stress theory. The differences are in the maximum values of the stresses in compression where the normal stress in y-direction is 62 % higher for the combination 7. Shear stress in the xy-plane is 50 % higher in the combination 7, while the stresses in the other plane are equal.

Use of the bonded type contact in one or more CPP implant contact interfaces, improved the stress distribution and overall performance of the implant. This is reflected by the smooth distribution of the stress over the implant structure which is shown by the high values of all three safety factors evaluated (Table 5.8). The shear safety factor and the maximum stress distributions over the CPP for contact combination 5 are shown in Figures 5.20 and 5.21 indicating the location of elevated stress levels.

Figures 5.24 and 5.25 show the directional and total deformation of the implant for contact combination 7. In comparison with other contact combinations, the direction of the deformation changes not only on the location of the occurrence of these maximum deformations but as well in the value.

5.2.3 Use of a biodegradable screw

In the original design, it was assumed that the implant would be initially fixed using a titanium screw, to be removed after some bone ingrowth occurred. A more desirable situation would be the use of a biodegradable screw, which would not require a second surgery to remove the screw. Therefore, an analysis of the assembly using a biodegradable fixation screw was also performed. The fixation screw was assumed to be of the same CPP material as the implant, and the same contact conditions were implemented except combination 6. The analysis with the biodegradable fixation screw was conducted for the 6 combinations listed in Table 4.6. A summary of the stress results with biodegradable screw are listed in Table 5.12 and the maximum sliding distances are listed in Table 5.11.

Table 5.11 Sliding distances for implant using biodegradable screw

Contact Combination (Table 4.6)	Maximum Sliding Distance (μm)
1	48
2	76
3	101
4	197
5	225
7	254

For all contact combinations except for combination 1, failure of the implant or fixation screw due to elevated stress would be expected to occur, or unacceptable sliding distances were observed, as can be seen in Tables 5.11 and 5.12. As examples, the distributions of the sliding distances of the CPP implant for two contact combinations are shown in Figures 5.28 and 5.29. The corresponding stress distributions over the contact surfaces of the implant are shown in Figures 5.30 and 5.31, in which the location of the maximum stresses are seen to occur at the screw exit on the dorsal side of the keel.

Table 5.12 FE results for the implant using CPP biodegradable fixation screw

Modified CPP Implant with Biodegradable Screw		Contact Combination 1		Contact Combination 2		Contact Combination 3		Contact Combination 4		Contact Combination 5		Contact Combination 7	
		Implant	Fixation Screw	Implant	Fixation Screw	Implant	Fixation Screw	Implant	Fixation Screw	Implant	Fixation Screw	Implant	Fixation Screw
Normal Stress (MPa) X-Axis	Tension	12.6	16.1	26.4	13.7	26	17	10.2	17	9.2	14.2	14.1	33.8
	Compression	-8.8	-8.1	-9.9	-22.4	-10	-12.3	-8.5	-26	-8.6	-26.2	-38.6	-22.9
Normal Stress (MPa) Y-Axis	Tension	10.2	8.3	14	2	13	4.4	14.5	3.2	18.1	4	9.6	11.9
	Compression	-9.4	-4.7	-20.4	-4.8	-27	-5.8	-7.7	-9.3	-7.2	-11	-69.2	-8.6
Normal Stress (MPa) Z-Axis	Tension	7.5	12.1	16.8	3.2	16.3	7	3.1	3.1	4.1	3.5	8	17.8
	Compression	-24.5	-6.1	-35	-10.3	-32.6	-6.2	-31.9	-11	-34.4	-13.1	-46.8	-8.9
Shear Stress (MPa) XY-Plane	Positive	3.8	10.8	7	5.2	7.3	4.5	9.3	6.4	10.2	8.3	10.9	11.5
	Negative	-3.9	-7.8	-4.9	-3	-4.3	-2.7	-5.3	5	-5.6	-6.4	-10.8	-17.7
Normal Stress (MPa) YZ-Plane	Positive	6.2	2.3	6.5	2.6	6.6	2	7.8	2.5	8.6	3.1	25.4	4.8
	Negative	-4.8	-2.2	-9.7	-1.7	-10.6	-1	-6.3	-1.2	-7	-1.6	-21.7	-4.5
Normal Stress (MPa) XZ-Plane	Positive	3.5	14.8	6.1	4.3	6	7.8	7.1	5	10.2	6	11.5	17.4
	Negative	-7	-5.2	-15.2	-9.8	-17.2	-2	-9	-5.7	-9.2	-7.5	-14.6	-5.9
Safety Factor	Max. Tensile	1.5	1.1	0.73	1.9	0.75	1.6	1.5	1.6	1.25	1.9	1.65	0.62
	Shear Stress	1	0.95	0.7	1.2	0.7	1.7	0.87	1.1	0.82	1.1	0.42	0.63
	Mohr-Coulomb	1.5	1	0.73	1.9	0.75	1.6	1.3	1.6	1.9	1.9	0.75	0.62

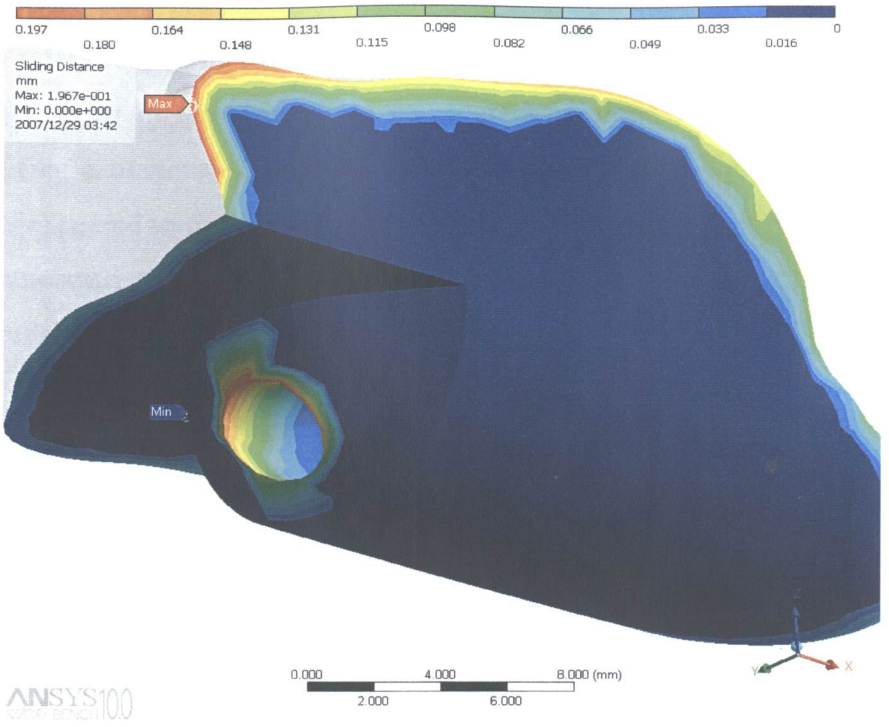

Figure 5.28 Sliding distance distribution for biodegradable fixation screw. using contact combination 4

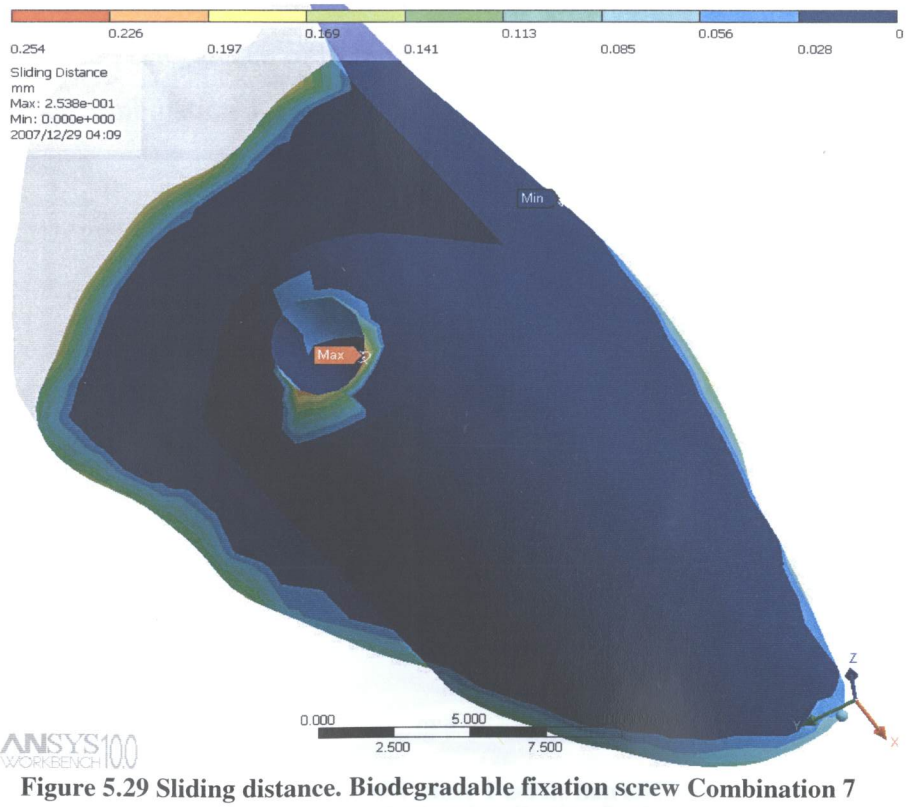

Figure 5.29 Sliding distance. Biodegradable fixation screw Combination 7

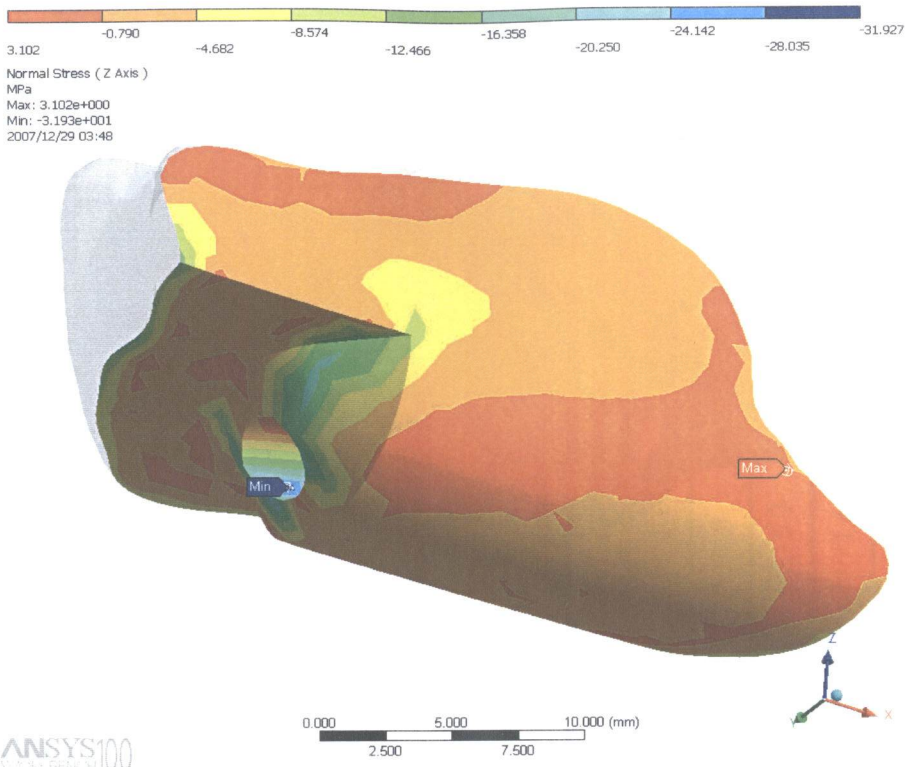

Figure 5.30 Z direction normal stress for biodegradable fixation screw using contact combination 4

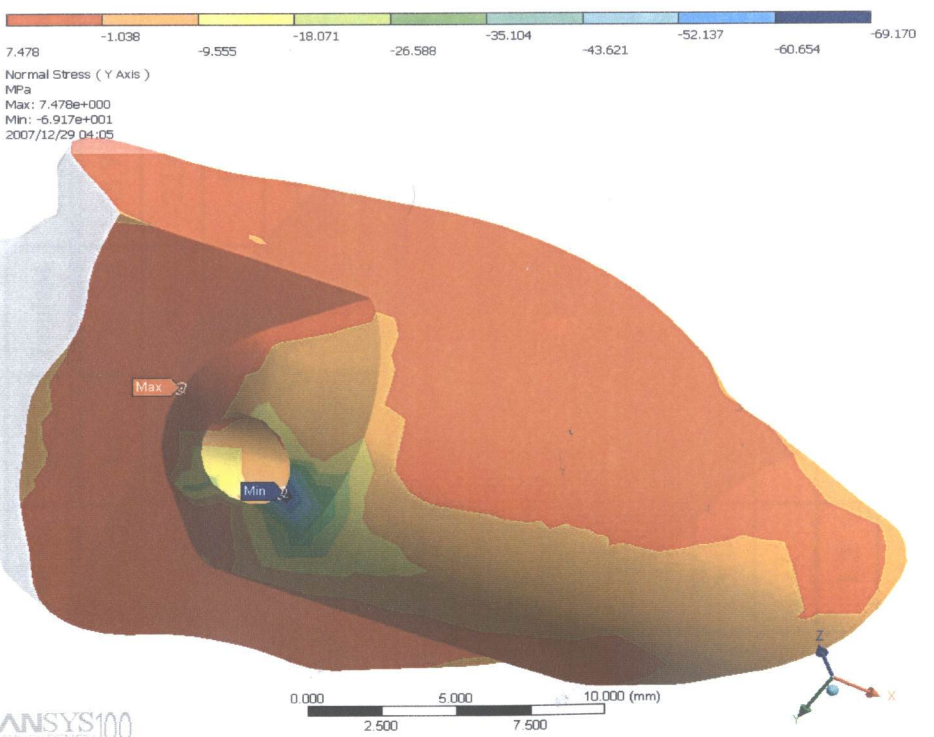

Figure 5.31 Normal stress Y Axis. Biodegradable fixation screw. combination 7

The safety factors in Table 5.12 show that the performance of the CPP implant – CPP fixation screw in terms of stress considerations alone was comparable with the system utilizing a titanium screw for contact combinations 1, 4 and 5. Fracture of the implant was expected to occur in contact combinations 2 and 3, while the fracture of the screw was expected only in the combination 7. The location of the expected fracture in the biodegradable screw for combination 7 is shown in Figure 5.32, where the stress is seen to be discontinuous at the boundary between the red and orange colored areas at where the screw exits the implant.

The other factor under consideration was the micromotion (sliding distance) occurring in the implant-bone interfaces. As can be seen in Table 5.11, only the sliding distance for contact combination 1 (48 μm) is below the critical value of 50 μm. All other contact combinations resulted in sliding distances that were between 76% (combination 2) to 400% (combination 7) above this critical value. This effect is attributed to the contact formulation for the bonded type which resulted in a more uniformly distributed stress distribution along the contact areas. Overall, it can thus be concluded that the performance of the implant with a CPP fixation screw was acceptable only for contact combination 1.

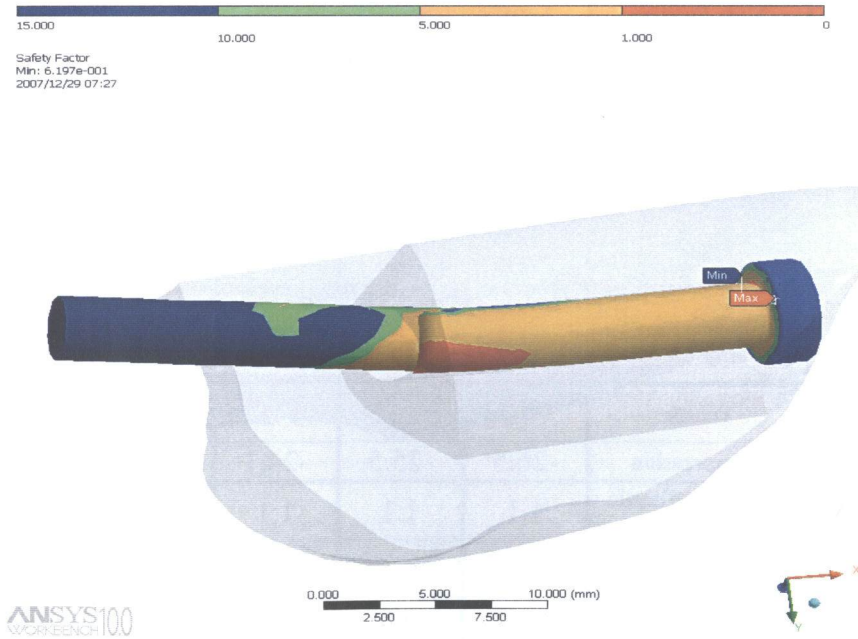

Figure 5.32 Fixation screw safety factor distribution for biodegradable screw contact combination 7

5.2.4 Dependency of implant performance on titanium screw tightening force

Discussions with the surgeon on the research team revealed that the torque applied while tightening implant screws is generally not controlled carefully, and therefore the resulting tensile force within the screw can potentially vary significantly from surgeon to surgeon A number of analyses were thus performed to determine what effect, if any, that this screw force might have on the stress distribution in, and sliding distance of, the CPP implant. For this purpose, contact combination 3 was used and the FE analysis was conducted over several values of screw force values. The contact combination 3 was selected for this type of analysis due to the fact that with this type of contact describes the contact conditions just after implant insertion and requires less time to achieve a solution compared to the contact combination 1. A summary of the results appears in Table 5.13

Table 5.13FE Results for various screw forces

Modified Model Combination 3		Screw Tensile Force					
		0N	32 N	75 N	160 N	320 N	810
Shear Stress (MPa) x-y plane	Max. Positive	7.4	5.9	7.9	11.6	19.8	36.4
	Max. Negative	-7.3	-7.4	-8.9	-16.3	-19.3	-42.4
Shear Stress (MPa) y-z plane	Max. Positive	17.8	17.4	16.8	15.8	24.4	26.8
	Max. Negative	-8.3	-10	-12..5	-16.8	-27.2	-17.5
Shear Stress (MPa) x-z plane	Max. Positive	10.3	9.9	9.4	8.5	11.1	34.7
	Max. Negative	-14.9	-15.5	-16.2	-16.5	-19.5	-49
Normal Stress (MPa) x-axis	Tensile	18.1	18.5	19.2	20.4	23.2	49
	Compression	-13.2	-15.3	-18.1	-22.9	-33.7	-45
Normal Stress (MPa) y-axis	Tensile	14.1	14.9	18.9	24.6	28.3	24
	Compression	-20	-22.5	-25.3	-36.3	-63.7	-83
Normal Stress (MPa) z-axis	Tensile	14.2	14.2	14.2	19.9	32.7	17.8
	Compression	-26.5	-25.5	-24.1	-32.1	-54	-94
Safety Factor	Maximum Tensile Theory	1.1	1.1	1.1	0.92	0.5	0.5
	Mohr-Coulomb Stress	0.75	0.75	0.75	0.78	0.4	0.25
	Maximum Shear Stress	0.93	0.9	0.86	0.62	0.48	0.4

For fixation forces less than 75 N, the performance of the implant was essentially independent of bolt force. This is indicated by the relatively constant values of stresses in tension or compression and the identical safety factors shown in Table 5.13.However, for higher screw forces, the performance of the system deteriorated, as can be seen by the dramatically increasing stress values for an applied load of 320 and 810 N. In these cases, the tensile stresses in the Z and X directions exceeded the tensile strength of the CPP material, indicating that fracture of the implant would likely occur.

As shown in Figure 5.33, for a screw force of 320 N, the location of the expected failure was at the horizontal surface near the keel indicated by the low value of safety factor (red zone). For the force of 810 N the location was shifted to the screw exit at the back surface.

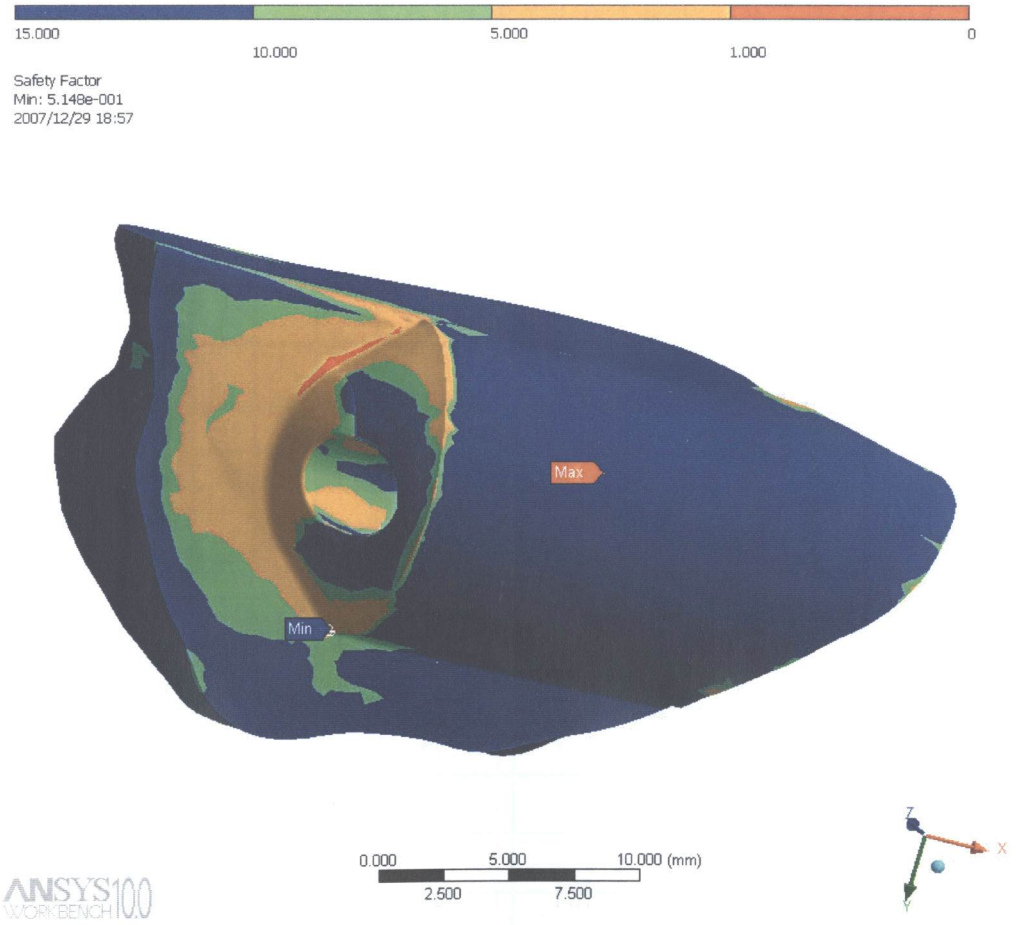

Figure 5.33 Safety factor (Maximum Tensile Stress Theory) for screw force of 320 N

5.2.5 Implementation of Orthotropic bone properties.

All analyses performed thus far had as their aim to determine the optimal shape and configuration of the implant, and used isotropic material properties. Using the final optimized geometry presented in Section 5.2.2, orthotropic material properties (Table 4.2) were considered for both the cortical and cancellous bone, in an effort to obtain a better estimate of implant behavior under real conditions. A cylindrical coordinate system was used with the axial, tangential and radial directions aligned with the z, y, and x directions, respectively, and the transversely isotropic properties of the cortical bone were applied based on this coordinate system. The anisotropic properties of the cancellous bone were applied based upon the global coordinate system with the proximal-distal, medial-lateral, and dorsal-ventral directions aligned with z, y, and x axes respectively.
A summary of the results for the FE solutions are shown in Tables 5.14and 5.14 respectively, together with the results for the isotropic case as a comparison. The analysis with the anisotropic properties was accomplished over only the first five contact type combinations listed in the tables.

Table 5.14Maximum sliding distances for model using anisotropic bone material properties

Implant Contact Combinations From Table 4.6	Maximum Sliding Distances (μm)	
	Isotropic	Anisotropic
1	2	6
2	32	32
3	37	34
4	3	3
5	2	3

Table 5.15Comparison of the orthotropic and isotropic

Modified CPP Implant with Biodegradable Screw		Combination 1		Combination 2		Combination 3		Combination 4		Combination 5	
		Isotropic Properties	Anisotropic Properties	Isotropic Properties	Anisotropic Properties	Isotropic Properties	Anisotropic Properties	Isotropic Properties	Anisotropic Properties	Isotropic Properties	Anisotropic Properties
Normal Stress (MPa) X-Axis	Tension	7.7	12	19	22.2	19.2	23.8	5.2	11.3	5.2	11.5
	Compression	-7.5	-9.1	-10.9	-10.6	-18.1	-28.5	-10.1	-29.1	-10	-29.1
Normal Stress (MPa) Y-Axis	Tension	6	9.6	11.9	14.1	18.9	14.8	8	18.3	8.1	14.3
	Compression	-14.4	-9.2	-29.8	-23.7	-25.3	-42.7	-7.9	-19.5	-7.9	-19.5
Normal Stress (MPa) Z-Axis	Tension	3.6	7.5	11.4	17	14.2	22.2	4	15.7	3.6	15.7
	Compression	-27.4	-17.7	-39.9	-27.7	-24.1	-33.4	-19.9	-29	-20	-29.3
Shear Stress (MPa) XY-Plane	Positive	3.9	2.8	6.8	8.5	7.9	10.6	3.9	6.7	3.9	6.7
	Negative	-3.6	-3.1	-5.7	-6.9	-8.9	-10.6	-5.3	-6.6	-5.1	-6.6
Normal Stress (MPa) YZ-Plane	Positive	10.5	6.6	17.8	8.2	16.8	19.1	10.3	17.2	10.4	17.2
	Negative	-5.2	-5.1	-6.8	-12	-12..5	-20.1	-5.7	-15.1	-5.8	-15.2
Normal Stress (MPa) XZ-Plane	Positive	5.4	3.9	6.8	7.1	9.4	13.2	7.6	8.4	7.7	8.4
	Negative	-7.8	-7.3	-12.2	-18.7	-16.2	-21	-9.6	-9.6	-8.8	-9.6
Safety Factor	Max. Tensile	3.1	2	1.2	0.8	1.1	0.7	2.91	1.6	2.9	1.63
	Shear Stress	1	1.3	0.64	0.61	0.75	0.58	1	0.66	1	0.66
	Mohr-Coulomb	1.8	1.7	1.1	0.71	0.86	0.64	1.8	1	1.8	1

The sliding distances estimated for the cases where the anisotropic bone material properties were implemented are very similar to the values of the isotropic case. There is no significant difference on the contact combinations implemented. For all contact combinations, Ansys returned almost identical values which indicate that the assumption of isotropy in determination of the best design and stated by [39] is an accurate and fair assumption.

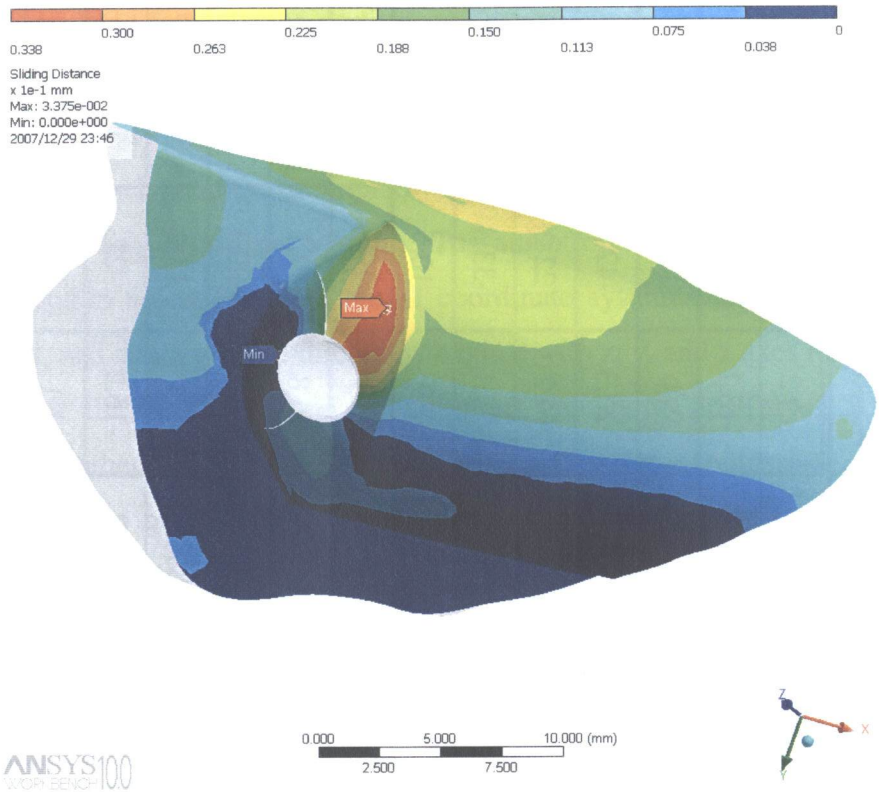

Figure 5.34 Sliding distances for anisotropic bone material properties combination 3

The main difference between the isotropic and anisotropic model results was in the stress distribution over the structure. For the anisotropic case, the stresses were generally slightly higher, resulting in a direct impact on the safety factor estimation, which were lower compared to the isotropic case for each contact combination analyzed. As mentioned previously, because in the loads used were extremely conservative, there was enough confidence that the selected model was adequate. The verification of this model was the subject of the experimental analysis presented in section 5.4.

5.3 Accuracy of the Solution

The accuracy of the solution for a particular FE model depends to some extent on how well the FE model describes the actual geometry of the implant. The FE description of the geometrical model, however, depends on the number of elements used in the meshing process. The scope of the present section was the variation of the results returned by the FE simulation with an increase in the mesh density (decrease of the elements size).

For this purpose the analysis was performed with five element sizes: 1.5, 0.2, 0.9, 0.8, and 0.6 mm, denoted by the numbers 1, 2, 3, 4, and 5, respectively in the figures in this section.

The variations of the stresses with the mesh density is shown in Figures 5.35 through 5.39 for contact combination 3 in Table 4.6, while the variation of reaction forces acting upon the contact interface of CPP implant with the bone elements, acting on the centroids of contact areas, are shown in Figures 5.38 through 5.40.

Convergence of the solution, based upon element size (a decreasing difference in successive stress values with decreasing element size which was selected at 5%) was generally achieved for most of the parameters analyzed. Nevertheless, some of the parameters seemed to oscillate, such as the case of the shear stress on the yz-plane in Figure 5.36. Another example is the variation of the reaction force acting upon the keel's surface on the dorsal side where the increase of the number of elements result in the continuous decrease of the reaction force as shown in Figure 5.40.

For both situations mentioned above, the solution was not considered converged because the these parameters change by 17 % and 15 % respectively, relative to global convergence norm set at 13 %.

The same type of analysis was conducted over specific points of the CPP implant contact surface with cancellous and cortical bone. Further investigation was restricted by the element/node number retained by the Ansys license, nevertheless the results obtained the information obtained was abundant and convincing for the accuracy of the solution

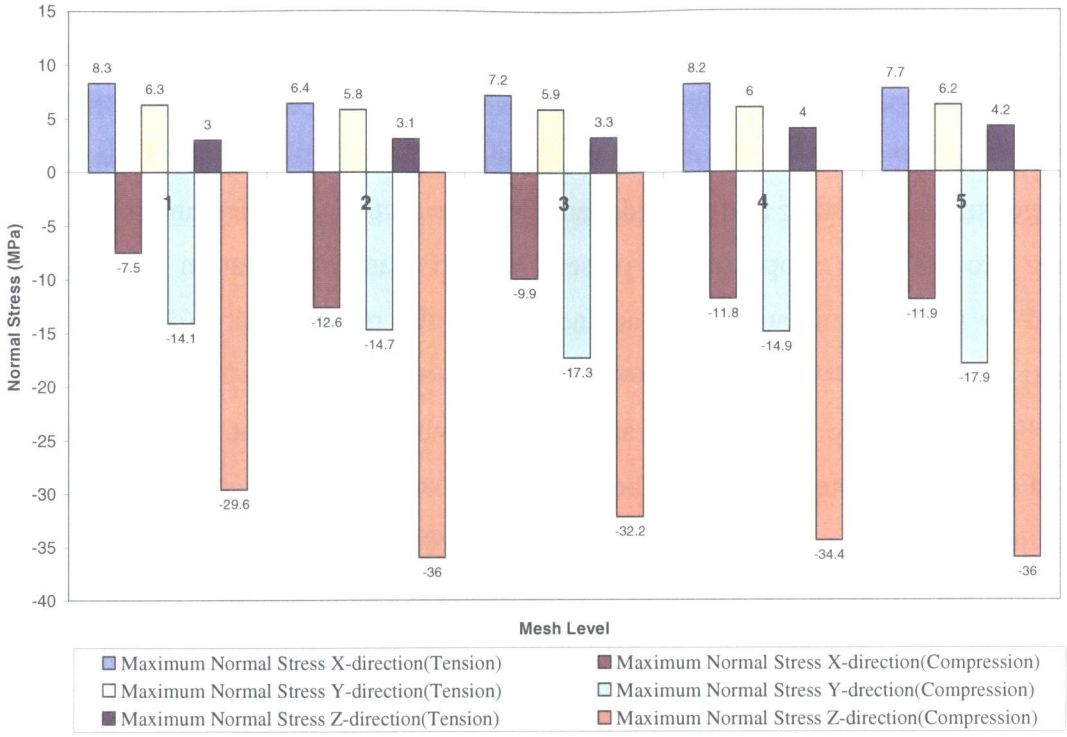

Figure 5.35 Normal stress variation as function of element size. Contact combination 1

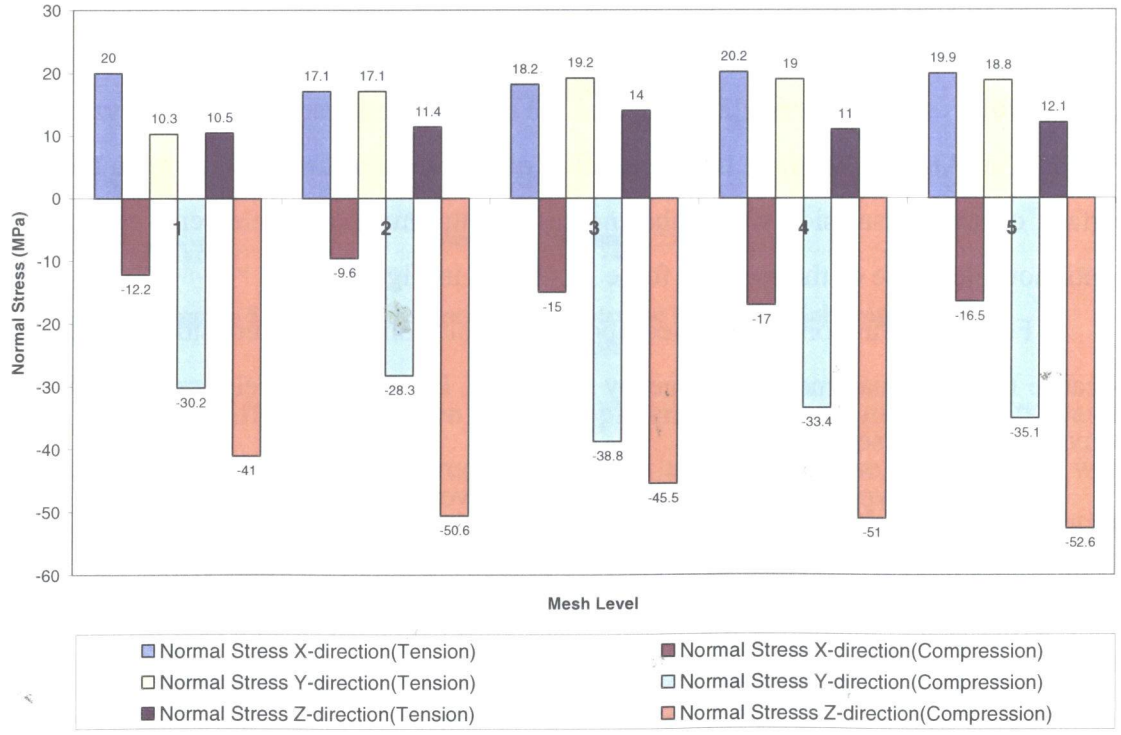

Figure 5.36 Normal stress variation over number of elements. Contact combination 3.

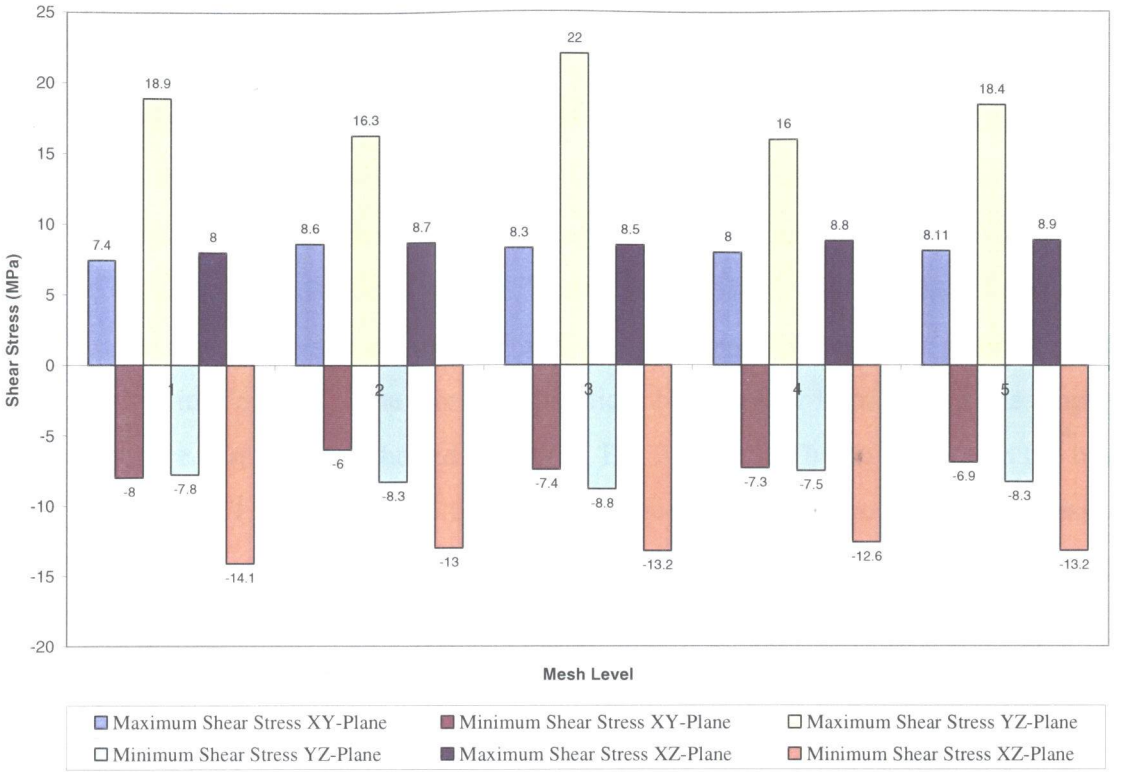

Figure 5.37 Shear stress variation over number of elements. Contact combination 3

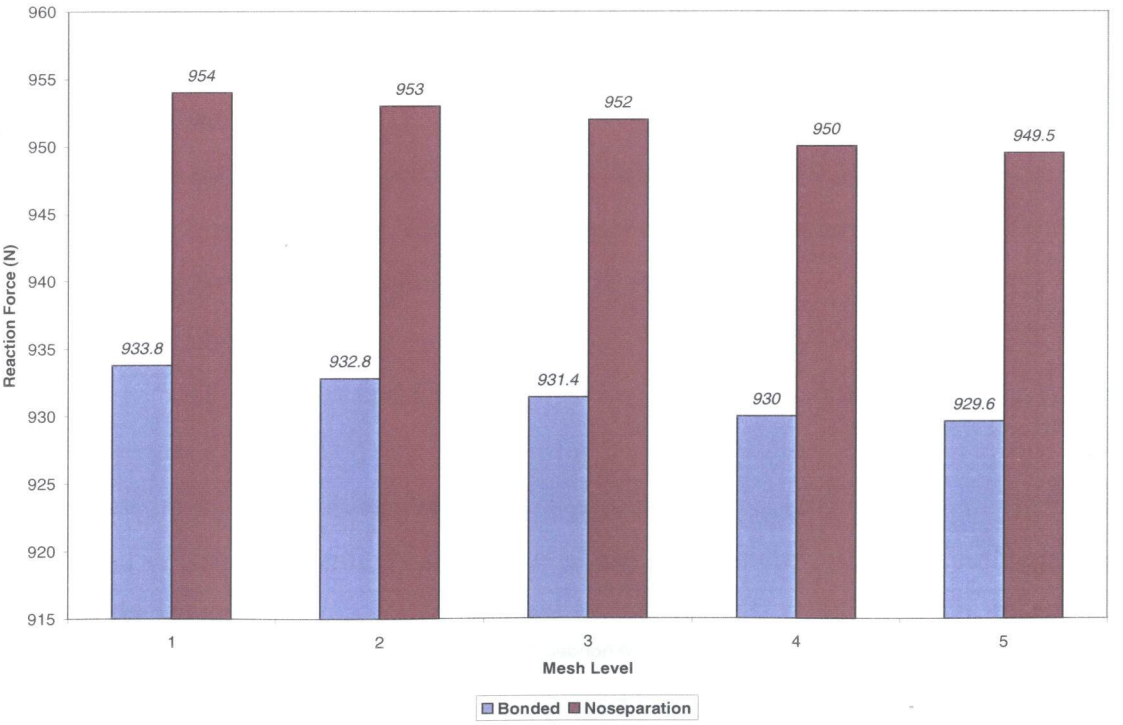

Figure 5.38 Z-direction reaction force at cortical and CPP implant interface. Contact combination 3

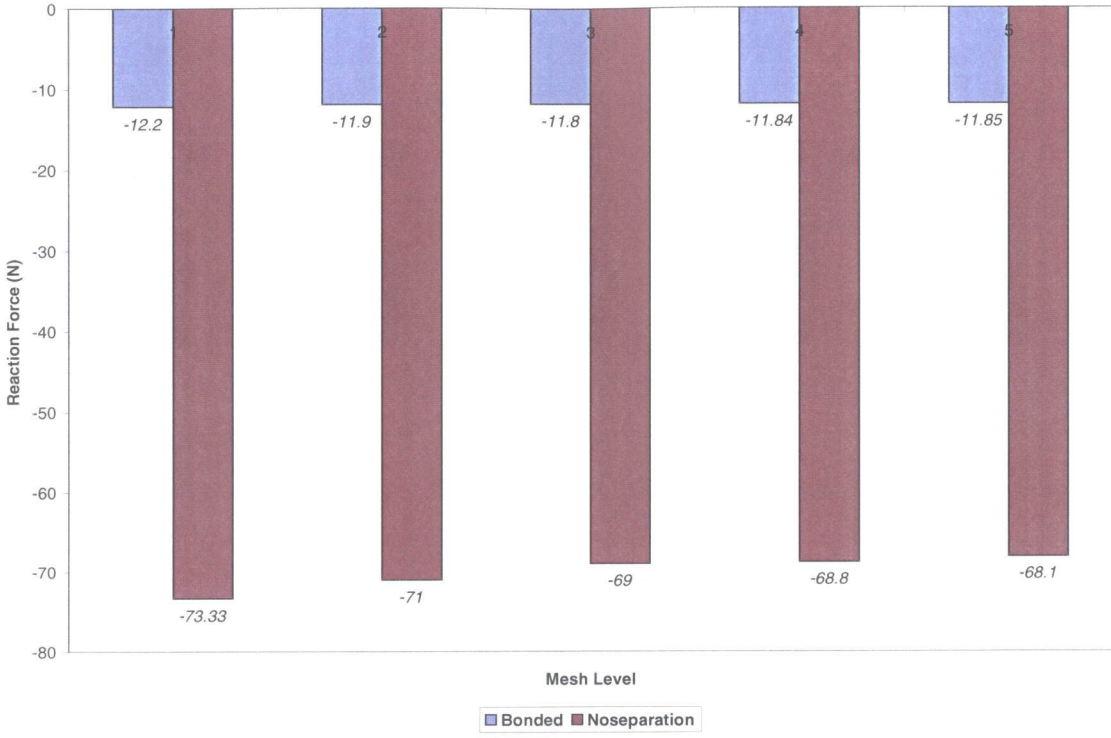

Figure 5.39 Y-direction reaction force at cancellous and CPP implant interface. contact combination 3

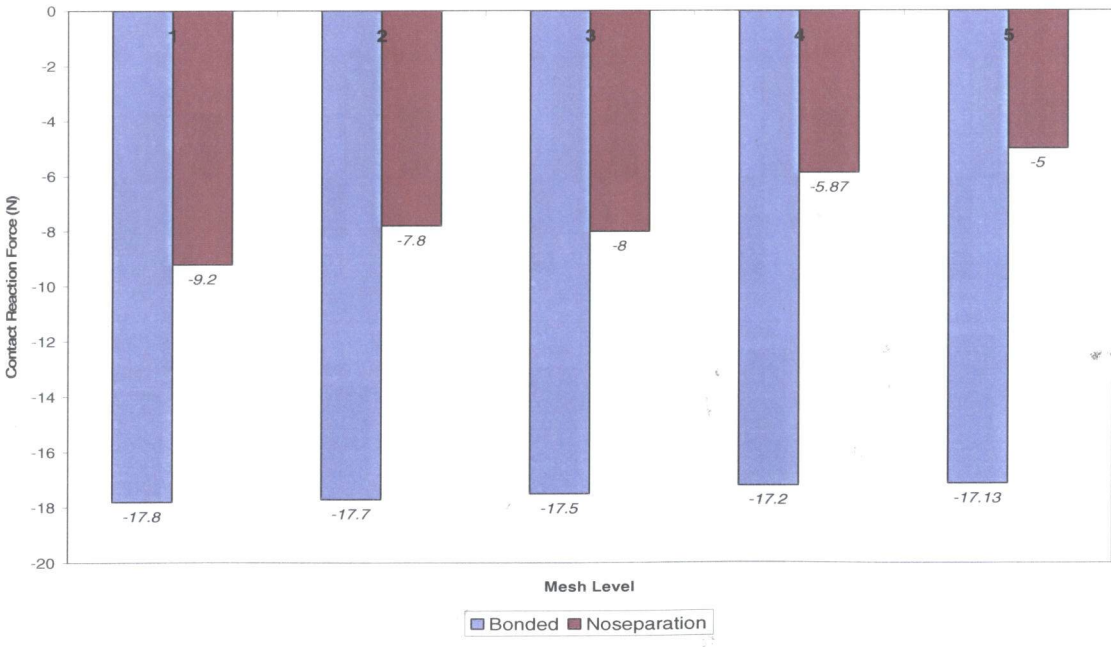

Figure 5.40. Y-direction reaction force for cancellous and CPP implant interface. contact combination 3

5.4 Experimental Verification

The final stage of the design consisted of an attempt at experimentally verifying the finite element model. An implant, derived directly from CAD files of the final implant (Section 5.2) was manufactured using advanced numerical machining methods by research partners at the University of Waterloo on supervision of Dr. Erkormaz. A sheep tibia, to which the implant was secured, was obtained from research partners at Mt. Sinai hospital in Toronto. The bone preparation for implant hosting and the implant insertion was performed by orthopedic surgeon Dr. P. Zalzal. The author potted the bone distally (Figure 5.41), and attached two strain gauges, and an instrumented compression test was performed using an Instron universal testing machine at the Faculty of Dentistry at the University of Toronto, with the assistance of Dr. J. Wang.

5.4.1 Experiment Apparatus.

1. **Instron** (3360 Series Dual Column Testing System, 825 University Ave., Norwood, MA) universal testing machine with data acquisition unit.
2. CPP implant
3. **Vishay** strain gauges (R=120 Ω ±0.3 % with gauge factor 2.07 ±5%) (Vishay Intertechnology, Inc., 63 Lancaster Avenue, Malvern, PA)
4. M-bond 200 adhesive liquid and plaster of Paris.
5. Sheep's tibia
6. Cylindrical container and Cerrobend potting material used in the distal fixation of the bone.
7. Pressure jig made of resin material (Research Triangle Park, Reichhold Inc,USA) used in cosmetic dentistry serving as a load distributor over the pressure surface of the implant.

5.4.2 Procedure

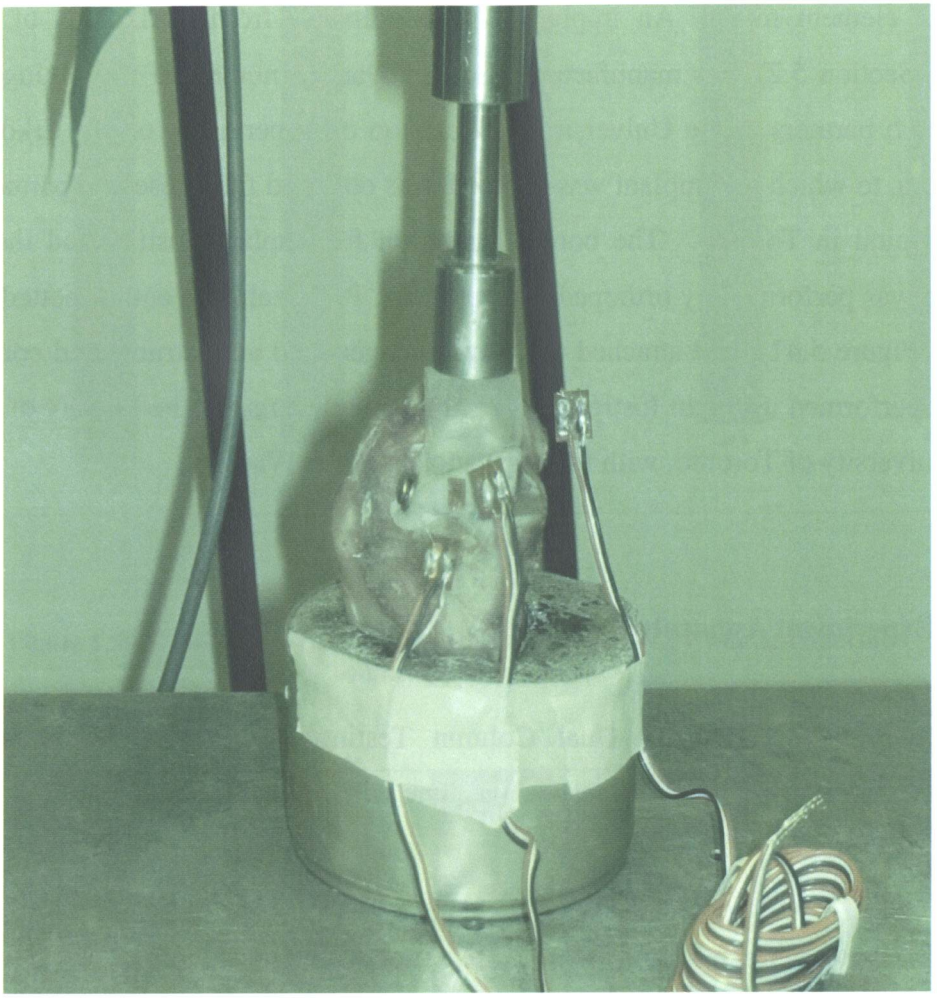

Figure 5.41 Experimental set-up showing potted sheep tibia with attached strain gauges in Instron Universal Testing Machine

The first step in the model preparation for testing was the insertion of the provided CPP implant into the hosting bone, as shown in Figure 5.41. To accomplish fixation, a screw with 3 mm diameter was used. As can be seen from Figure 5.42, there was a large mismatch between the hosting bone and the CPP model because of the fact that the implant was derived from a different sized sheep tibial plateau than that which was provided for this test. Such large specimen to specimen variations in bone size and material properties are an unfortunate reality in biological testing.

The bone was potted distally to a height 40 mm using Cerobend, a metal alloy of bismuth, lead, tin, and cadmium with a melting temperature of 70°C, to provide a well defined zero displacement boundary condition in the FE model, and a stably fixated bone for the testing. The potting of the bone into the container was facilitated by the use of a commercial gas torch.

Figure 5.42 CPP implant attached to the host bone.

Three locations were chosen for the attachment of the strain gauges, two on the medial side and one in the dorsal side. Figure 5.43 shows the locations and number convention of the gauges on the medial side. Both gauges attached in the medial side were located 17 mm from the vertical surface of the CPP implant, and with the of 4 mm distance from the horizontal surface (mid axis of the gauge).

The attachment procedure of the strain gauges included the standard decreasing, abrading, and conditioning of the attachment location. Initial attempts at attachment were not successful due to the fact that the M-200 bond adhesive did not stay at the implant

surface, but quickly disappeared into the highly porous CPP ceramic material. This obstacle was overcome by the application of a very thin layer of plaster of Paris at the application site, followed by abrading of the areas where the plaster was applied. In The gauges were oriented in the proximal-distal direction.

Figure 5.43 also shows the pressure jig; consisting of resin material used in cosmetic dentistry, which was used in order to have a uniform pressure distribution over the implant surface, thus avoid any possible local fracture on the upper surface of the implant. The pressure jig was produced with the generous assistance of the Orthodenstitry laboratory of the University of Toronto, Faculty of the Dentistry. During this procedure, unfortunately, the pressure gauge attached to the dorsal side of the implant was accidentally removed from its attachment location due to the very tight space in which the operation of generating the pressure jig occurred. The experimental results will therefore be considered only for the two gauges attached on the medial side.

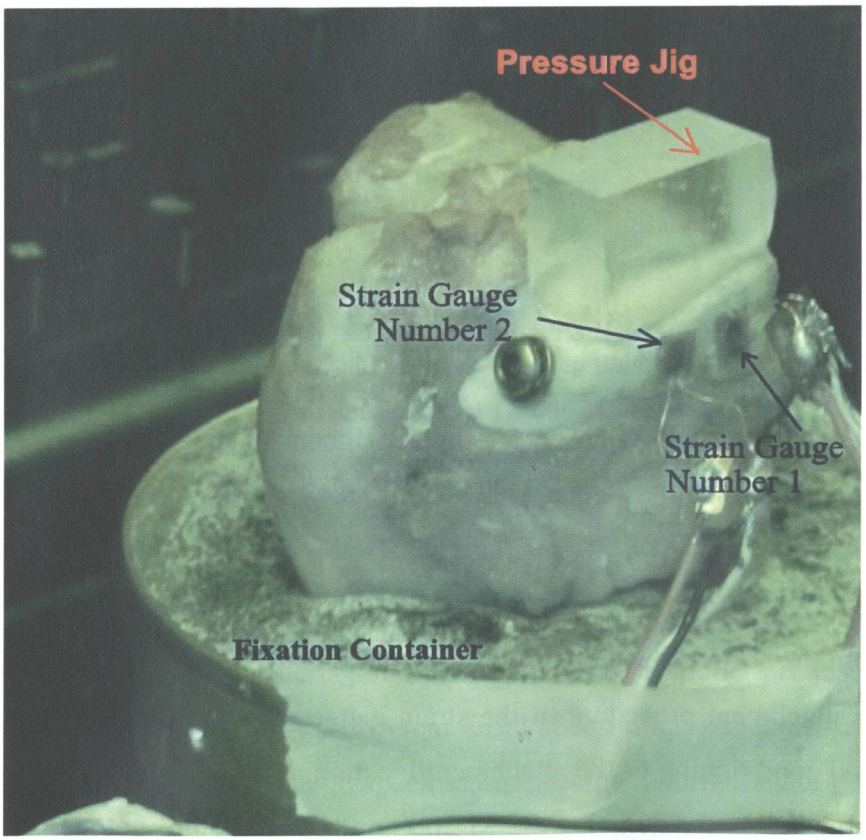

Figure 5.43 Experimental set-up of the bone assembly.

5.4.3 Experimental Procedure and Results

As shown in Figure 5.44, the force exerted by the actuator was applied through the pressure jig over the upper surface of the CPP implant and the strain measurements were registered by the data acquisition system. The force was applied with a step actuator displacement rate of 0.2 mm/min to a maximum load of 650 N. Load and strain measurements as a function of time are shown in Figures 5.44 – 5.46.

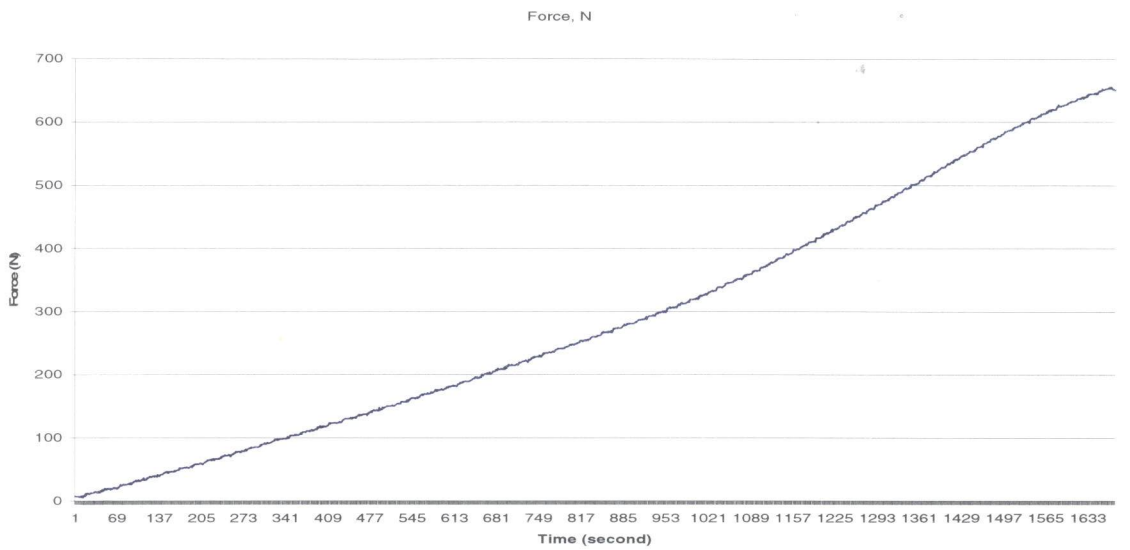

Figure 5.44 Force variation during experiment

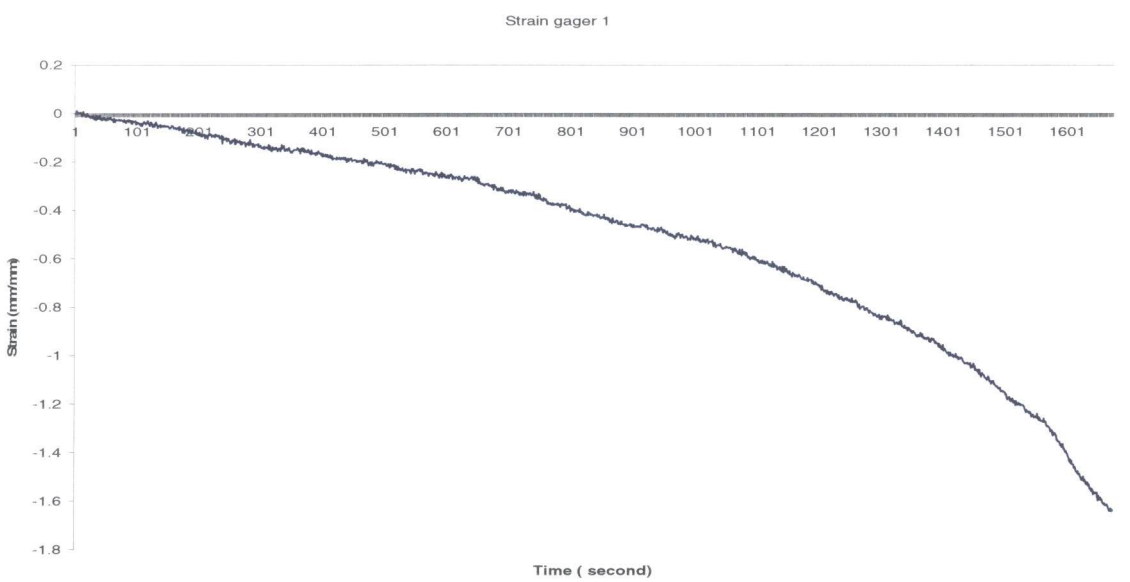

Figure 5.45 Strain measurements for gauge 1

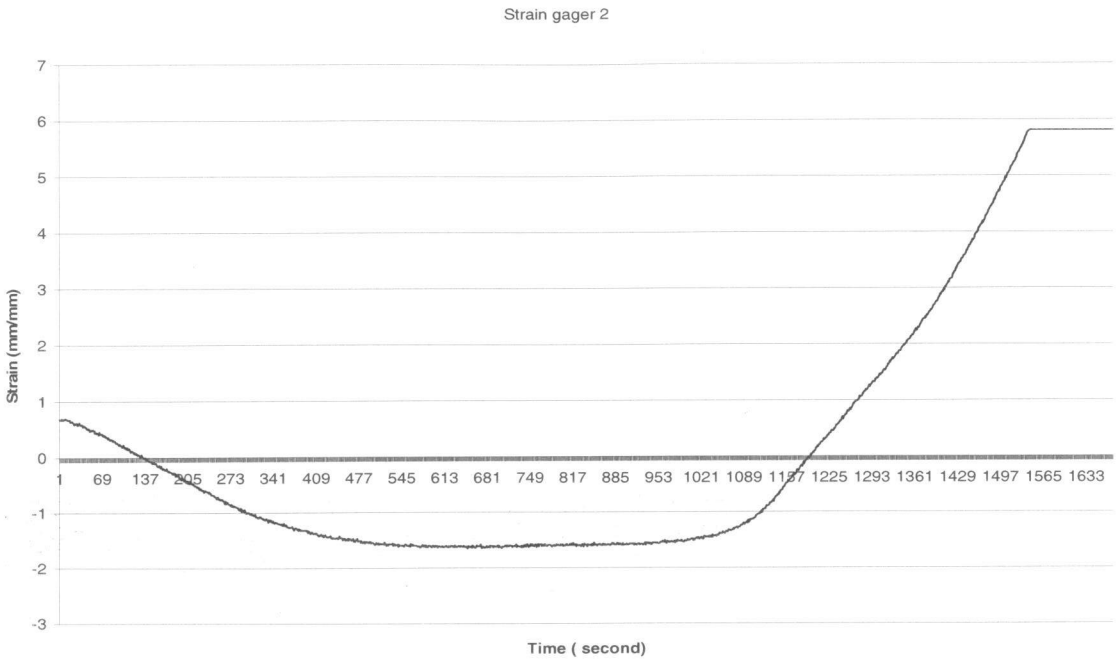

Figure 5.46 Strain measurements for gauge 2

5.4.4 Discussion of the experimental results

Visual inspection of the implant after the experiment did not reveal any damage to the CPP implant. Given that the maximum load applied, exceeded the reaction force registered for the sheep's gait cycle measurement [46] as mentioned in Section 4.2, this was an encouraging indication that the design was sound.

Analyzing the strain data experienced by the two gauges, from Figures 5.43 and 5.45, it can be seen that while gauge 1 experienced only compression, gauge 2 experienced a tensile load as well. The load transmitted through the resin pressure jig was applied through a surface 258 mm^2. Initially gauge 1 experienced a tensile load which decreased as the applied load increased, until the applied load reached 37.81 N (0.154 MPa) value for which this gauge sensed compression. This gauge continued to experience compression until the load was increased to 416.3 N (1.61 MPa) from which point the strain that this gauge sensed was again tensile. Saturation of the gauge was experienced when the load was increased to 604.5 N value (2.34 MPa).

The scale applicable to the reading is that the gauge is a reading of 1000 μ when the value obtained is 5. Thus, at the maximum load applied (650 N) the readings of the gauges 1 and 2 are 340 με (compression) and $1.16x10^{\wedge-3}$ (tension).

A direct comparison between the existing FE models already investigated and the experimental model cannot be conducted. As mentioned before, there was a noticeable difference between the assemblies due to the fact that the hosting bone was considerably larger than the original bone used to design the CPP implant (which resulted in a perfect match with the hosting bone). This difference in the volume occupied by the CPP implant relative to the removed volume of the hosting bone caused the contact surface between the implant and cortical/cancellous bone to be greatly affected.

Despite these discrepancies, the fact that the designed implant did not experienced failure indicates that the CPP implant designed displays considerable structural strength.

5.4.5 FE approximation of experimental model

An effort to approximate the experimental model with an FE model was made. To build the solid model of the tested bone would have required construction using CT scans, which were not available for the tibial host bone. The FE model was thus based on the pictures taken of the experimental bone assembly. Therefore, CAD modeling of the new FE model was accomplished with the same procedure mentioned in Chapter 3. The surface manipulations were conducted in the Rhinoceros 3.0 CAD modeling software, and consisted in the expansion of the dorsal cortical surfaces (inner and outer surfaces), expansion of the proximal tibia plateau surfaces, and expansion of the ventral side. The end result of the CAD modeling is shown in Figure 5.47.

Figure 5.47 Approximate FE model of the experimental assembly

In the model shown above, all the approximations of the CPP implant with cortical bone are based on visual observation of the experimental assembly. This is a factor that heavily affects the outcome of the comparison and will be discussed later in this section.

Figures 5.48 and 5.49 show the locations of the software probes used to monitor the z direction strain at the locations approximate to the strain gauges locations. Values of the strain at these locations are listed at Table 5.16 where in bold are the strain results of the probes that were in the closest positions to gauges 1 and 2.

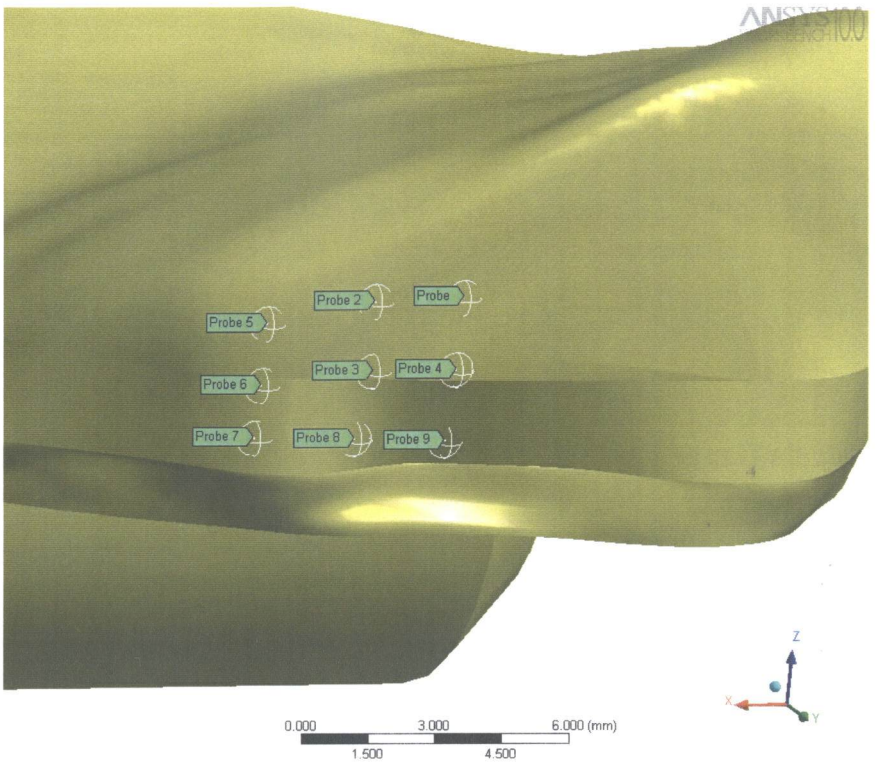

Figure 5.48 Probe points locations. Probe group 2. Strain gauge 2

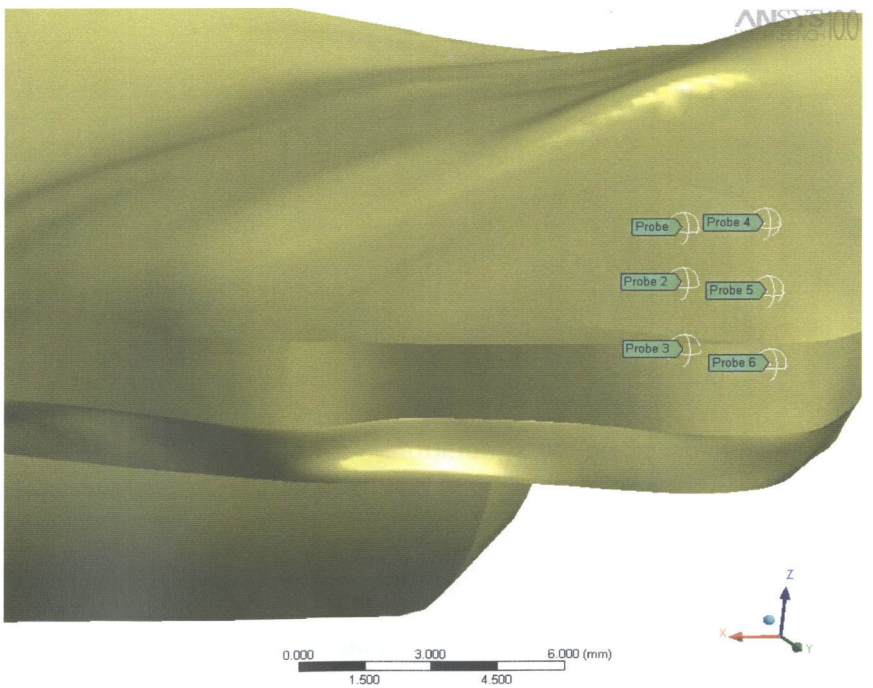

Figure 5.49 Probe points locations. Probe group 1. Strain gauge 1

Table 5.16 Strain in z-direction evaluated by Ansys

Strain Measurement from Ansys Simulation		Strain z-direction (με)		
		0.15 MPa	1.6 MPa	2.54 MPa
Probe Group 1 Strain Gauge 1	1	-15	-147	-230
	2	**-24**	**-234**	**-365**
	3	-39	-377	-589
	4	-22	-217	-339
	5	**-33**	**-329**	**-513**
	6	-31	-299	-467
Probe Group 2 Strain Gauge 2	1	-5.6	-56	-85
	2	-6.1	-59	-92
	3	**-15.5**	**-59**	**-235**
	4	**-6.9**	**-150**	**-105**
	5	-5.5	-67	-85
	6	-19.6	-191	-298
	7	-23.8	-234	-362
	8	-42	-411	-642
	9	-38	-367	-573

The location of the probes is shown in figures 5.48 and 5.49 the result at the desired location can be determined only by variations within a certain range and not by an exact value.

All the data listed in the Table 5.15 and the strain distributions shown in the in the Figures 5.50 – 5.52 are based on the simulations with contact combination 3. Due to the time required in the solution of the model with contact combination 7, it was not possible to present the results for that type of analysis.

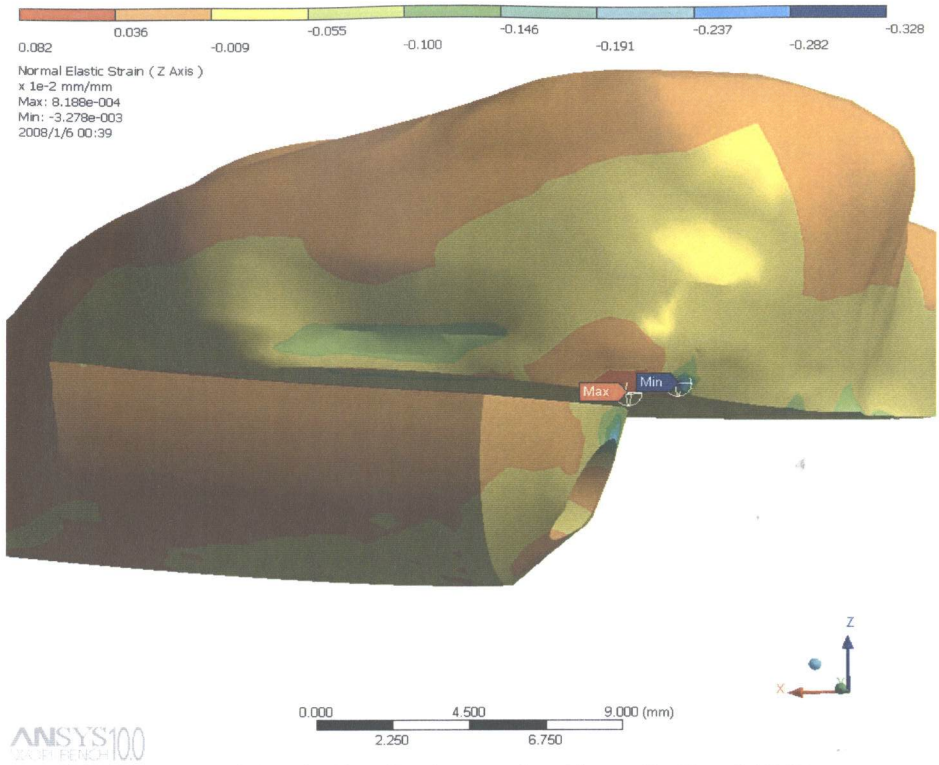

Figure 5.50 Strain distribution z-axis with applied load 1 MPa

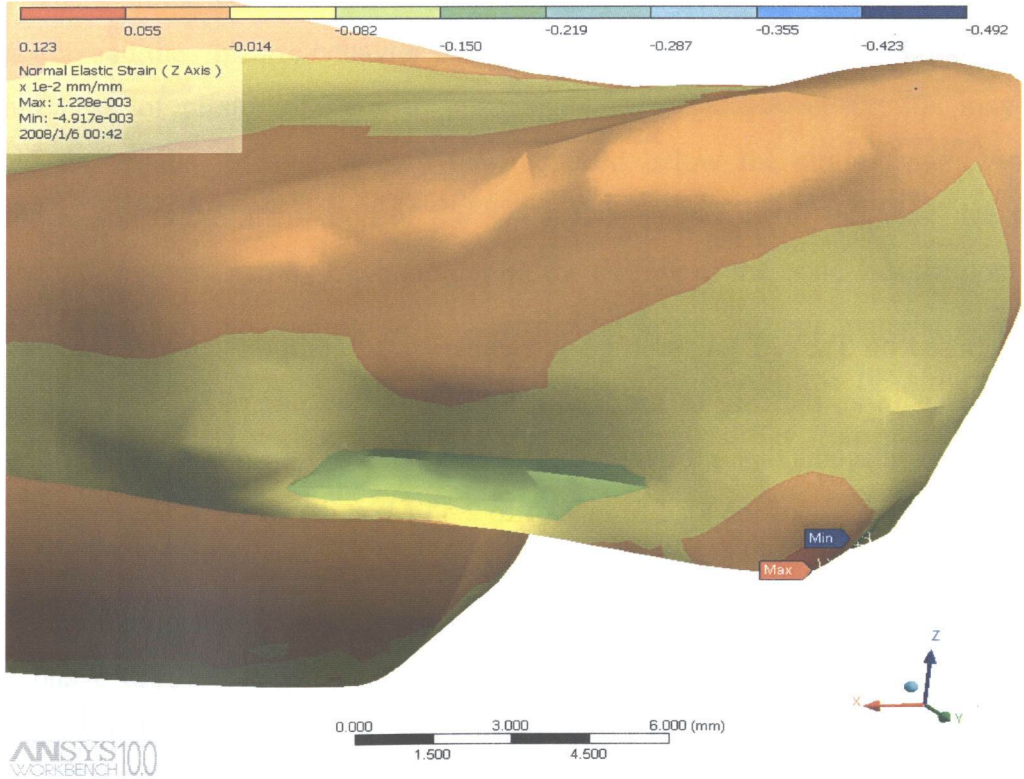

Figure 5.51 Strain distribution z-axis with applied load 1.6 MPa

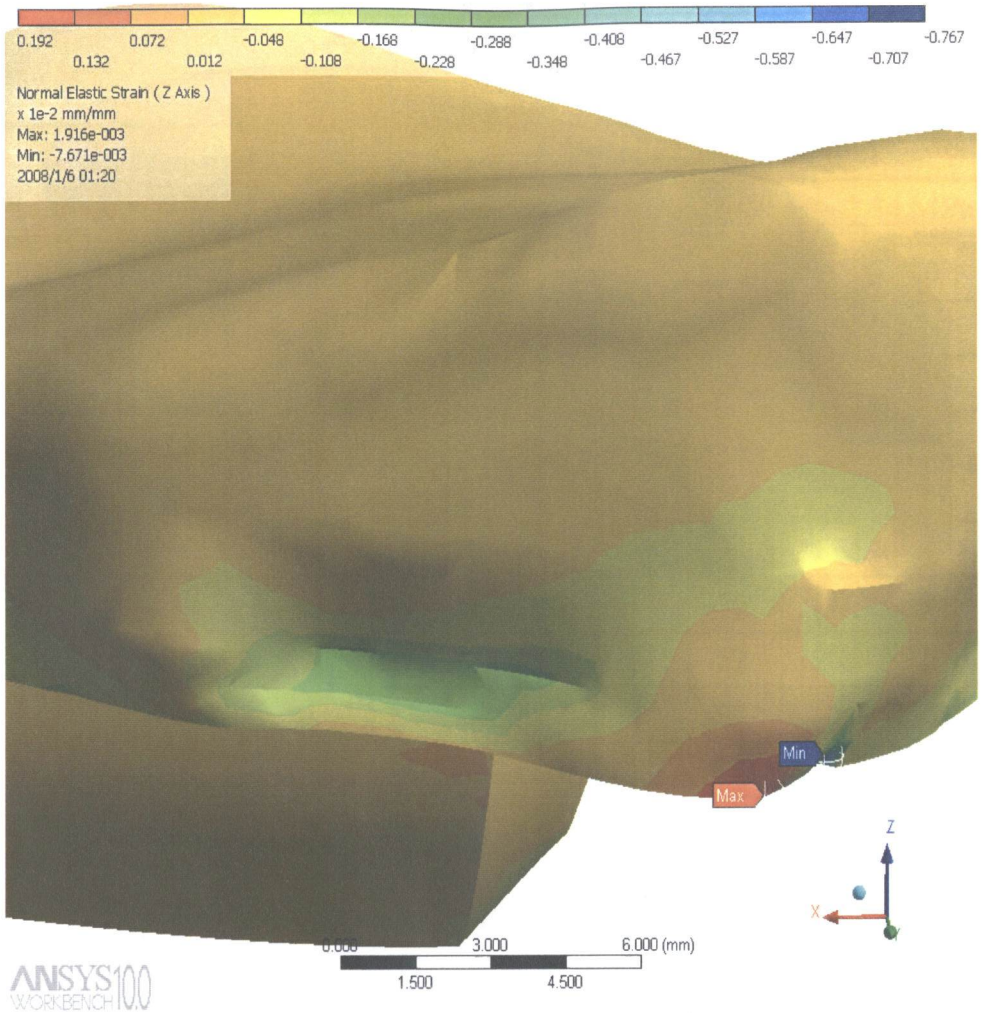

Figure 5.52 Normal strain distribution z-axis with applied load 2.54 MPa

Based on Table 5.4.1, both gauges experienced compression at the locations of the probes with an increase of the load generally, all but one of the probe, follow the same pattern. It seems that a different pattern was observed for probe 3 at probe group 2 where for an increase of the load from 1.61 to 2.54 MPa, the strain is decreased by 30 %. For probe group 1, all probes experience the same increase in strain (56 %) which is the same as the load increase. The same assertion can be made for all the probes of the probe group 2, with the exception of two highlighted probes, namely probes 3 and 4. The increase of the load from 1.6 MPa to 2.54 MPa (59 %) the probe number 3 experience and increase of 300 % in strain while probe number 4 experience a drop of 30 %.

5.4.6 Comparison of Experimental and FE results.

Experimental strain results show that for a load of 650 N, gauge 2 became saturated after it experiences a shift in the nature of load it encounters. Initially the load is tensile with a decreasing trend, experiencing compression from a load of 38 N until 416 N. The positive strain increases until saturation is reached at 650 N. Gauge 1 experiences only compression with a maximum value of 340 με. FE analysis reveals that both probes experience compression with the trends that are explained in Section 5.4.5.

There is a large disagreement between these two models especially in the behavior of the gauge 2 for which the FE does not estimate a tensile type loading at the location of the probe. For gauge 1, at load values of 38 N (0.15 MPa) and 416 N (1.61 MPa) the strain readings are 11 and 139 με respectively. Using probe tool 1 (corresponding to strain gauge 1), for 38 N and 416 N applied load, probe 2 gave 24 με and 234 με compression, respectively, and probe 5 gave 33 με and 329 με respectively. The FE analysis overestimates the state of strain at this region by between 68 and 200 %.

There are several possible reasons for the poor agreement between experiment and model, and the bizarre behavior of gauge 2. There is the possibility that the use of the thin layer of plaster of Paris to prevent strain gauge glue absorption may have affected the results, because it may have cracked below the strain gauge. Another possible reason is the alternation of the mechanical properties of the bone due to the elevated temperature seen by the bone during the potting of the bone into the container. Another factor is the notoriously large experimental scatter in bone material properties, depending on its age, quality, specimen sex, etc. Also, during the FE simulations, a fixation force of 75 N was applied, which in reality may differ from the actual force exerted by the surgeon during the implant insertion.

Another factor of great importance is the type of contact between the bone and CPP implant implemented in the FE model. To the author's knowledge, there is no information related to the friction coefficient of CPP with cortical and cancellous bone, so that the no-separation type contact was applied in the model. Furthermore, the contact areas between cortical and cancellous bone were visually estimated due to the misfit of the bone with the implant, and therefore the exact contact areas and their ratio between the assembly elements are not known. And lastly, a major factor affecting especially the

behavior of gauge 2 was the geometrical mismatches between bone and implant which were not considered during the FE analysis due to time limitations. As shown highlighted in blue in Figure 5.53 there was a gap between the cortical bone and the horizontal surface of the CPP, which was not implemented in the analysis and most likely greatly affected the results. Bone to implant mismatch is a major problem which the research team will have to address in the future, perhaps by custom making implants for a particular patient.

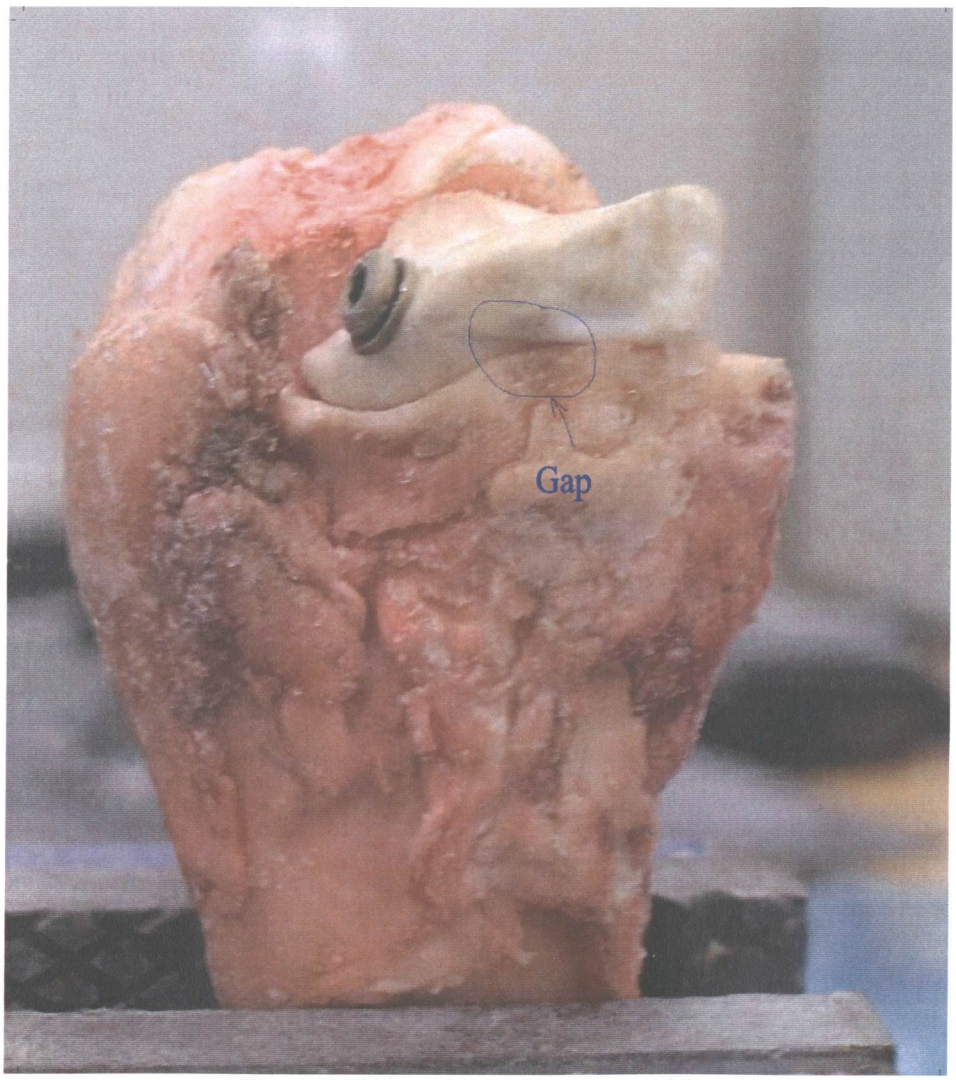

Figure 5.53 Experimental bone assembly.
Highlighted gap at the CPP implant cortical bone contact interface

CHAPTER 6

Finite Element Modeling of Articular Cartilage

FE methods have been widely used in the modeling of the cartilage layer, and this process has evolved from the single phase linear modeling to a biphasic analytical model. Modeling of the cartilage as a single linearly elastic material is valid only at the equilibrium when all the fluid flow ceases and in the situations where at the instant the load application the fluid has not yet start flowing. At every other instance under load, the cartilage exhibits high viscous effects.

Nowadays there are many prevailing theories which describe the behavior of the articular cartilage. They are divided into a number of groups, the first of which includes Biphasic and Poroviscoelastic theories. Despite the fact that both of these theories started from different roots, they reach the same conclusion. Both the theories can be used to describe not linear and nonlinear behavior of the cartilage.

The other group is comprised of viscoelasticity and hyperviscoelasticity. In this project, the modeling of the cartilage layer was based in the second group.

6.1 Articular Cartilage Modeling:

According to quasi-linear viscoelasticity theory (Fung theory) the stress relaxation function can be separated into two parts: time dependent and elastic portion which gives [48]:

$$K(\lambda,t) = W(t)T^{e}(\lambda) \tag{6.1}$$

where the total stress relaxation function K depends on both time and the stretch ratio λ, given by elastic response T^e and the reduced relaxation function W. The time dependent strain energy function of the cartilage can be expressed by the two term Prony series in the relaxation form as:

$$W(t) = W_0\left[1 - \sum_{1}^{2} A_i(1 - e^{(t/\tau_i)}\right] \tag{6.2}$$

In formula (6.2), W_0 represents the instantaneous strain energy function prior for the incompressible materials, τ_1 and τ_2 are the short and long term relaxation time constants and A_1 and A_2 are the relaxation magnitudes for short and long term.

The instantaneous strain energy function can be modeled by a three parameter hyperelastic Mooney-Rivlin material model as follows:

$$W_0 = C_{10}(I_1 - 3) + C_{01}(I_2 - 3) + C_{11}(I_1 - 3)(I_2 - 3) \tag{6.3}$$

where the C_{10}, C_{01}, and C_{11} are the coefficients that need to be determined experimentally, and coefficients I_1 and I_2 are the first and second invariants of the right Cauchy deformation tensor. In the case of a creep test, the creep compliance $J(t)$ is given by:

$$\varepsilon(t) = J(t) \cdot \sigma_0 \tag{6.4}$$

Creep compliance function can be expressed in the form Prony series:

$$J(t) = D_0\left(1 - \sum_{i=1}^{n} p1 \cdot (1 - e^{-t/\tau_i})\right) \tag{6.5}$$

In this project the determination of the Prony terms were acquired using a standard nonlinear regression method (the Marquardt-Levenberg method). For a given set of experimental data x_i and y_i, the nonlinear regression method approximates an error function (Θ^2) with respect to some unknown constants which are defined as:

$$\Theta^2(a) = \sum_{i=1}^{N}\left[\frac{y_i - y(x_i, a)}{\sigma_i}\right]^2 \tag{6.6}$$

where σ_i is the standard deviation of the measurement error of i-th data point. A set of unknowns constants a will be determined that minimize the error function given by eq.(6.6), which can be approximated by its Taylor series of the quadratic form:

$$\Theta^2(a) = c - d \cdot a + \frac{1}{2} a \cdot D \cdot a \tag{6.7}$$

Where 'd' is the gradient of the error function with respect to 'a' which will be minimized. Elements of the matrix D are the second order partial derivative of the error function with respect to parameters 'a'. Final values of parameters 'a' are obtain by inserting into the nonlinear regression algorithm initial values which will be ultimately improved.

For linear viscoelastic material, a superposition of hereditary integrals describes the time dependent response. For a load applied at time t=0 with, the variation of strain at time t+Δt is given by:

$$\varepsilon(t) = \sigma_0 \cdot J(t) + \int_0^t J(t-\xi) \frac{d\sigma(\xi)}{d\xi} d\xi \tag{6.8}$$

Loading of the creep experiment can be divided into two time segments which are given by the following discretized stress function:

$$\sigma(t) := \begin{cases} \left[\left[\sigma 1 \cdot \dfrac{t}{(t1 - t0)} \right]\right] & \text{if } 0 < t \le t1 \\ ((\sigma 1)) & \text{if } t1 < t \le t2 \\ 0 & \text{otherwise} \end{cases} \tag{6.9}$$

The hereditary integrals with Prony series kernels given by eq. (6.8) can be applied to model a loading process of the creep experiment in the following way. By assuming that strain at t=0 is $\varepsilon_0 = \varepsilon(0) = 0$ and by assuming that the load requires a certain time t_1 to reach the constant applied load, equation (6.8) takes the form:

$$\varepsilon(t) = \varepsilon_0 \cdot J(t) + \int_0^{t_1^-} J(t-\xi)\frac{d\sigma(\xi)}{d\xi}d\xi + \int_{t_1^+}^{t} J(t-\xi)\frac{d\sigma(\xi)}{d\xi}d\xi \tag{6.10}$$

$$= 0 + \frac{D_0 \cdot \varepsilon_1}{t_1}\left[\xi - \sum p_i\xi + \sum p_i \cdot \tau_i \cdot e^{-(t-\xi_i)/\tau_i}\right]_0^{t_1} + 0 \tag{6.11}$$

$$= \frac{D_0 \cdot \varepsilon_1}{t_1}\left[t_1 - \sum p_i t_1 + \sum p_i \cdot \tau_i \cdot e^{-(t-t_{1i})/\tau_i} - \sum p_i \tau_i e^{-t/\tau_{io}}\right] \tag{6.12}$$

This equation is valid only for the time interval $t_1 - t_2$. In the same way as the equation (6.8) is transformed to equation (6.12). The same integration scheme can be implemented for the interval t_0-t_1 resulting in :

$$\varepsilon_0 = \frac{D_0 \cdot \varepsilon_1}{t_1}\left[t - \sum p_i t + \sum p_i \cdot \tau_i \cdot e^{-(t-t_{1i})/\tau_i} - \sum p_i \tau_i e^{-t/\tau_{io}}\right] \tag{6.13}$$

Because the number of equations is 2 the number of the variables in the nonlinear regression algorithm is 2n+1, therefore several constraint conditions must be implemented.

$$P_i \geq 0 \quad \tau_i \geq 0 \quad D_i > 0 \tag{6.14}$$

The nonlinear regression method was implemented in MathCAD software (Mathsoft Inc., Cambridge, Ma) where the procedure is provided in the Appendices. Because only the creep data were known (no relaxation) this algorithm was used in determining the 1 term Prony series. (P_i and τ_i). These parameters were then used to obtain the relaxation form of the Prony series as described by [49], and implemented in the simplified FE model of the cartilage layer. The hyperelastic, three parameter Mooney-Rivlin material was utilized to represent the solid fibers of the cartilage layer [49]. The data of the 1 term Prony series and the data obtained from [49] for the hyperelastic model are listed in Table 6.1.

Table 6.1 Evaluated Prony Terms

Prony Constants	P_1 (No units)	τ_1 (Seconds)
Creep	0.365	2.4

Table6.2 Hyperelastic material constants [49]

C_{10} (MPa)	C_{01}(MPa)	C_{11}(MPa)
0.1	0.45	0.6

6.2 Finite Element Modeling of Cartilage

Finite element analysis of the bone assembly with cartilage layers included was not completed. Instead the analysis was accomplished on a very simplified assembly including cortical bone and the cartilage layer.

There were several reasons that the analysis was not completed with the real model. The main reason was the limited number of elements, causing the presence of elements with poor shape in the cartilage layers volumes, which when combined with the very complicated geometrical shape, required a large number of elements to be modeled. This fact left no possibility of improving the poorly shaped elements. The other possibility to overcome this limitation was the use of superelements which, however,was restricted because of the fact that in the creation of the Matrix 50 element, all the elements need to be defined and all volumes need to be meshed. Nevertheless, several attempts at generation of the superelement failed due to the restricted number of degrees of freedom allowed by the Ansys license. Due to the nonlinear characteristics of the analysis at hand, 6 DOF are required ,leaving little possibility for success. In Figure 6.1 is

shown the bone assembly in Ansys. Every element was imported individually with facet option on, ensuring prior to the import in IGS format that all elements had the same defined coordinate system. Cortical, cancellous, fixation screw and CPP implant were modeled with element type SOLID 92 while meshing of cartilage layers was accomplished with element type SOLID 187.

Problematic features that the cartilage layer exhibits are related to the its geometrical shape having an height of 0.4 mm and covering the entire surface of the tibia resulting in 87 element with poor geometrical shape.

Figure 6.1 Complete bone assembly in Ansys

Therefore, the analysis was shifted to a cylindrical shaped of height of 0.6 mm solid for the cartilage layer and a cylindrical shaped of a bigger radius for the cortical bone, as shown in figure 6.2

Meshing of the simplified model was done with SOLID 92 for the cortical bone and meshing for the cartilage was done with SOLID 187. A static analysis was implemented for cartilage layer: linear viscoelasticity (small strain viscoelasticity) and hyper-viscoelastic. This was accomplished by the model combination available in Ansys. For both types of simulations the Kevin-Voigt model was adopted. The contact between cartilage layer and cortical bone was treated as 'bonded always' type, not allowing any type of relative movement

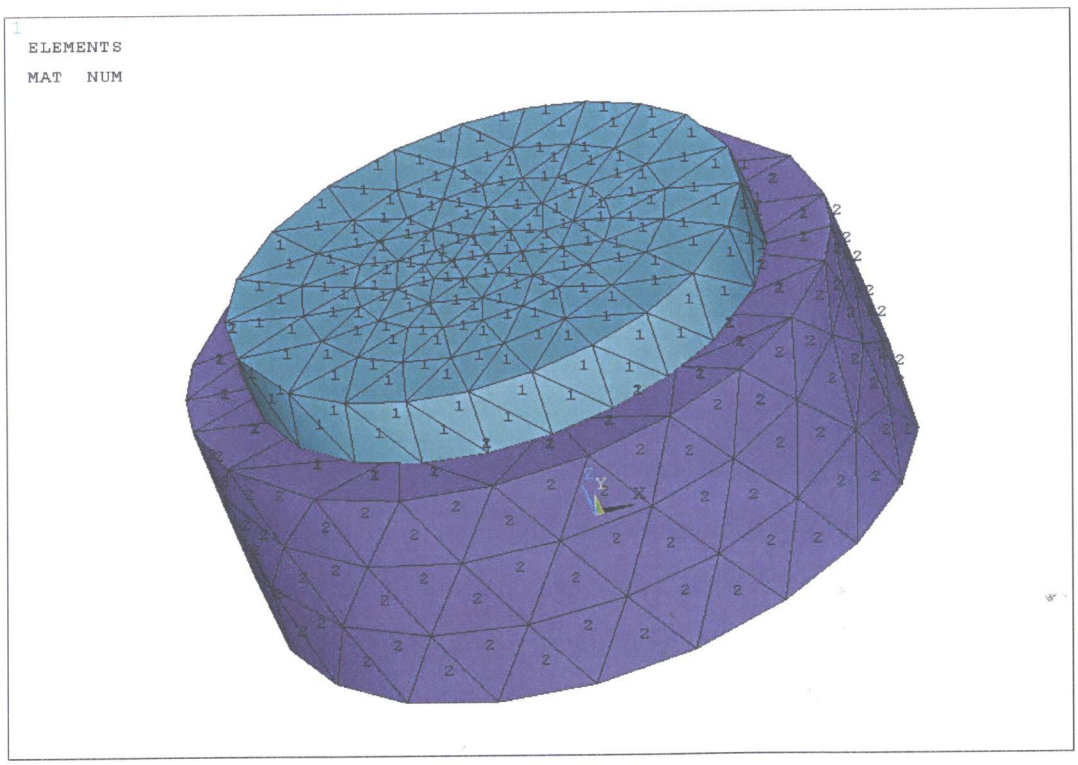

Figure 6.2 Simplified assembly. Cartilage layer and cortical bone

CHAPTER 7

Concluding Remarks and Future Work

7.1 Conclusions

A 3-dimensional solid model of the sheep's tibia bone was constructed based on the provided CT scans. This model was used to generate the solid model of a biodegradable CPP implant of the medial side of the tibial plateau, which is used as an anchorage structure in the restoration of damaged cartilage layer in synovial joints.

The purpose of this investigation was the determination of the optimal structural shape which would address the two main requirements that a structure of this nature needed to satisfy: sufficient bulk strength of the implant and only a limited amount of allowed micromotion.

The overall stability and strength of the implant structure depended on many factors which were considered: keel orientation cross-sectional geometry and dimensions, fixation screw length, screw angle insertion, fixation screw force, and overall implant height.

Implant height was maintained constant throughout project, due to assumptions related to the area of the cartilage layer being repaired covering the entire medial tibial plateau. Keel orientation, the angle that the keel axis creates with the ventral-dorsal direction, was found to be a very important parameter in implant design. However, there was not an apparent clear pattern that related the implant performance to the orientation. For each individual keel angle, the failure modes were unique to that orientation, with locations of destructive tensile and compressive stresses characteristic only for that specific angle.

Keel dimensions, and more specifically keel cross-sectional dimensions, had a great effect in the overall stability of the implant structure. Two cross-sectional shapes were investigated: trapezoidal and semicircular. For both shapes, as the cross-sectional area of the keel was increased, the stresses and bone/implant relative sliding distances decreased, indicating a stronger and more stable implant. The shape of the final design was based not only on the performance in terms of strength and stability, but also on the easy of implantation.

The screw angle of insertion did not greatly affect the stress distribution on the implant structure. For the angles investigated, the variation of stresses was very small, never leaving to implant failure based upon this parameter alone; however screw angle

insertion was strongly associated with the keel length due to the requirement of where the screw exiting had to exit.

Keel length played a very important role in the performance of the implant. The final design was based on the longest possible keel, however an increase in keel length did not necessarily imply improvement of the performance, as the analysis for three different keel length showed.

Another factor that was analyzed was the screw insertion force. The implant performance was not affected by this force until it reached a value of 160 N. A further increase beyond this value causes the appearance of high and possibly destructive stresses.

The analysis of the FE results for assessing the possibility of implementing a totally biodegradable implant (use of biodegradable screw) showed that it is not feasible.

Finally, the experimental verification showed that the implant displayed as a very robust behavior, experiencing no fracture even though applied load was several times higher than that to which it would naturally be exposed. The experimental results did not match those predicted by the FE mainly because of mismatch between the tested bone, and that for which the implant was originally designed, which was much smaller than that used in the test,

7.2 Future work

The work involved in this project has also lead to specific recommendations for improvement in future work related to the design of models of biodegradable structures. Such recommendations include:

1) The accuracy of the measured distributed load applied over the tibia plateau needs to be improved. Because of the lower threshold with pressure sensitive files, it is not possible to measure load lower than 2 MPa, resulting in a significant uncertainty in applied load.
2) The performance of the implant is strongly related to the type of contact conditions implemented. The accurate assessment of the bone ingrowth rate would lead to a better specification of these contact conditions as a function of time.
3) During the experimental set up the cut on the bone was based only on the visual comparison between the solid model and the sheep's tibia. Further more the cut was accomplished by an electrical jigsaw. Application of sophisticated cutting tools such as laser operating cutters, would significantly improve the quality. The cut on the host bone which directly not only affect the initial performance of the implant by providing a better fit with the implant but as well prevent the bone to grow over the cartilage compromising the very purpose this procedure is being implemented. Another effect of this kind of improvement is that it would easy the surgical procedure that the surgeon has to perform. The implementation of this type of procedure in vivo is accomplished in very tight places where the room to maneuver is very small and
4) Another way that would improve the success rate of the procedure is the possibility of the application of *in vivo* sizing of the hosting bone. This would lead to the perfect fit between the hosting bones, placing the implant in perfect support conditions (contact with the cortical bone).
5) The design of the implant in this project was based only on the CT scans of only one sheep tibial bone. Size averaging of a large population of

sheep's, would decrease the size difference between the implant and host bone, consequently increasing the chance for success of the biodegradable implants.

APPENDIXES

data :=

	0	1
0	0	0
1	1	0.6352
2	2	0.6555
3	3	0.663
4	4	0.6705
5	5	0.6855
6	6	0.6951
7	7	0.7047
8	8	0.7154
9	9	0.7272
10	10	0.7368
11	11	0.7475
12	12	0.7571
13	13	0.7689
14	14	0.7764

t2 = 3200

$\varepsilon := data^{\langle 1 \rangle}$

t1 = 1

σ1 := 129190

$$\sigma(t) := \begin{cases} \left[\left[\sigma 1 \cdot \frac{t}{(t1 - t0)} \right]\right] & \text{if } 0 < t \le t1 \\ \left(\left(\sigma 1\right)\right) & \text{if } t1 < t \le t2 \\ 0 & \text{otherwise} \end{cases}$$

$t := data^{\langle 0 \rangle}$

guess values:

a1 := 0.12

τ1 := 5

D := 0.0

Given

$a1 \ge 0$ $\tau 1 \ge 0$ $D > 0$

$$\varepsilon 1(t) := D \cdot \frac{\sigma 1}{t1} \cdot \left(t - P1 \cdot t + P1 \cdot \tau 1 - P1 \cdot \tau 1 \cdot \exp\left(\frac{-t}{\tau 1} \right) \right)$$

$$\varepsilon 2(t) := D \cdot \frac{\sigma 1}{t1} \cdot \left[t1 - P1 \cdot t1 + P1 \cdot \tau 1 \cdot \exp\left[\frac{-(t - t1)}{\tau 1} \right] - P1 \cdot \tau 1 \cdot \exp\left(\frac{-t}{\tau 1} \right) \right]$$

$$\begin{pmatrix} D \\ a1 \\ \tau 1 \end{pmatrix} := \text{Find}(D, a1, \tau 1)$$

REFERENCES

[1] Korkala O, Kuokkanen H. " Autogenous osteoperiosteal grafts in the reconstruction of full-thichness joint surface defects" Int Orthop 1991; 15: 233-7

[2] Bonucci E, " Mechanical Testing of Bone and the Bone-Implant Interface". Chapter 1: Basic Composition and Structure of Bone. Edited by Y.H. An and R.A. Draughn. CRC Press LLC, 1995; 3-17

[3] Linde F, " Elastic and Viscoelastic Properties of Trebecular Bone by a compression testing approach". Danich Medical Bulletin; Vol 41, No 2, 1999; 119-138

[4] Knott L, Bailey AJ. " Callogen Cross-Links in mineralizing Tissues: A review of their Chemistry, Function and Clinical Relevance" Bone ; Vol 22, No. 3, 2003; 181-187

[5] Oxlund H, Mosekilde L, Ortoft G, " Reduced concentration of Collagen reducible cross links in Human Trebecular Bone with respect to age and Osteoporosis." Bone; Vol. 19, No. 5, 2002; 479-484.

[6] Homminga GN, Bulstra SK, Bouwmeester PS, Van Der Linden AJ, "Perichondral grafting for cartilage lesions of the knee". J Bone Joing Surg. 1990: 72B, 1003-7

[7] Amger, amm P, RiegelsNielsen P, Pedersen H. " Osteochondrities dissecans of the femoral condyle treated with periosteal transplantation – poor outcome in 14 patiens followed for 6-9 years. Acta Orhop Scand 1998: 69:595-7

[8] Bousmeester S, Beckers J, Kuijer R, van Dla, Bulstra S. " Long-term results of rib

periochondrial grafts for repair of cartilage defects in the human knee." Int Orthop 1997; 21:313-17

[9] Korkala O, Kuokkanen H. " Autogenous osteoperiosteal grafts in the reconstruction of full-thichness joint surface defects" Int Orthop 1991; 15: 233-7

[10] Hoikka VE, Jaroma HJ, Ritsila VA. " Reconstruction of the patellar articulation with periosteal grafts.4-year follow-up of 13 cases" Acta Orthop Scand 1990; 61:36-9

[11] Waldman SD, Spiteri CG, Grynpas MD, Pilliar RM, Kandel RA. " Long-Term Intermittent compressive stimulation Improves the composition and mechanical properties of Tissue-Engineered Cartilage" Tissue Eng Vol. 10, 2004, 1323-1329

[12] Knecht S, Vanwanseele B, Stussi E. "A review of the mechanical quality of articular cartilage-Implications for the diagnosis of osteoarthritis" Clinical Biomechanics 21 (2006) 999-1012

[13] Bobic V. " Arthroscopic osteochondral autograft transplantation in anterior Cruciate ligament reconstruction: a preliminary clinical study". Knee Surg Sports Traumatol Arthrose 1996; 3:262-4

[14] Matsusue Y, Vamamuro T, Hama H. " Arthroscopic multiple osteaochondral transplantation to the Chondral defect in the knee associated with anterior Cruciate ligament disruption" Arthmscopy 1993;9:318-21

[15] Morelli M, Nagamori J, Miniaci A. " Management of Chondral injuries of the knee by osteochondral autogenours transfer (mosaicplasty)" J Knee Surg 2002; 15:185-90

[16] Hangody L, Fuies P. " Autologous osteochondral mosaicplasty for the treatment of full-thickness defects of weight-bearing joints: ten years of experimental and and clinical experience". J Bone Joint Surg [Am] 2003;85-A (Suppl 2):25-32

[17] Meyers M, Jones R, Bucholz R, Wenger D. " Fresh autogenous grafts and osteochondral allografts for the treatment of segmental collapse in osteonecrosis on the hip". Clin Orthop 1983; 174:107-12.

[18] McDermott A, Langer F, Pritzker K, Gross A. " Fresh small-fragment osteochondral allografts. Long-term follow up study on first 100 cases". Clin Orthop 1985; 197:96-102.

[19] Mahomed M, Beaver R, Gross A. "The long-term success of fresh , small fragment osteochondral allografts used for intraarticular post-traumatic defects in the knee joint". Orthopedics 1992; 15:1191-9.

[20] Hunziker EB. " Articular cartilage repair: basic science and clinical progress: a review of the current status and prospects". Osteoarthritis Cartilage 2002; 10:432-63

[21] Soderman P, Malchau H, Herberts P, Zugner R, Regner H, Garellick G. "Outcome after total hip Arthroplasty: part II. Disease-specific follow-up and the Swedish National Total Hip Arthroplasty Register".Acta Orthop Scand 2001;72(2):113-9

[22] Berry DJ, Harmsen WS, Ilstrup D, Lewallen DG, Cabanela ME. " Survivorship of uncemented proximally porous-coated femoral components". Clin Orthop Relat Res 1995; October (319): 167-77

[23] Waldman SD, Grynpas MD, Pilliar RM, Knadel RA. " Characterization of cartilaginous tissue formed on calcium polyphosphate substrates in vitro". J Biomed Mater Res 2002;62(3):323-30

[24] Pilliar Rm. "Porous-surfaced metallic implants for orthopedic applications". J Biomed Mater Res 1987; 21(A1):1-33

[25] Tencer AF, Johnson KD, " Biomechanics in orthopaedic trauma :bone fracture and fixation" Lond: Martin Dunitz, 1994, 31.

[26] Pilliar, R.M., Fillagi M, Wells,J.D., Grynpas, M.D., Kandel,R.A. "Porous calcium polyphosphate scaffolds for bone substitute applications-In vitro studies". Biomaterials. 2001 (22). 963-972

[27] Grynpas, M.D., Pilliar, R.M., Kandel,R.A, Renlund, R., Fillagi M, Dimitriu, M., "Porous calcium polyphosphate scaffolds for bond substitute applications in vivo studies". Biomaterials. 2001 (23) 2063-1070.

[28] Li B, Aspden RM, " Material Properties of Bone from the femoral neck and calcar Femorale of patients with osteoporosis and osteoarthritis" Osteoporosis International; Vol 7, 1992; 450-456.

[29] Rho,J.Y. "Microstructural elasticity and regional heterogeneity in human femoral bone of various ages examined by nanoindentation." Journal of Biomechanics; Vol.35, 2003; p.189-198

[30] BME/ME 456 Biomechanics website. http://www.engin.umich.edu/class/bme456/cartilage/cart.htm

[31] Nieminen Heikki. " Acoustic Properties of Articular Cartilage- Effect of Composition , Structure and Mechanical Loading" Doctoral Dissertation,

[32] Porter, N.L., Pilliar,R.M., Grynpas,M.D., "Fabrication of porous calcium polyphosphate implants by solid freeform fabrication: A study of processing parameters and in vitro degradation characteristics" Biomaterials. 2001 (24) 1898- 1996

[33] Ropp, R.C., Inorganic polymeric glasses. Amsterdam: Elsevier Science Publishers; 1992. 91-161.

[34] S.G.Lekhntskii, 'Theory of Elasticity of an Anisotropic Elastic Body'. , 1968

[35] K.J.Bathe, 'Finite Element Procedures", Prentice-Hall of India., New Dehli, India 2005.

[36] Wriggers P., "Computational Contact Mechanics". John Wiley & Sons, INC., 2002

[37] Pietrzak G., Curnier A., "Continuum mechanics modeling and augmented Lagrange formulation of multibody, large deformation frictional contact problems". Proceedings of COMPLS 5, 1997, 878-883.

[38] Papini M, Zalzal P. thirdgen.zip, from the International Society of Biomechanics (ISB) Finite Element Mesh Repository, Istituti Ortopedici Rizzoli" Available from: http://www.cineca.it/hosted/ LTM- IOR/back2net/ISB_mesh /isb_mesh.html.

[39] Katz,J.L., Meunier,A., "The elastic anisotropy of bone". Journal of Biomechanics 20, 1987;1063-1070.

[40] Reilly, D.T., Burstein,A.H.,. "The elastic and ultimate properties of compact

bone tissue". Journal of Biomechanics 8, 1975; 393-405

[41] Protopappas, V.C., Kourtis, I.C., Kourtis, L.C., Malizos, K.N., Massalas,X.V., Fotiadis,D.I., "Three-dimensional finite element modeling of guided ultrasound wave propagation in intact and healing long bones". Journal of Acoustical Society of America 121 (6), June 2007, ; 3907-3921

[42] Simon, U., Augat, P., Ignatius, A., Glaes, L., "Influence of the stiffness of bone defect implants on the mechanical conditions at the interface – a finite element analysis with contact". Journal of Bioemechanics 36 2003; 1079- 1086

[43] Rehman, I., Smith R, Hench, L.L., Bonfield,W., "Structural evaluation of human and sheep bone and comparison with synthetic hydroxyapatite by FT-Raman spectroscopy". 1995. Journal of Biomedical Material Research. 29 (1995) 1287-94.

[44] ANSYS, version 10.0, (2005). ANSYS Analysis User's Manual and ANSYS Theory Manual.

[45] Boresi, A.P., Schmidt, R.J., "Advanced Mechanics of Materials". John Wiley & Sons, INC. Sixth Edition, 2002

[46] Duda,G,N., Ecker-Hubner,K., Kreutner,A., Miller,R., Claes,L., "Analysis of inter-Fragmentary movement as a function of musculo-Skeletal loading conditions in sheep". Journal of Biomechanics 31, 1998;201-210

[47] Callister,D.W., "Materials Science and Engineering, an Introduction". John Wiley & Sons, INC. Sixth Edition, 2003.

[48] Fung, Y.C. "Bio-viscoelastic solids." In: Biomechanics: Mechanical Properties of Soft Tissues. New York :Springer-Verlag, 1993, pp 242-320.

[49] Z. Li, J.E. Alonso, J. E. Kim, J. S. Davidson, B. S. Etheridge, and A.W. Eberharddt. " Three- Dimensional Finite Element Models of the Human Pubic Symphysis with Viscohyperelastic Soft Tissues", 2006, Annals of Biomedical Engineering., Vol. 34, pp 1452-1462.